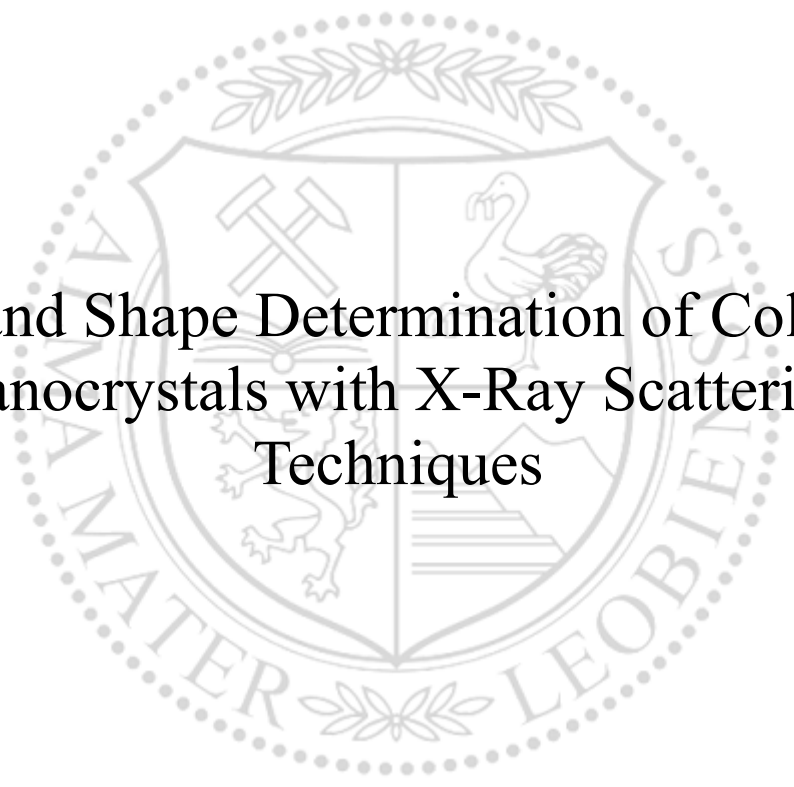




Chair of Physics

Master's Thesis



Size and Shape Determination of Colloidal
Nanocrystals with X-Ray Scattering
Techniques

Maximilian Ritter, BSc

June 2020

Acknowledgement

I would like to start by thanking my family and girlfriend for the unending support during my entire duration of study here at Montanuniversität Leoben. They always had a friendly ear for me and my concerns, however ridiculous these might have been at times. Without their support, I probably would not be where I am right now, and this work would never have been written in the first place.

My deepest gratitude goes out to my advisor and mentor Dr. Rainer Lechner for introducing me to the highly complex, but also incredibly interesting topic of Small Angle X-ray Scattering, but also for his incredibly valuable scientific inputs. I want him to know that the time he devoted to guiding me through this work, especially in the aggravated times during the Covid-19 pandemic lockdown, is highly appreciated. As are all the life lessons I could learn from him.

I would also like to thank Prof. Oskar Paris for his extremely helpful scientific advice regarding my work, but also for the hospitality I was greeted with from my first day onwards.

Additionally, I would like to thank all colleagues and friends at the Institute of Physics for their advice regarding both scientific, but also personal things. I would especially like to thank Dr. Gerhard Popovski for his help regarding highly specific SAXS questions and the fact that he always had an answer and Dr. Markus Kratzer for all the fun conversations we had about science and Sci-Fi.

Finally, I would like to thank all my friends, both here at the Montanuniversität and back in Vienna for constantly reminding and showing me that there is more to life than just university and science. That being said, I would also like to thank them for the great learning community that we have been right from the first day onwards.

Eidesstattliche Erklärung

Ich erkläre an Eides statt, dass ich diese Arbeit selbständig verfasst, andere als die angegebenen Quellen und Hilfsmittel nicht benutzt, und mich auch sonst keiner unerlaubten Hilfsmittel bedient habe.

Ich erkläre, dass ich die Richtlinien des Senats der Montanuniversität Leoben zu "Gute wissenschaftliche Praxis" gelesen, verstanden und befolgt habe.

Weiters erkläre ich, dass die elektronische und gedruckte Version der eingereichten wissenschaftlichen Abschlussarbeit formal und inhaltlich identisch sind.

Affidavit

I declare in lieu of oath, that I wrote this thesis and performed the associated research myself, using literature cited in this volume.

Maximilian Ritter

Leoben, June 2020

Abstract

The morphology of nanocrystals has a substantial influence on their highly diverse physical properties ranging from luminescence to biocompatibility. One key to success for the various applications and research areas is understanding the effect the morphology has on these properties and controlling the morphology during synthesis. Transmission electron microscopy has been the leading tool for analysing the morphology for the last decades. As modern-day nanocrystals are no longer used for purely fundamental research, the fact that it is extremely time consuming to analyse a substantial number of nanocrystals using transmission electron microscopy, has led to the developed of different methods. The properties of real-life nanocrystal applications do not depend on the morphology of a few selected ones analysed with transmission electron microscopy, but rather on the overall morphology of all nanocrystals in the application.

Small angle X-ray scattering is a leading technique to analyse the morphology of colloidal nanocrystals with a sub-nanometre resolution. Using modern *ab initio* bead modelling the size, but more importantly also the 3D mean shape of at least 10^6 nanocrystals, seen in all directions, can be retrieved from the scattering data.

To study the capability of shape retrieval from small angle X-ray scattering data, four superparamagnetic iron oxide nanocrystals with different shapes, ranging from a simple cube-like shape to a highly complex star-like shape are analysed. The results are then compared to transmission electron microscopy images to evaluate the success of the shape retrieval. X-ray diffraction is performed to complement and support the results.

It is shown that without any *a priori* information about the shape, it is possible to extract the exact shape for simple structures and for complex structures the characteristic features are reproduced. Using either *a priori* information from e.g. transmission electron microscopy or the outcome of the first shape retrieval process, the results can be greatly enhanced by predefining the symmetry of the system, when applied with extreme caution. Then even the complex star-like shape can be retrieved, demonstrating that shape retrieval from small angle X-ray scattering data is a fiercely powerful tool and a definite alternative to transmission electron microscopy.

Kurzfassung

Die Morphologie von Nanokristallen hat einen substantiellen Einfluss auf die diversen Eigenschaften der Nanokristalle und beeinflusst Eigenschaften von Magnetismus bis hin zu Biokompatibilität. Ein Schlüsselfaktor für den Erfolg der zahllosen Anwendungen und Forschungsprojekte ist es den Zusammenhang zwischen Morphologie und Eigenschaften zu verstehen und die Morphologie während der Synthese zu kontrollieren. Transmission Elektronen Mikroskopie war lange Zeit das vorherrschende Mittel zur Untersuchung der Morphologie von Nanokristallen. Doch da moderne Nanokristalle nicht mehr nur Teil der Grundlagenforschung sind und es extrem zeitaufwändig ist mit Transmission Elektronen Mikroskopie große Mengen von Nanokristallen zu untersuchen, wurden neue Methoden entwickelt. Die Eigenschaften von realen Anwendungen der Nanokristalle hängen nämlich nicht von der Morphologie einiger weniger ausgewählter, mit Transmission Elektronen Mikroskopie analysierter Nanokristalle ab, sondern von der Morphologie des Ensembles.

Röntgen-Kleinwinkelstreuung ist eine der führenden Methoden zur Analyse der Morphologie von kolloidalen Nanokristallen mit Sub-Nanometer Auflösung. Durch *ab initio* Modelle kann sowohl die Größe als auch die gemittelte Gestalt von bis zu 10^{11} Nanokristallen aus den Daten der Röntgen-Kleinwinkelstreuung rekonstruiert werden.

Um die Leistungsfähigkeit der Gestaltrekonstruktion aus Röntgen-Kleinwinkelstreuung Daten zu analysieren, werden vier superparamagnetische Eisenoxid Nanokristalle mit unterschiedlicher Gestalt untersucht. Die Gestalt dieser Nanokristalle geht von einer einfachen würfelförmigen bis hin zu einer äußerst komplexen sternförmigen Form. Die Ergebnisse werden mit Transmission Elektronen Mikroskopie Bildern verglichen, um den Erfolg der Rekonstruktion zu beurteilen. Röntgendiffraktion wird zur Ergänzung und Unterstützung der Ergebnisse durchgeführt.

Es wird gezeigt, dass ohne *a priori* Information die genaue Gestalt der einfachen Nanokristalle und die charakteristischen Merkmale der komplexen Nanokristalle rekonstruiert werden können. Nutzt man *a priori* Information aus Transmission Elektronen Mikroskopie Bildern oder aus den Modellen, welche ohne Symmetrie angefertigt wurden, können die Ergebnisse deutlich verbessert werden, indem man die Symmetrie des Systems definiert. Zwingt man dem System eine Symmetrie auf, ist es jedoch notwendig extreme Vorsicht walten zu lassen. Mit vorgegebener Symmetrie ist es sogar möglich die komplexe Gestalt der sternförmigen Nanokristalle zu rekonstruieren, was eindrucksvoll demonstriert, dass die Gestaltrekonstruktion aus Röntgen-Kleinwinkelstreuung ein mächtiges Tool ist und eine definitive Alternative zu Transmission Elektronen Mikroskopie darstellt.

Inhaltsverzeichnis

ABBREVIATIONS AND SYMBOLS	3
1. INTRODUCTION	4
2. THEORY.....	6
2.1. SCATTERING THEORY.....	6
2.2. SMALL ANGLE X-RAY SCATTERING	9
2.3. SMALL ANGLE X-RAY SCATTERING DATA ANALYSIS	11
2.3.1. GUINIER ANALYSIS.....	11
2.3.2. POROD ANALYSIS	11
2.3.3. FROM SAXS DATA TO THE SHAPE OF A PARTICLE	12
2.4. SHAPE RETRIEVAL	14
2.4.1. SIMULATED ANNEALING	14
2.4.2. THE LOSS OF INFORMATION DUE TO RANDOM ORIENTATION	15
2.4.3. RETRIEVING THE SHAPE.....	16
3. EXPERIMENTAL.....	18
3.1. SAMPLE PREPARATION	18
3.2. MEASUREMENTS.....	19
3.2.1. SMALL ANGLE X-RAY SCATTERING MEASUREMENTS	19
3.2.2. X-RAY DIFFRACTION MEASUREMENTS.....	19
4. ANALYSIS	21
4.1. DATA PROCESSING	21
4.1.1. SAXS DATA.....	21
4.1.2. XRD DATA	24
4.2. SHAPE RETRIEVAL	24
4.2.1. CREATING THE MODELS	25
4.2.2. AVERAGING THE MODELS	26
4.3. DIAMETER DISTRIBUTION	27
5. RESULTS	29
5.1. SHAPE RETRIEVAL FROM SAXS DATA.....	29
5.1.1. ATSAS MODELS WITHOUT PREDEFINED SYMMETRY	29

5.1.2.	ATSAS MODELS WITH PREDEFINED SYMMETRY	35
5.1.3.	SASHEL MODELS	38
5.2.	DIAMETER DISTRIBUTION	42
5.2.1.	DIAMETER DISTRIBUTION FOR THE MODELS WITHOUT A PREDEFINED SYMMETRY	42
5.2.2.	DIAMETER DISTRIBUTION FOR THE MODELS WITH A PREDEFINED SYMMETRY	45
5.3.	X-RAY DIFFRACTION	47
6.	DISCUSSION.....	51
6.1.	EVALUATION OF THE SAXS MODELS.....	51
6.1.1.	SAXS MODELS WITHOUT A PREDEFINED SYMMETRY	51
6.1.2.	SAXS MODELS WITH A PREDEFINED SYMMETRY	56
6.2.	INTERPRETING THE DIAMETER DISTRIBUTION	60
6.2.1.	INTERPRETING THE DIAMETER DISTRIBUTION OF THE MODELS WITHOUT A PREDEFINED SYMMETRY	60
6.2.2.	INTERPRETING THE DIAMETER DISTRIBUTION OF THE MODELS WITH A PREDEFINED SYMMETRY	62
6.3.	XRD DATA AND CRYSTAL GROWTH DURING SYNTHESIS	63
7.	CONCLUSION	65
	REFERENCES.....	68

Abbreviations and Symbols

approx.	... approximately
DA(s)	... dummy atom(s)
DNA	... deoxyribonucleic acid
e.g.	... <i>exempli gratia</i>
FCC	... face centred cubic
FWHM	... full width at half maximum
GIFT	... generalised indirect Fourier-transformation
h	... hour
HHD	... half height dimension
IFT	... indirect Fourier-transformation
NC(s)	... nanocrystal(s)
NSD	... normalised spatial discrepancy
OA	... oleic acid
PDDF	... pair distance distribution function
QD(s)	... quantum dot(s)
RT	... room temperature
SAS	... small angle scattering
SAXS	... small angle X-ray scattering
SPIONs	... super paramagnetic iron oxide nanocrystals
SDD	... sample detector-distance
TEM	... transmission electron microscopy
XRD	... X-ray diffraction

1. Introduction

Nanocrystals have been known since the 19th century, as proven by the mention of ruby coloured gold sols by Faraday in 1857 [1]. Nanoscience or Nanotechnology using colloidal nanocrystals (NCs) as known to us today, however, has only started about 40 years ago in the early 80s of the last century. In the beginning the main focus was on semiconductor NCs for use in solar energy harvesting devices. Whilst these colloidal semiconductor NCs, later renamed to quantum dots (QDs) due to the quantum size effect, have become the masterclass of modern NC science, research on colloidal NCs has lately been the focus of various scientific fields. What distinguishes NCs from other hot scientific topics, is the uttermost variation of scientific applications they acquire vogue in, such as electronics, information storage, catalysts, sensors, molecular biology and medicine. Despite different applications of the NCs, the scientific challenge is always similar, tuning the NCs' properties by controlling chemistry, size and shape to best fit the application's demands. One mannerism of NCs is that their chemical and physical properties are particularly sensitive on size and shape. At the same time, synthesising macroscopic quantities of colloidal NCs with controlled chemistry, size and shape is the main challenge for chemists working in this field. [2]–[6]

NCs are by definition smaller than 1 μm , but for practical reasons often only crystals smaller than 500 nm are considered as NCs and in applications NCs are usually even smaller than that. [7]

One type of NCs that have received a considerable amount of attention over the last couple of years, are super paramagnetic iron oxide nanocrystals (SPIONs). They exhibit exceptional magnetic properties and are considered to play a crucial role in many future key technologies. SPIONs are already used in medicine as MRI contrast agents, traces for magnetic particle imaging and only recently also in materials science for ceramic-organic nanocomposites with exceptional features. Possible future technological applications of SPIONs are targeted drug delivery, magnetic hyperthermia and biosensing. The advantages of SPIONs for these applications are numerous, for one they are inexpensive to synthesise, the precursors are readily available, they are chemically stable, environmentally safe and, the most important property for medical applications, biocompatible. The SPIONs' morphology strongly influences the magnetic properties, but also biocompatibility. Understanding how the magnetic properties and the morphology of the SPIONs correlate, will play a crucial role in the success of SPIONs in future technologies. [8] [9]

In the last decade enormous advancements have been made regarding the possibility of synthesising precedingly more and more complex shapes of NCs with incredible process control. [2] [8] [10] [11] With increasing complexity of the NCs' shape, the focus has lately been on improving existing methods and developing new ones to resolve structural differences on a nanometre scale. Transmission electron microscopy (TEM) is the most common analysis method to study the morphology of NCs, as single atom resolution is achievable. But as always,

this comes with a series of drawbacks. The main one being, that quality TEM images can only be made of a few hundred NCs at once at absolute maximum. Most NC devices contain or consist of at least 10^6 NCs, most likely many more. TEM therefore, may be the preferred tool for fundamental research, but for a more applied context, the fact that it is time consuming to analyse a great enough number of NCs limits its application area. The method of choice for analysing the morphology of an ensemble of NCs is small angle scattering (SAS), more precisely small angle X-ray scattering (SAXS). [5]

SAXS was developed in the 1930s to study metal alloys, but was quickly discovered by polymer physicists, colloidal chemists and molecular biologists, who all came to appreciate the possibility of exploring the nanostructure of a vast range of materials. The two milestones in the history of SAXS, that have led to its modern-day appreciation, were readily available access to intense synchrotron sources from the 70s onwards and advances in computational methods and the capacity of modern computers starting in the 90s. Today, SAXS is a well-established analysis technique to study the morphology (size and shape) of nanometre scaled systems in solution. SAXS' main advantage is the possibility to study up to 10^{11} particles in a single experiment, a substantially larger number than in TEM. As the NCs are randomly oriented, the orientational average over a large number of NCs is analysed, giving the information statistical validity and indicating that the retrieved shape is a 3D representation of the averaged mean NC shape. [5] [6] [12]

Ever since Watson & Crick [13] discovered the structure of the deoxyribonucleic acid (DNA) using X-Ray diffraction (XRD) in 1953, molecular biology was closely tied to structural analysis using X-rays. Therefore, structure analysis from SAXS data has long been used in biology. The advantage of studying proteins is that unlike inorganic NCs, they don't exhibit any noticeable polydispersity and are not faceted, greatly simplifying the shape retrieval process. [5] [14]

It is because of this long history, that many shape retrieval software packages are specialised on molecular biology. The most popular software ATSAS [15] was even developed by a molecular biology group, the European Molecular Biology Laboratory (EMBL) in Hamburg, Germany. Many modern tools are specifically tailored to study and retrieve shapes commonly found in molecular biology, such as helices. An example for this is the relatively new SasHel software developed by Max Burian [6].

In this work the morphology of four different SPIONs is analysed using SAXS. The shapes of the NCs all exhibit characteristic features of different complexity. Due to the strongly differing complexity of the NCs' shape, it is possible to analyse the limits of the shape retrieval process for NCs based on SAXS data. The models are created using both ATSAS and SasHel, and further analysed using Matlab and Paraview. Additionally, XRD measurements of the NCs are performed to complement the SAXS results.

2. Theory

The aim of this chapter is to provide a concise overview of small angle scattering theory and techniques, focusing mainly on SAXS, as the main focus of this work is on SAXS measurements and analysis. SAS of both X-rays and neutrons is a tool used in various fields, from condensed matter physics to molecular biology. The size and shape of NCs can be studied using a vast range of different techniques including, but not limited to, electron microscopy, neutron scattering, X-ray scattering and X-ray diffraction. The main principle of all these techniques is the interaction of an incoming particle (photon, electron or neutron) with the matter that is being analysed. **Figure 1** schematically illustrates the different types of interaction observed between X-rays and matter. Generally speaking, the interaction includes (a) reflection, (b) absorption, (c) transmission and (d) inelastic and (e) elastic scattering. This theory chapter will focus on scattering, as it is the main focus of this work. All techniques can be used to analyse materials on strongly differing scales. Using X-rays and electrons with sub nanometre wavelengths it is possible to resolve structures on an atomic level. [16] [17] [18] This chapter is partly based on the *Theory* chapter in [19].

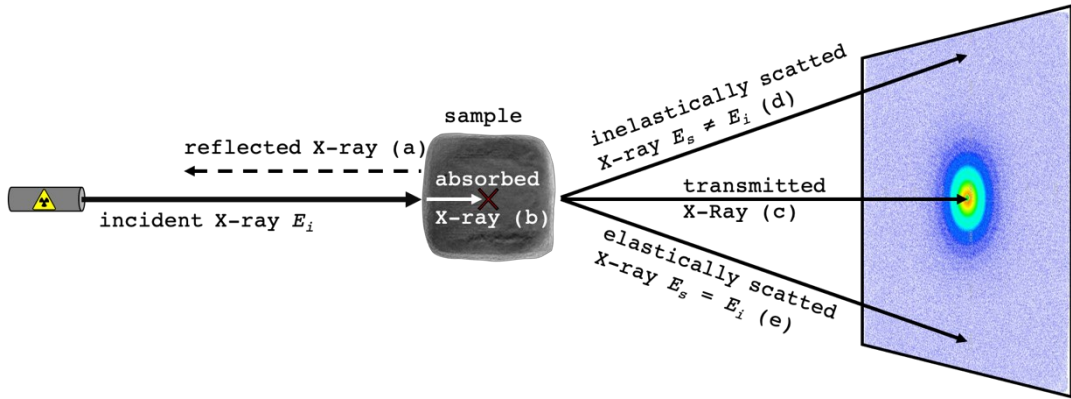


Figure 1: Schematic representation of the different ways X-rays can interact with matter: (a) reflection, (b) absorption, (c) transmission, (d) inelastic and (e) elastic scattering. Figure redrawn from the original in [20]

2.1. Scattering Theory

X-rays can be treated as photons or as electromagnetic waves with a wavelength in the Ångstrom range, this allows the analysis of structures down to atomic distances. When treated as electromagnetic waves there is an electric \mathbf{E} and magnetic field \mathbf{H} oscillating perpendicular to the direction of propagation of the wave. To simplify, the magnetic field will be neglected in the following elaboration and only the electric field will be considered. The oscillating electric field can mathematically be described using a sine wave or the more compact complex form

$$\mathbf{A}(\mathbf{r}, t) = A_i e^{i(\mathbf{k} \cdot \mathbf{r} - \omega t)} \quad \text{Equation 1}$$

where A_i denotes the initial amplitude of the electric field \mathbf{E} , \mathbf{k} is the wavevector ($k = 2\pi/\lambda$) and ω is the angular frequency. [18] [21]

As mentioned before, there are numerous ways a photon can interact with matter, one of them being scattering. A scattering event involves the change of trajectory of the wave, as a result of the interaction with matter. This change of trajectory is closely related to the structure and composition of the material. Furthermore, elastic and inelastic scattering need to be distinguished. A scattering event is considered to be elastic if the energy is preserved during the scattering event, whereas there is a change in energy with inelastic scattering events, as illustrated in **Figure 1**. The energy E of a wave with a frequency ν can be calculated as [4] [5]

$$E = h\nu = \hbar\omega \quad \text{Equation 2}$$

where h is the Planck constant and \hbar is the reduced Planck constant. [22] The direction of propagation is given by the beforementioned wave vector \mathbf{k} . As the scattering event leads to a change in the direction of propagation by 2θ , the wave vector \mathbf{k} also changes, according to **Figure 2a**. This change in direction is called scattering vector \mathbf{q} [4] [5] [16]

$$\mathbf{q} = \mathbf{k}_s - \mathbf{k}_i \quad \text{Equation 3}$$

where \mathbf{k}_i denotes the wavevector before the scattering event (initial) and \mathbf{k}_s is the wavevector after the scattering event (scattered), as shown in **Figure 2a**. In the case of inelastic scattering the scattering event changes the absolute values of the wavevectors ($|\mathbf{k}_i| \neq |\mathbf{k}_s|$), whereas the absolute values are unchanged during an elastic scattering event ($|\mathbf{k}_i| = |\mathbf{k}_s|$). [4] [5]

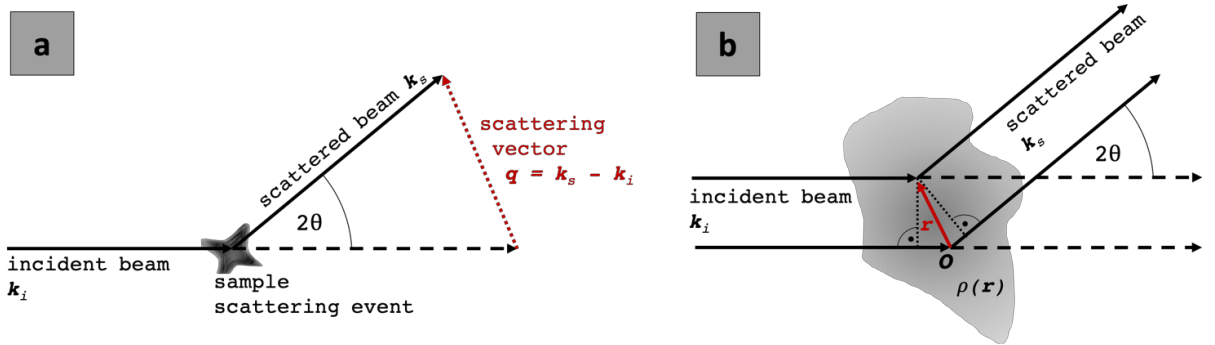


Figure 2: (a) Schematic representation of a scattering event illustrating the definition of the scattering vector \mathbf{q} . The incident beam \mathbf{k}_i is scattered by the scattering angle 2θ , resulting in the scattered beam \mathbf{k}_s . (b) A wave with wavevector \mathbf{k}_i is scattered to the direction given by \mathbf{k}_s , resulting in a phase difference between a wave scattered at two different spots, the origin O and position $O + \mathbf{r}$, in $\rho(\mathbf{r})$. Figures redrawn from the original in [21]

In the following only a purely classical model will be used to discuss the scattering theory, therefore the electron distribution can be described by a number density $\rho(\mathbf{r})$, where \mathbf{r} is the vector indicating the position of an individual charge. Furthermore, it can be assumed that the biggest part of the X-rays penetrates the sample without being scattered in the first place (transmission beam (c) in **Figure 1**) and we can therefore adopt the *Born Approximation*. The *Born Approximation* states that interaction of the scattered wave with charges can be neglected and with that also the possibility of the scattered wave being scattered again [23]. Then the total

scattering is the superposition of X-rays being scattered at all the different volume elements in this electron distribution $\rho(\mathbf{r})$. **Figure 2b** shows two waves scattered at different positions in $\rho(\mathbf{r})$, namely the origin \mathbf{O} and position $\mathbf{O} + \mathbf{r}$, resulting in a phase difference [4] [5]

$$\Delta\phi(\mathbf{r}) = (\mathbf{k}_i - \mathbf{k}_s) \cdot \mathbf{r} = \mathbf{q} \cdot \mathbf{r} \quad \text{Equation 4}$$

where \mathbf{q} is the beforementioned scattering vector, sometimes also referred to as wavevector transfer. If the wavelength λ is known the scattering vector \mathbf{q} can be related to the scattering angle 2θ [16]

$$q = |\mathbf{q}| = \frac{4\pi \sin(\theta)}{\lambda} \quad \text{Equation 5}$$

This relationship is especially important, as SAXS data is usually shown as intensity plotted over the scattering vector \mathbf{q} and powder XRD data as intensity over the scattering angle 2θ . The intensity $I(\mathbf{q})$ is proportional to the squared amplitude of the wave $A(\mathbf{q})$, which in reciprocal space (from now on referred to as q space) is defined as

$$I(\mathbf{q}) = A(\mathbf{q}) \cdot A(\mathbf{q})^* \quad \text{Equation 6}$$

where $A(\mathbf{q})^*$ is the complex conjugate of $A(\mathbf{q})$. The scattering amplitude $A(\mathbf{q})$ can be calculated from the Fourier transformation of the electron density $\rho(\mathbf{r})$ [16]

$$A(\mathbf{q}) = \int_0^V \rho(\mathbf{r}) \exp(-i\mathbf{q} \cdot \mathbf{r}) d\mathbf{r} \quad \text{Equation 7}$$

It is important to notice, that only if there is a difference in the electron distribution $\rho(\mathbf{r})$ a signal will be detected. This is why, actually, the difference in the electron density $\Delta\rho(\mathbf{r})$, is of interest here. E.g. the electron density difference between the scattering object (for example the NCs) and the overall mean density. [17]

The intensity of the scattered wave for two electrons as a function of the scattering vector \mathbf{q} can be calculated using

$$I(\mathbf{q}) = 2r_0(1 + \cos(\mathbf{q} \cdot \mathbf{r})) \quad \text{Equation 8}$$

If more than two electrons shall be described, it would be convenient to use the angle between \mathbf{q} and \mathbf{r} . Between the two there usually is a random orientation. Peter Debye suggested using a spherical average of all angles [24]. First the angle θ between the two directions needs to be defined ($\mathbf{q} \cdot \mathbf{r} = q \cdot r \cdot \cos(\theta)$). Then, using the non-integral form of Equation 8 for N electrons ($A(\mathbf{q}) = r_0 \sum_0^N \exp(-i\mathbf{q}\mathbf{r}_j)$) [21] for $N=2$ electrons having scattering amplitudes f_1 and f_2 and a distance \mathbf{r} , the amplitude of the scattered wave is calculated as

$$A(\mathbf{q}) = f_1 + f_2 \cdot \exp(-i\mathbf{q}\mathbf{r}) \quad \text{Equation 9}$$

Introducing Equation 9 into Equation 6 yields the intensity of the scattered wave as

$$I(\mathbf{q}) = f_1^2 + f_2^2 + f_1 f_2 \cdot \exp(i\mathbf{q}\mathbf{r}) + f_1 f_2 \cdot \exp(-i\mathbf{q}\mathbf{r}) \quad \text{Equation 10}$$

Assuming \mathbf{r} as a fixed, but randomly oriented distance the latter two terms of Equation 10 can be condensed, yielding

$$\langle I(\mathbf{q}) \rangle = f_1^2 + f_2^2 + 2f_1f_2 \cdot \langle \exp(i\mathbf{q}\mathbf{r}) \rangle \quad \text{Equation 11}$$

The angle bracket in Equation 11 indicates the spherical or orientational average of the ensemble. Using the previously defined angle θ between the two directions \mathbf{q} and \mathbf{r} the term $\langle \exp(i\mathbf{q}\mathbf{r}) \rangle$ can be rewritten as

$$\begin{aligned} \langle \exp(i\mathbf{q}\mathbf{r}) \rangle_{orient.av.} &= \frac{1}{4\pi} \int \int \exp(i\mathbf{q}\mathbf{r} \cdot \cos(\theta)) \cdot \sin(\theta) \cdot d\theta d\varphi = \\ &= \frac{\sin(qr)}{qr} \end{aligned} \quad \text{Equation 12}$$

The scattering intensity of any system with N scattering points, that all have an individual scattering amplitude described by f_i and are separated by a distance r_{jk} ($r_{jk} = |\mathbf{r}_j - \mathbf{r}_k|$) can be calculated using

$$\langle I(\mathbf{q}) \rangle = \sum_{j=0}^N \sum_{k \neq j}^N f_j f_k \frac{\sin(qr_{jk})}{qr_{jk}} \quad \text{Equation 13}$$

also known as *Debye Equation*. [18] [21] [24]

2.2. Small Angle X-Ray Scattering

SAXS is a powerful tool to study particles on the sub-nanoscale, by recording the elastically scattered X-rays at very low angles (usually between 0.1° and 10°). It is this angular range that contains the information on the size and shape of the nanoparticles or nanocrystals. This has to do with the reciprocal nature of all scattering processes, resulting in an inverse relation between the NC size and the scattering angle. This is best illustrated by the Bragg Equation [25]

$$n \lambda = 2 d \sin(\theta) \quad \text{Equation 14}$$

NCs, consisting of a vast number of atoms, are usually between some ten to a couple of thousand Å in size, so vastly larger than the wavelength of the most commonly used X-ray source (Cu K α ~ 1.54 Å), resulting in a small angular range of the scattering signal. Information on the structure can be obtained for particles in the range from ~ 0.5 to ~ 100 nm, depending on the resolution of the system, which in itself depends on a number of factors, e.g. photon energy, sample detector-distance (SDD), detector pixel size and size of the beam stop to name only a few. A schematic representation of a SAXS setup is given in **Figure 3**, where most of those influencing factors are depicted. [16] [17] [26]

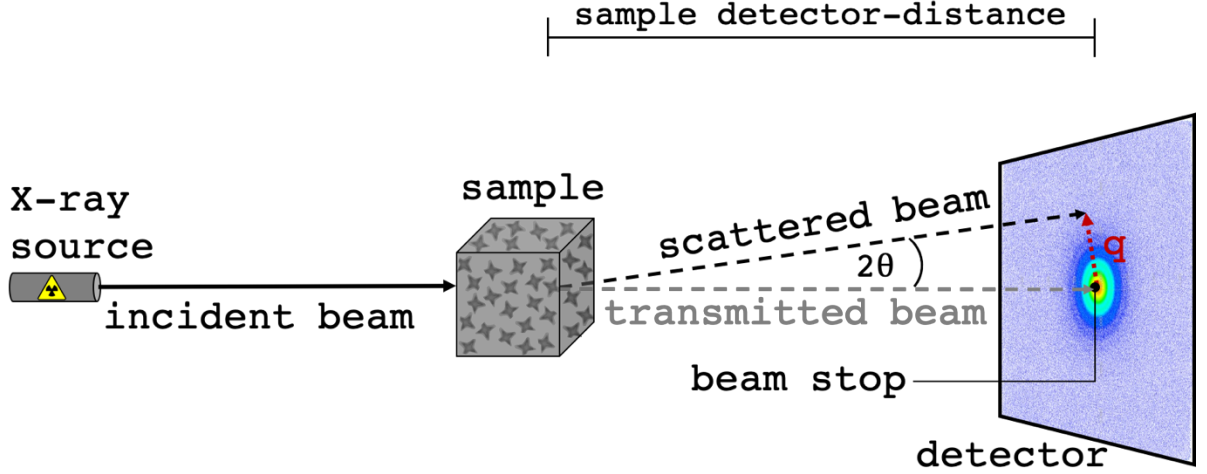


Figure 3: Schematic representation of a basic SAXS setup, illustrating the pathway of the X-ray beam, the beam stop, the scattering angle 2θ , the scattering vector \mathbf{q} and the sample detector-distance SDD. Figure redrawn from the original in [16]

Combining Equation 5 and the Bragg Equation (Equation 14) yields one of the most convenient equation for SAXS users, as it allows for a “quick and dirty” estimate of the NC size directly from the position of extrema in the scattering curve [27]

$$d = \frac{2\pi}{q} \quad \text{Equation 15}$$

If there is *a priori* knowledge of the NC size, the necessary q range can be estimated using Equation 15 and the SDD can be changed accordingly, as of cause the SDD has a great impact on the accessible q range. If a very wide q range is necessary, there also is the option of conducting the same measurement using different SDDs and subsequently merging the scattering curves.

The scattering intensity for N identical (size and shape) particles with the Volume V_p in a diluted system can be calculated as

$$I(\mathbf{q}) = N \cdot V_p^2 \cdot |F(\mathbf{q})|^2 \cdot S(\mathbf{q}) \quad \text{Equation 16}$$

with the *formfactor* $F(\mathbf{q})$ and the *structure factor* $S(\mathbf{q})$. The structure factor describes the interaction of the particles. For a diluted system, where all particles are far apart and there is basically no interaction to be accounted for, one can write $S(\mathbf{q}) = 1$. The formfactor depends solely on the morphology (size and shape) of the particles and for $q \rightarrow 0$ the formfactor yields $F(\mathbf{q}) = 1$. It can be calculated using

$$F(\mathbf{q}) = \frac{1}{V_p} \int_{V_p} \exp(i\mathbf{q} \cdot \mathbf{r}) dV_p \quad \text{Equation 17}$$

An analytical calculation of the formfactor is feasible, however only for the uttermost simple cases. When the analytical calculation is no longer possible, one has to fall back on the numerical evaluation of the integrals. [21] [27]

2.3. Small Angle X-Ray Scattering Data Analysis

In order to perform proper data preparation of SAXS data, a solid understanding of the theory behind is imperative. The aim of the following pages is to give the reader a fundamental knowledge of the theory behind SAXS scattering curves and the information that can be extracted from the scattering curves.

2.3.1. Guinier Analysis

In the long wavelength limit $qR \rightarrow 0$ it can be shown (for the exact derivation consult [21]) that the scattering intensity of a particle with the radius R can be calculated as

$$I(\mathbf{q}) \approx \Delta\rho^2 V_p^2 \exp\left(-\frac{\mathbf{q}^2 R^2}{5}\right) \quad \text{Equation 18}$$

Therefore, by plotting the intensity $I(\mathbf{q})$ logarithmically over the scattering vector squared \mathbf{q}^2 a linear fit could be obtained with a slope equal to $-R^2/5$. If the Guinier Analysis is to be applied to the scattering signal of a system of diluted, not perfectly spherical particles, the size can no longer be measured by the radius. Instead, a more general measure of the particle size needs to be introduced, the radius of gyration R_g . The radius of gyration is the square-root of the mass average of the particle. [28] It can mathematically be described as

$$R_g = \frac{1}{V_p} \int_{V_p} r^2 dV_p \quad \text{Equation 19}$$

and usually the integrals can only be solved numerically, but for a sphere a very simple solution can be found: $R_g^2 = \frac{3}{5} R^2$ This means that Equation 18 can be rewritten to yield

$$I(\mathbf{q}) \approx \Delta\rho^2 V_p^2 \exp\left(-\frac{\mathbf{q}^2 R_g^2}{3}\right) \quad \text{Equation 20}$$

This not only allows for a fast estimate of the approximate size and shape of the particles from visual analysis, but is also suited for automated analysis [29]. Because the analysis method is called Guinier Analysis the long wavelength limit is also referred to as Guinier regime. [21]

2.3.2. Porod Analysis

Whilst the Guinier Analysis operates in the long wavelength limit ($qR \rightarrow 0$), the Porod Analysis operates on the exact opposite of the scale, the short wavelength limit $qR \gg 1$. It is important to note that this is still a lot larger than the inner atomic spacing. Calculating the scattering intensity for a spherical particle with Volume V_p and surface area S_p one can use

$$I(\mathbf{q}) = \frac{2\pi\Delta\rho^2}{q^4} S_p \quad \text{Equation 21}$$

From Equation 21 one can conclude that in the long wavelength limit of SAXS the signal is proportional to the surface of the particles. As before the short wavelength limit has another name referring to its analysis method, the Porod regime. [21]

Figure 4 gives an overview of the position of Guinier and Porod regime in the q range with a schematic representation of three different scattering curves for three different particle shapes. There is a third regime mentioned in **Figure 4**, the Fourier regime, containing information on the shape of the particles. This regime will be the focus of the following chapter.

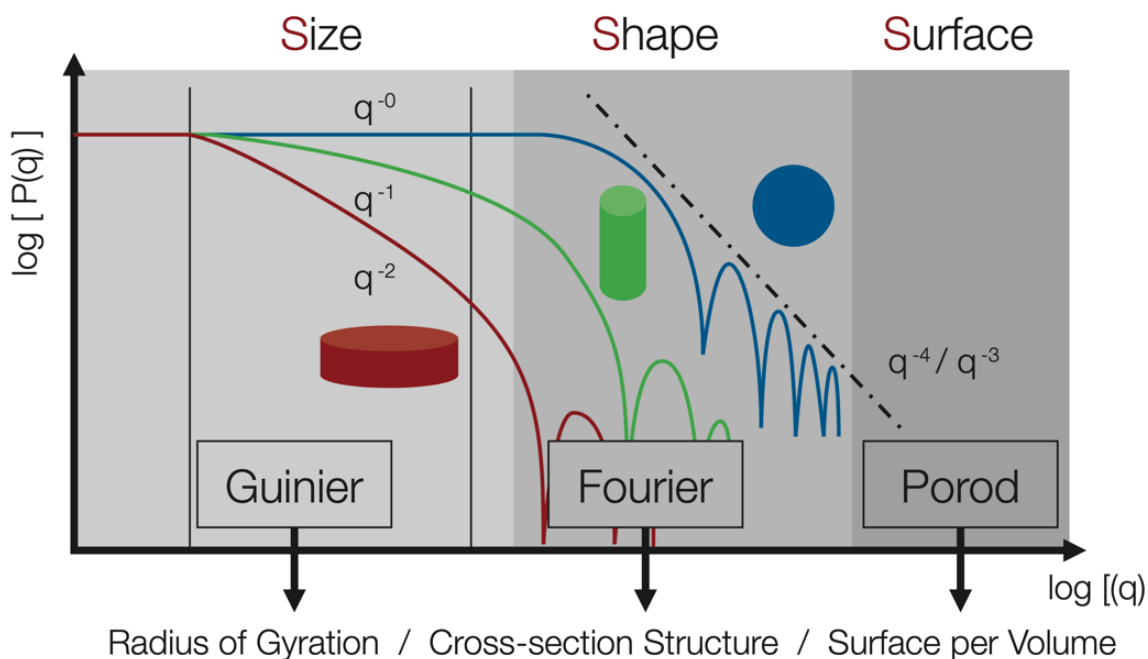


Figure 4: The Guinier, Fourier and Porod regime with an approximate location in the q range and the information that can be extracted from the corresponding regime. Additionally, there are three schematic scattering curves for different particle shapes, namely a disc (full red line), a cylinder (full green line) and a sphere (full blue line). Taken from [26]

2.3.3. From SAXS Data to the Shape of a Particle

From the name, and if that is not convincing enough then from Equation 17, it should be clear that the formfactor $F(q)$ strongly depends on the particle shape. Calculating the formfactor for a three-dimensional shape involves integrating over the particle volume V_p . As mentioned before this is analytically really only possible for a few selected particle shapes, for all other shapes the formfactor is calculated numerically. The formfactor squared $F(q)^2$, radius of gyration R_g and Porod exponent n for the three shapes shown in **Figure 4** (disc, cylinder and sphere) are summarised in **Table 1**.

For the infinite number of shapes for which a numerical calculation is necessary, it is best to use a slightly modified version of the Debye Equation (Equation 13), where the particle consist of N individual scatterers with individual formfactors F_i , located at r_i .

As any complex shape can be reconstructed as an assemblage of geometrically simpler shapes, this is the preferred way to compute the scattering signal for complex shapes and is therefore of great importance for this work. [5] [21]

Table 1: Summarisation of the squared formfactor $F(q)^2$, the radius of gyration R_g and the Porod exponent n . The three parameters are shown for a sphere with radius R , an infinitely thin disc of radius R and an infinitely thin cylinder with length L , sometimes also referred to as rod. Due to lack of space two abbreviations are used: $Si(x)$ is the sine integral $\int_0^x \sin(t)/t dt$ and $J_1(x)$ is a Bessel function $(\sin(x) - x \cdot \cos(x))/x^2$. [21]

	Formfactor squared $F(q)^2$	Radius of gyration R_g	Porod exponent n
Sphere ($d = 3$)	$\left(\frac{3J_1(qR)}{qR}\right)^2$	$\sqrt{\frac{3}{5}} R$	-4
Disc ($d = 2$)	$\frac{2}{q^2 R^2} \left(1 - \frac{3J_1(qR)}{qR}\right)$	$\sqrt{\frac{1}{2}} R$	-2
Cylinder ($d = 1$)	$\frac{2Si(qL)}{qL} - \frac{4 \sin^2(qL/2)}{q^2 L^2}$	$\sqrt{\frac{1}{12}} R$	-1

Another approach for describing complex geometries is the Pair Distance Distribution Function (PDDF) or $p(r)$ proposed by Glatter [30]. It is mainly used to analyse the oscillating part of the scattering curve, which is often referred to as Fourier regime as can be seen in **Figure 4**. It is basically a transformation from reciprocal space $I(q)$ to real space $p(r)$ by performing a Fourier-transformation via

$$I(q) = 4\pi \int_0^{\infty} p(r) \frac{\sin(qr)}{qr} dr \quad \text{Equation 22}$$

The PDDF shows all the distances that can be found inside the particle by plotting the frequency of a certain distance over said distance. This distribution holds a lot of information not only on the particle size, but also its shape. The PDDFs for some characteristic shapes are shown in **Figure 5**, illustrating the possibility of differentiating between a spherical, cylindrical and disc like shape just from the PDDF. In **Figure 4** the corresponding scattering curves $I(q)$ are depicted. The Fourier-transformation works bilateral, making it possible to calculate the PDDF directly from the scattering curve $I(q)$ [26] [30] [31]

$$p(r) = \frac{1}{2\pi^2} \int I(q) qr \sin(qr) dq \quad \text{Equation 23}$$

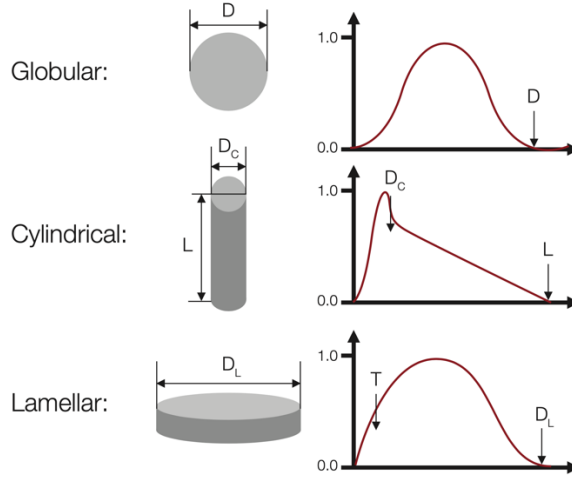


Figure 5: The PDDF or $p(r)$ shown for three different shapes, indicating how easily the shape of a spherical, cylindrical or disc like sample can be estimated from the PDDF. The corresponding scattering curves were shown before. Taken from [26]

2.4. Shape Retrieval

In the chapters so far, the assumption was made that there is *a priori* knowledge of the electron density of the analysed system, which can then be used to calculate the scattering intensity using the derived equations. In reality however, it is the other way around. The scattering intensity is measured in form of the scattering curve and then from this the electron density is to be calculated. Furthermore, in a real-world system only the orientational averaged intensity is measured, leading to a massive loss of information. Retrieving the shape of a measured particle, therefore is a long and complex iterative process that requires a deep understanding of the scattering theory discussed in the preceding chapters.

In a first step the scattering intensity of an initial model $I^{calc}(q)$ is calculated and compared to the measured experimental intensity $I^{exp}(q)$ via

$$\chi^2 = \frac{1}{N_{exp}} \sum_{m=1}^N \left(\frac{I^{exp}(q) - I^{calc}(q)}{\sigma_{exp}(q)} \right)^2 \quad \text{Equation 24}$$

where N_{exp} denotes the number of experimental data points with the experimental error $\sigma_{exp}(q)$. Minimising the chi squared functional χ^2 (often referred to as objective function) is the main objective of any shape retrieval process. [6]

2.4.1. Simulated Annealing

Generally speaking, the fundamental idea behind this minimisation is to continuously alter an initial starting shape until the best agreement between $I^{exp}(q)$ and $I^{calc}(q)$ is found. In order to minimise the chi squared functional different metaheuristic approaches exist, e.g. *Simulated Annealing* proposed by Kirkpatrick *et al.* in [32] or *Genetic Algorithms* proposed by

Mitchell [33] [34]. This chapter will focus on simulated annealing, as it is similar to those used by both software packages appearing later in this work.

Simulated annealing uses an iterative improvement approach. It starts with a predefined starting configuration (in the case of shape retrieval often a spherical or cubic starting model), then it applies a standard rearrangement operation to the configuration and calculates the objective function. It compares the objective function of the original and the new configuration and if the objective function of the new configuration is lower, the new configuration becomes the starting point of the next step. This step is repeated until no further improvement can be found. However, if only steps that lower the objective function are allowed, this is the simulation equivalent of rapidly quenching a material to low temperatures, usually resulting in metastable solutions. As temperature does not have an equivalent in the world of computational optimisation, an *effective temperature* was introduced by Kirkpatrick *et al.* acting as a control parameter of the annealing process. To counteract the quenching effect, Metropolis *et al.* [35] introduced a procedure, that also allows for uphill steps under certain conditions. As before, there is a small random rearrangement of the system performed every step, after which the change in the objective function $\Delta\chi^2$ is calculated. In the case of a lower objective function $\Delta\chi^2 < 0$, the displacement is accepted and the new configuration is used as the starting point of the next step. If the objective function increases $\Delta\chi^2 > 0$ the probability of it being accepted is calculated in the means of Boltzmann statistics $P(\Delta\chi^2) = \exp(-\Delta\chi/k_b T)$. The simulated annealing starts with a high effective temperature T , the equivalent of melting the system, and slowly lowers the effective temperature step by step until no further changes are possible, the equivalent of a frozen system. [32] [35]

2.4.2. The Loss of Information due to Random Orientation

The resolution of SAS data regarding the structure is a lot worse than that of data from diffraction of single crystals. This loss of information is linked to the random orientation of particles in a solution and has nothing to do with the phase problem. Additionally, the loss of information due to random orientation is greater than the loss because of the phase problem. To account for the fact that a SAXS signal does not depend on the particle orientation, the introduction of a scattering multipole $\rho(\mathbf{r})$ with rotational properties in the form of spherical harmonics Y is suggested by Stuhrmann [36]. This way the multipole can be described as

$$\rho(\mathbf{r}) = \sum_{l=0}^{\infty} \sum_{m=-l}^l \rho_{lm}(r) Y_{lm}(\theta, \varphi) \quad \text{Equation 25}$$

in real space. The coefficient $\rho_{lm}(r)$ are the multipole components of the field $\rho(\mathbf{r})$ and are calculated as

$$\rho_{lm}(r) = \int Y_{lm}^*(\omega) \rho(\mathbf{r}) d\omega . d\omega = \sin(\theta) d\theta d\varphi \quad \text{Equation 26}$$

using the spherical harmonic complex conjugate Y_{lm}^* , which is only dependent on the angle ω .

Using this information, the scattering amplitude can be written as

$$A_{lm}(r) = \sqrt{\frac{2}{\pi}} i^l \int \rho_{lm}(r) j_l(qr) r^2 dr \quad \text{Equation 27}$$

where $j_l(qr)$ denotes the spherical Bessel function of l^{th} kind. All things combined, the scattering intensity $I(q)$ can then be calculated using A_{lm}^* and the complex conjugate A_{lm}^*

$$I(q) = \frac{1}{4\pi} \sum_{l=0}^L \sum_{l=-m}^l A_{lm}(q) A_{lm}^*(q) \quad \text{Equation 28}$$

This equation is similar to the beforementioned Debye Equation (Equation 13), with the difference that now the sum does not need to be calculated for all particles N , but all harmonics L . This takes significantly less effort in terms of calculating effort. If the calculation of the scattering intensity $I(q)$ has to be calculated many times, like in the simulated annealing procedure above, this helps drastically speed up the process. [19] [36] [37]

Despite the complexity of the abovementioned equations, the relevance of their statement for shape retrieval can also be described without using a single equation. First a structure can be split into angular regions. If in the process of e.g. simulated annealing the only change made to a model is in one of those regions, it is no longer necessary to again calculate the scattering intensity of the entire model, but rather it is sufficient to calculate the corresponding multipole. This additionally helps to reduce the computing time for a model. [19]

2.4.3. Retrieving the Shape

The most common method to study the size and shape of NCs is transmission electron microscopy, with which it is possible to reach single-atom resolution. However, TEM comes connected to numerous severe drawbacks. As a TEM image is only resolvable in the focusing plane of the microscope, all information on the shape perpendicular to the focusing plane is lost. Whilst this problem can be bypassed by using electron tomography, the problem that quality TEM images can only be made of a few hundred NCs at once at absolute maximum remains. [5] Using SAXS the probed sample usually contains at least 10^6 NCs, sometimes even up to 10^{11} , all of them interacting with the X-ray photons and therefore contributing to the SAXS signal. Therefore, the number of NCs analysed is larger by an incredibly big margin.

The idea of reconstructing a 3D model from SAXS scattering curves was first brought up in the 1960s. At first the scattering curves of simple geometries were calculated in a trial-and-error approach and compared to experimental data. From this a general idea of the approximate shape was acquired. Advances like Stuhmann's idea to use spherical harmonics [36] (see above) allowed for a faster calculation of the scattering curve of a given structure. The final breakthrough came with the idea of an *ab initio* approach using automated bead modelling. This approach is also used by today's most popular shape retrieval program DAMMIN and DAMMIF [15]. The shape is represented by a dense conglomeration of beads or dummy atoms

(DAs) (the two terms can be used synonymously) that is slowly modified using simulated annealing to find a configuration that minimised the objective function. As *ab initio* methods do not result in a unique solution, building multiple individual models, comparing and averaging them is advised (for example using DAMAVER [15]). [12]

A different approach from Glatter suggests performing an indirect Fourier-transformation (IFT) of the scattering curve. For the scattering curves from diluted NCs this results in a desmeared and smoothed PDDF. [30] If there is a superimposed Structure Factor $S(\mathbf{q})$, the next step could be to perform a generalised indirect Fourier-transformation (GIFT) and then the structure factor of the system can be calculated. [31] [38]

The different shape retrieval software packages are most commonly used to study proteins, strictly monodisperse systems. This is where the biggest disadvantage of *ab initio* based shape retrieval methods stems from, its theoretical limitation to strictly monodisperse system. However, the applicability of *ab initio* shape retrieval methods for slightly polydisperse systems has been proven. [5]

3. Experimental

The aim of this chapter is to give the reader a concise overview of the techniques used to generate the data analysed later in this work. Only little focus is placed on the synthesis of the samples, as this step was performed by collaborators at the University of Hamburg in Germany and would exceed the scope of this work.

3.1. Sample preparation

The samples were synthesised by Dr. Artur Feld and Dr. Agnes Weimer, members of the group of Prof. Dr. Horst Weller at the University of Hamburg. All TEM images in this work are taken from [8].

The NC synthesis was started by synthesising iron(II)oleate and iron(III)oleate. This was done by mixing purified FeCO_3 salt and $\text{Fe}_2(\text{CO}_3)_3$ salt respectively with oleic acid (OA) in a Fe:OA ratio of 1:7 at room temperature (RT). Subsequently, the mixture was heated to 60°C and stirred at that temperature for 1 h and then cooled down to RT again. At RT the mixture was stirred for an additional 24 h until a milky grey emulsion had formed. By heating the sample to 60°C under vacuum for 2 h, water and CO_2 were removed. To fully remove the remaining water, the emulsion was heated to 120°C under vacuum for 1 - 2 h. Finally, the NCs were synthesised by thermal decomposition of iron(II)oleate and iron(III)oleate. By varying temperature and reaction time the morphology of the NCs can be altered. For this work four different samples were created and labelled FeO 4, FeO 6, FeO 14 and FeO E. Whilst the shape of sample FeO 4 is best described as star-like, the shape of sample FeO E is cubic. Sample FeO 6 and FeO 14 are in between. The shapes of all four samples are shown in **Figure 6**. The final NCs from both the iron(II)oleate and iron(III)oleate iron source, result in a purely wustite (FeO) structure. [8] For more information on the synthesis of the samples please consult [8].

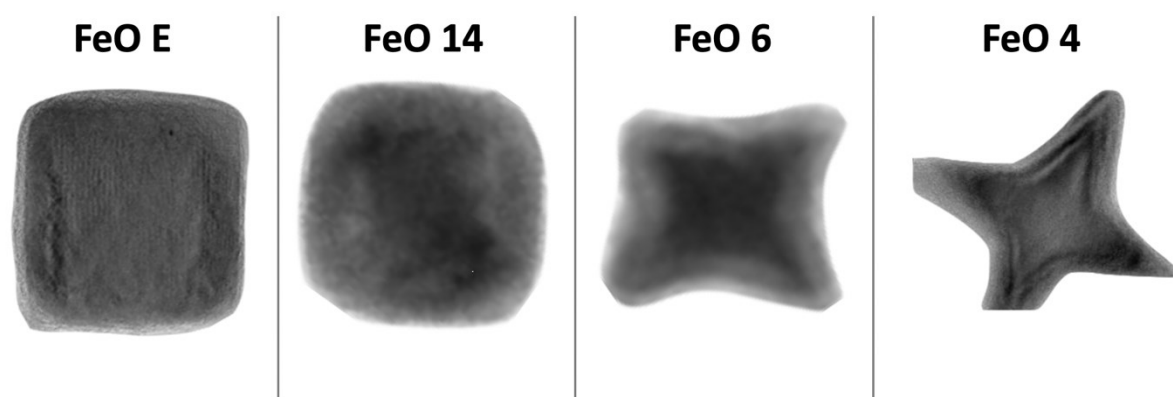


Figure 6: Comparison of a TEM image of a representative NC of all four prepared samples. FeO E represents the most cubic sample and will often be referred to as a cube. FeO 14 can best be described as a cube with more rounded edges. FeO 6 is a cube with concave faces. The shape of FeO 4 can best be describes as star-like. Individual TEM images taken from [8].

The FeO NCs are so called superparamagnetic iron oxide nanocrystals and exhibit exceptional magnetic properties. These magnetic properties, however, strongly depend on the size and shape of the NCs. The size determines the saturation magnetisation and whether the NCs are superparamagnetic or ferromagnetic. The shape allows the alternation of additional magnetic properties, such as the blocking temperature and biocompatibility. [8] [9]

The NCs were diluted in toluene and a small amount of oleic acid was added to prevent aggregation. Upon arrival at our lab the samples and the toluene solvent were transferred into quartz capillaries with a stated wall thickness of 0.1 mm using a sterile syringe and needle. To prevent the samples from evaporating due to the vacuum in the sample chamber, the capillaries were sealed using a two-component epoxy adhesive and then left to harden. The dried epoxy adhesive was subsequently covered with an additional layer of wax. From the concentration of 8 to 12 mg/ml, the 300 μm diameter of the X-ray beam and the 1.5 mm capillary diameter the average number of NCs illuminated by the X-ray beam in the capillary can be approximated to be $9 \cdot 10^{10}$, which corresponds to a volume fraction of approx. 0.18%.

3.2. Measurements

All measurements were performed at the Montanuniversität Leoben, adhering to the highest safety standards.

3.2.1. Small Angle X-Ray Scattering Measurements

The capillaries containing the four diluted NCs, a capillary containing pure toluene and a capillary containing the calibrant were placed inside the sample chamber of the SAXS device. For this work a *Bruker Nanostar*, using a Cu K α source with a wavelength of 1.5418 Å and two 300 μm *SCATEX* collimators, was used. Silver behenate is used as the calibrant due to its large number of sharp peaks in the range below 20° 2-theta. [39] The calibrant is used during analysis to determine the exact SDD (see **Figure 3**). After evacuating the sample chamber, a number of x- and y-scans were performed to locate the exact positions of all six capillaries. Once the exact positions were located the measurement was started. The samples and solvent were measured three times for 4 hours at two different SDDs to yield the largest possible q range to the setup. The calibrant was measured once for 1 hour, also at two SDDs. The two SDDs used were approx. 25 cm and approx. 107 cm.

3.2.2. X-Ray Diffraction Measurements

In order to measure the dissolved NCs with XRD, the NCs needed to be dried first. This was done by heating a sample holder to approx. 50 °C and adding a small amount of sample step by step, making sure the solvent can evaporate before adding a new layer. In total four layers were added to the sample holder before it was placed inside the X-ray diffractometer. For this work a *Bruker D8 ADVANCE eco* was used, with a Cu K α source and a wavelength of 1.5418 Å. The samples were rotated continuously and measured for 11 hours between 5° and 130° 2θ ,

corresponding to a scattering vector q of 3.56 nm^{-1} and 73.87 nm^{-1} respectively. Converting from 2θ to q is done using Equation 5.

4. Analysis

Whilst SAXS measurements usually require only little time in the laboratory, processing the data to yield results is a considerably more elaborate process, that requires not only the appropriate software, but also a deep understanding of scattering theory.

4.1. Data processing

Before one can think about retrieving the shape of the NCs from the scattering data, there is a considerable amount of processing to do. This chapter will give a brief insight into the software used and the steps that are necessary to get the most out of the collected data.

4.1.1. SAXS Data

The 2D SAXS data was azimuthally integrated using *PeakFit 2D* to obtain the SAXS scattering curves. As every sample was measured three times, the three SAXS scattering curves were subsequently averaged using *PCG Tools*. Both *PeakFit 2D* and *PCG Tools* were developed by Gerhard Fritz Popovski, a member of our group.

Because the measurements were performed using two different SDDs, the two averaged scattering curves from the two SDDs had to be merged before the data could be further analysed. As shown in **Figure 7a**, a long SDD (in this case approx. 107 cm) yields a narrow q range with good resolution at low q , whereas a short SDD (in this case approx. 25 cm) yields a broader q range with a worse resolution at low q values. The data from the long distance is therefore best used to describe the low q range, and vice versa. However, for further analysis one file containing information on both the low and high q range is needed. Therefore, the files need to be merged, e.g. using *PCG Tools*. **Figure 7a**, **b** and **c** show the three steps involved in the averaging process. In the first step (**a**) the two scattering curves are plotted and compared. It can be seen, that the signal from the ~ 25 cm SDD has a considerably higher intensity than the signal from the ~ 107 cm SDD. Furthermore, there is a distinct difference in the resolution of the details in the q range up to 1 nm^{-1} , the minima are precisely defined in the ~ 107 cm signal and only loosely defined in the ~ 25 cm signal. In the second step (**b**) one of the two signals is shifted in its intensity (multiplied by a corresponding value), so that the curves overlap. Data points from the end of the ~ 107 cm signal and from the beginning of the ~ 25 cm signal are removed in step 3 (**c**), so that there is a smooth transition from one curve to the other. Finally, the files are merged, and a new file is created. All three steps can be performed using *PCG Tools*.

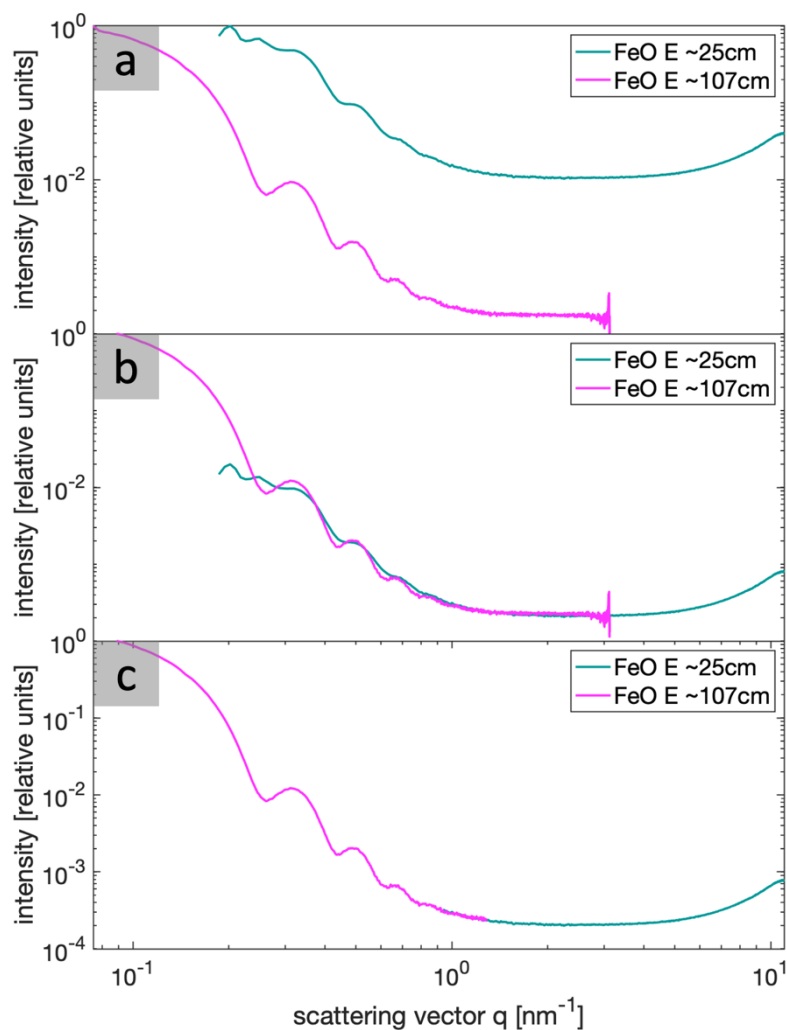


Figure 7: Visualisation of the three steps of the merging process of two SAXS curves recorded using two different sample-detector distances, in this case ~ 25 cm (full green line) and ~ 107 cm (full pink line). (a) Plotting the data with no adjustments made. (b) Adjusting the intensity values to create two overlapping curves. The difference in the resolution regarding the details in the q range below 1 nm^{-1} is clearly seen in this depiction. (c) Removing data points at the beginning (~ 107 cm data – pink line) and end (~ 25 cm data – green line) of the two curves.

The created files are the scattering curves (intensity plotted logarithmically over q), with a q range from approx. 0.1 nm^{-1} to approx. 11 nm^{-1} , of the NCs with the superimposed scattering of toluene and the capillary, the so-called background (noise). The background can be removed by subtracting the scattering curve of the toluene from the other scattering curves, leaving behind the pure scattering curve of the NCs. However, due to differences in transmission of the samples caused by small fluctuations in the concentration or varying diameters of the capillaries a transmission correction has to be performed before the subtraction can be performed. In the present case fluorescence from the iron in the NCs complicates the transmission correction. A simpler but equally effective way is to normalise the curves to the solvent peak at approx. 11 nm^{-1} , seen in **Figure 8a**. **Figure 8b** shows the low q range before the background removal. **Figure 8c** shows the scattering curves after the background was removed. The scattering

artefacts (e.g. maxima and minima) of the individual samples remain unchanged, however a change in the slope can be observed. The scattering curves shown in **Figure 8c** are the basis for all further analysis in this work from here on.

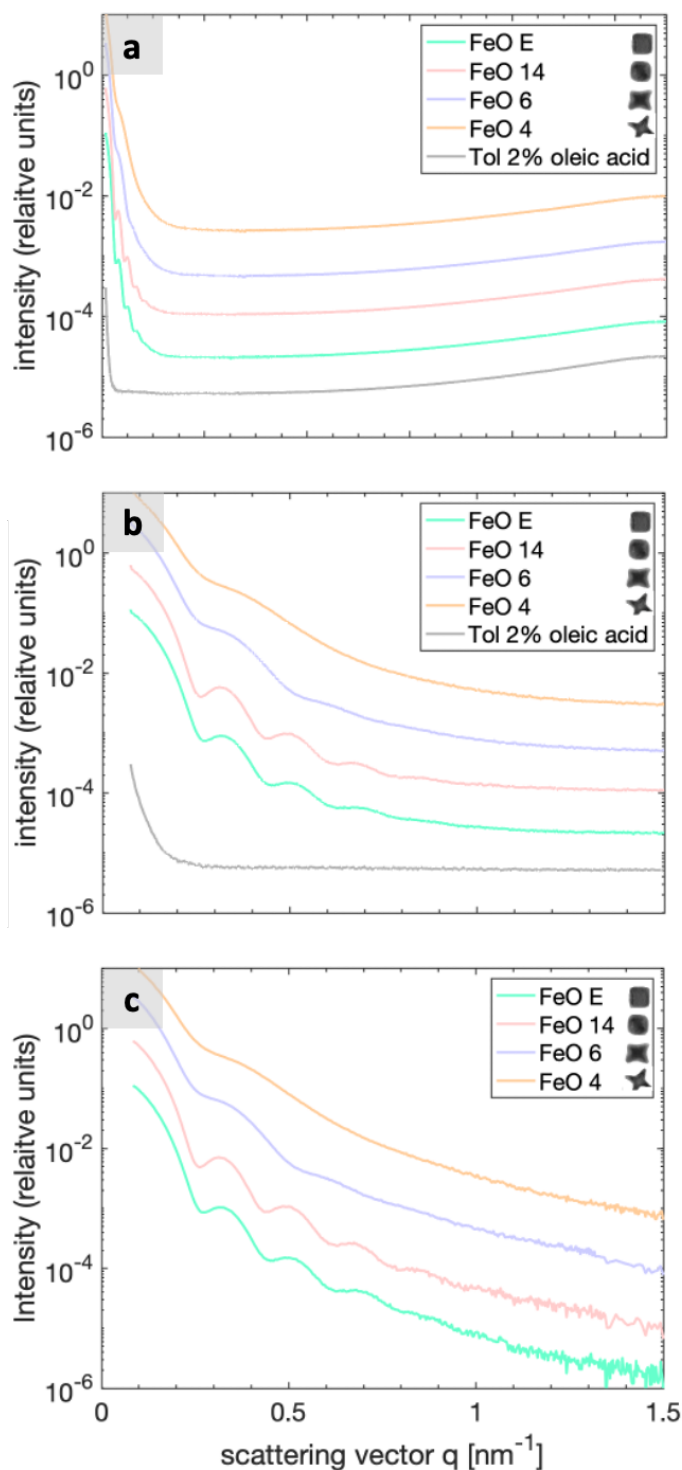


Figure 8: (a) Scattering curves of the four NCs – solid green line FeO E, solid pink line FeO 14, solid purple line FeO 6, solid orange line FeO 4 – with superimposed scattering from the background: the capillary and toluene (solid grey line). (b) Scattering curves of the four NCs with background shown for a narrower q range. (c) Scattering curves of the four NCs with subtracted background. Curves shifted vertically to aid readability.

4.1.2. XRD Data

The XRD patterns were Cu $k\alpha$ corrected and the peak positions were compared to the ones of standards of different oxidation states of iron. Additionally, the crystallite size can be extracted from the XRD pattern by analysing the full width at half maximum (FWHM) of the individual peaks. Moreover, the crystallite size can then be linked to a crystallographic direction. To determine the FWHM of the individual peaks, they are first fitted with a gaussian function, then the FWHM is extracted and finally the crystallite size is determined using Scherrer's Equation

$$D = \frac{b\lambda}{\beta(2\theta) \cos(\theta)} \quad \text{Equation 29}$$

where $\beta(2\theta)$ is the FWHM of the peak, given in the scattering angle two theta 2θ , λ is the wavelength (Cu $K\alpha$, approx. 1.5418 Å) and b is a constant close to 1. [42] [43] As it is good practice to present SAXS data as intensity over the scattering vector q and in this work, also the XRD data is given in q space due to the work's focus on SAXS, it would be preferable to also give the Scherrer equation in q space:

$$D = \frac{b2\pi}{\beta(q)} \quad \text{Equation 30}$$

where $\beta(q)$ is the FWHM of the peak, given in the scattering vector q . [40]

4.2. Shape Retrieval

Shape retrieval was performed using two different software packages: (a) SasHel [6] and (b) ATSAS [15].

- (a) SasHel is a bead modelling software capable of reproducing the shape of helical or rod-like systems by using the repetitive scheme of natural systems. Only a single building block is calculated and afterwards stacked. More important for this work, however, is the grid free approach of the SasHel algorithm. Contrary to other modern modelling programmes, the DAs do not have to move on an underlying grid during the simulation process. [6]
- (b) ATSAS is a software package delivering a vast number of different applications, from primary SAXS data processing to *ab initio* bead modelling. In this work the bead modelling software DAMMIF and DAMMIN were used. In contrast to SasHel they work with an underlying face centred cubic (FCC) grid, on which the DAs have to be placed. This difference is clearly visible and its consequences are addressed at a later point. Furthermore, DAMMIF and DAMMIN implement a support for the preselection of certain symmetries. [15]

4.2.1. Creating the models

The approach for both software packages is similar. The scattering curve is given as the input parameter. Subsequently further parameters are defined, such as the number of DAs used, looseness penalty, curve weighting options and the number of different simulations running simultaneously.

ATSAS

All input parameters for the ATSAS models, except the scattering curve obviously, were kept identical for the four samples. Two options are available in DAMMIF, “*fully automated processing*” or “*manual selection of parameters*”. The latter was used in this work. After the user determines the Guinier range and the PDDF, he is presented with a number of options. There are two modes available, “fast” and “slow”. The differences between these two are manifold, the most important ones for this work are the difference in DA size, effecting the total number of DAs used (approx. 10 000 in “slow” mode and only approx. 2 000 in “fast” mode) and the amount of iteration steps. [42] As there is no *a priori* knowledge of the NCs’ shape or on the degree of filigree details of the NCs, the number of DAs needed to be high in order to be prepared for both the simple and complex cases. Therefore, the “slow” mode is used. Next up the user can choose how many individual models should be simulated, in this work 15 models were created during every evaluation. DAMMIF further provides a selection of different symmetries. For this first evaluation, the symmetry was not predefined (option “*p1*”). Regarding the “Anisometry” and “Angular Scale” the option “unknow” was selected. Finally, the option of averaging the 15 individual models using DAMAVER was selected, the computation time for this step increases exponentially with the number of models being averaged. The averaging procedure is discussed in more detail in the next chapter.

Additionally, the shape retrieval process was performed with a predefined symmetry based on the outcomes of the models with no predefined symmetry. This step was performed to study the effect of symmetry on the final model. DAMMIN was used for the model with a predefined symmetry. The shape retrieval was performed using different predefined symmetries (*p432*, *p4* and *p8*), eight models were created and subsequently averaged using DAMAVER. As the starting model for the *p4* and *p8* symmetry a parallelepiped with edge length 50 nm was chosen, for the *p432* symmetry a sphere with diameter 50 nm was chosen. The parallelepiped was chosen based on the results from the foregoing analysis, whilst for *p432* only the sphere could be selected. The size of the starting model was approximated based on the maximum size in the PDDF with a fair bit added, as this had proven to deliver the best results. The remaining parameters were left unchanged.

SasHel

Once a set of successful parameters was found for SasHel, they were kept identical for all samples too. First a new model needs to be created, choosing both initial size and initial shape (cube, sphere, cylinder) of the model. To study SasHel’s ability of finding the right shape

without any *a priori* information, a sphere with a diameter of 45 nm was chosen (the size of the starting sphere was approximated from the maximum dimension in the PDDF). The number of DAs was set to 8 000. As mentioned before, SasHel has the ability to create stacked models, a feature that is of no relevance here. Therefore the “Nr. of Building Blocks” is set to 1. The DA size was left at its default setting (0.2 nm), the same is true for the “Starting Temp.,” “Delta Temp.,” “Iterations,” “Curve Weighing Options” and the “Advanced Fitting Parameters”. The number of models created simultaneously is depending on the number of CPU cores n_{CPU} . The recommended maximum number of models to fit simultaneously is $n_{CPU} - 1$ [42], in the case of the computer used for these simulations there were eight cores, so seven simulations were run simultaneously. The seven models were subsequently averaged using DAMAVER. Many models were created using both ATSAS and SasHel to fully develop an understanding of the influence of the different parameters on the resulting models.

4.2.2. Averaging the models

For the averaging process the software DAMAVER from the ATSAS package was used for models created with both SasHel and ATSAS. DAMAVER consist of a three-step averaging process using DAMSEL, DAMSUP, DAMAVER [15], which will be further elaborated in the following.

DAMSEL compares all input models and finds the most probable one and defines outliers by calculating and comparing the normalised spatial discrepancy (NSD), providing an quantitative estimate of the similarity of two or more models [43]. If the NSD value is above a certain threshold, the model will not be considered during the averaging process. DAMSUP aligns the models to a reference model, in this case the most probable one, again using the NSD. In the last step all aligned models are averaged using DAMAVER. This is done by remapping them onto a grid of closely packed DAs, which allows for the calculation of a frequency map, also referred to as occupancy. The occupancy hence gives the number of atoms on every lattice point placed over all the superimposed models. If, for example, 10 models are averaged with DAMAVER and the occupancy at a certain point on the grid is 10, this means that in every model a DA will be found on this lattice point. In the following always the normalised occupancy will be given.

As discussed earlier, DAMMIF works with an underlying FCC grid structure for placing the atoms during the simulation, whereas SasHel does not work with a grid and allows for unrestricted DA positions. That is why during the DAMAVER procedure there are never two DAs located on the same grid position, yielding a uniform occupancy for every DA in the model. As a consequence, it is harder to evaluate the accuracy and statistical validity of a model generated using SasHel.

4.3. Diameter Distribution

Apart from the shape, the dimension of NCs is of major importance. Of course, some information on the size can be extracted from the position of the minima in the scattering curve or by calculating the PDDF. In this chapter however, an alternative analysis of the NCs' dimension will be discussed. When looking at the size of averaged models composed out of many DAs smearing effects can be observed. As the models are built by many DAs with a defined radius r_{DA} , the resolution of this size analysis is limited by the size of those DAs. In addition to this the models are the result of an averaging process, resulting in an additional statistical smearing.

First the dimension along one direction of the particle is analysed. To do so, a measuring cylinder, with a length much bigger than the biggest dimension of the model and radius bigger than the radius of the DAs r_{DA} , is inserted through the model's centre of gravity. All DAs outside the measuring cylinder are ignored during analysis, the NCs inside the measuring cylinder are circled red in **Figure 9a**. **Figure 9b** shows the result of the first step of this analysis, the mean occupancy along a given direction inside the model (full black line), representing the electron density. The inside of any homogeneous particle displays a constant electron density, consequently the inner region can be fitted by a horizontal line averaging the fluctuations in the occupancy map. The fluctuations are caused by the individual DAs placed on the grid.

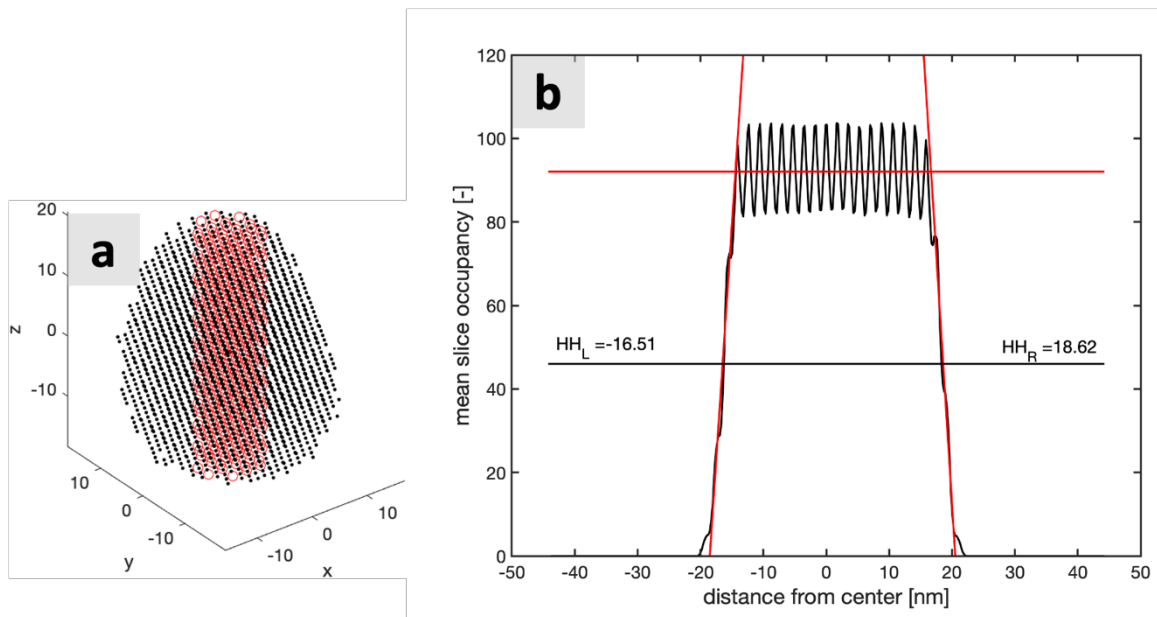


Figure 9: (a) 3D model representing a NC (full black dots), the DAs inside the measuring cylinder are circled red. The measuring cylinder has a radius of 5 nm. (b) Cross section showing the occupancy (full black line) along the measuring cylinder with, linearly fitted (full red line) to extract the half height dimension.

The edge, however, is where it starts to get more interesting. Despite smearing effects, a clear decision needs to be made on where the edge of the model is located. This is done by manually fitting the slopes on both sides and calculating the intersection with the horizontal line. The half-height dimension (HHD) is then defined as the diameter where the occupancy is exactly

half that of the horizontal line. **Figure 9b** shows two values HH_L and HH_R , adding the absolutes of these two values yields the HHD, in this case 35.13 nm. The slope on the edges is proportional to the polydispersity of the system. [19]

Evaluating the HHD along one single direction is a helpful tool for evaluating the size along characteristic dimensions of objects. In the case of cubes, e.g. the edge length can be determined. In the case of more complex or smeared shapes, the models cannot be described by a single characteristic dimension. It is therefore necessary to evaluate the dimension along a considerably larger number of directions. The procedure for evaluating the HHD along a single direction is automated and performed n times along randomly selected directions. [19] [31] For good statistics it is recommended to set $n > 10^5$. The outcome of this procedure is a kind of diameter distribution, that can be used to further study the models.

5. Results

All four NCs were modelled using the two software packages SasHel and ATSAS. As mentioned before no occupancy could be calculated for the SasHel models, making all analysis going beyond simple evaluation of the 3D model impossible. Consequently, this section will focus on the models created using ATSAS, whilst the SasHel models will be used for comparison only. Furthermore, the diameter distribution will be discussed. XRD measurements were performed to complement the results from the SAXS data and are also discussed in the following.

5.1. Shape Retrieval from SAXS Data

First the results of the ATSAS models will be discussed in detail and afterwards they will be compared to the SasHel models.

5.1.1. ATSAS models without predefined symmetry

Figure 10 shows the fits of the four models FeO E (**a**), FeO 14 (**b**), FeO 6 (**c**) and FeO 4 (**d**) in comparison to the experimental data. The fits are in very good accordance with the experimental data. Only for FeO E there is a slight deviation in the range of the last two minima and the fit tends towards the top end of the error bars for FeO 4 in the q range above 1 nm^{-1} .

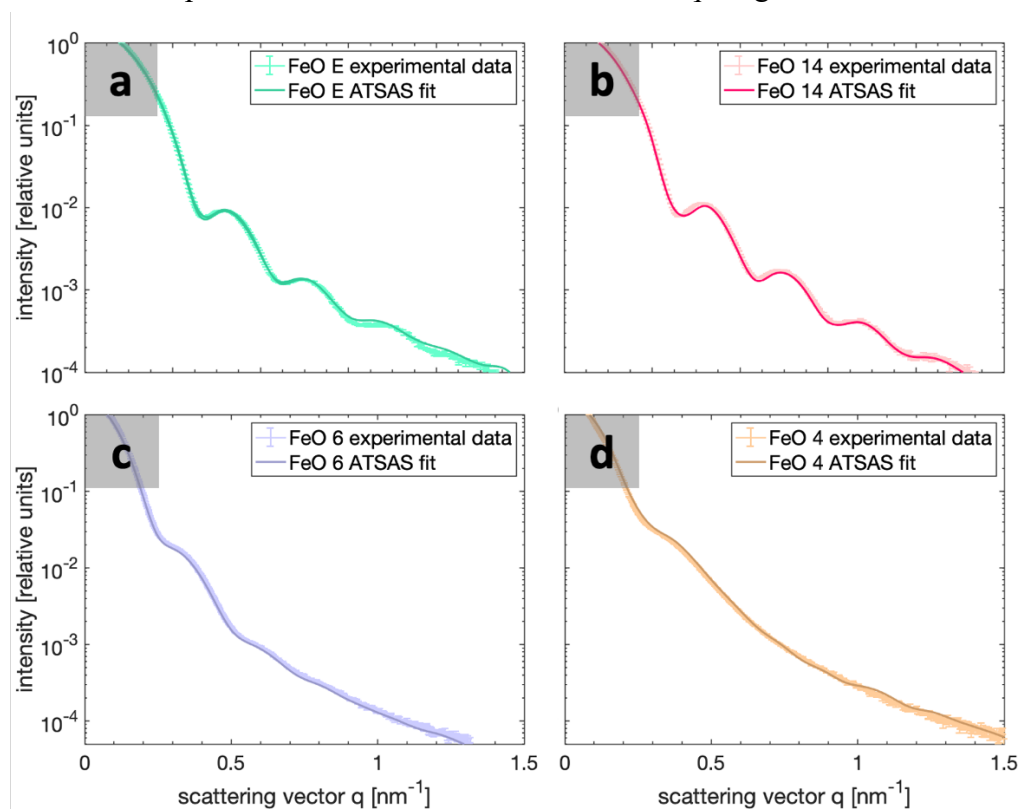


Figure 10: Fits of the models of the four samples FeO E (**a**), FeO 14 (**b**), FeO 6 (**c**) and FeO 4 (**d**) created in ATSAS with no predefined symmetry. The fits of all the models are in good accordance with the experimental data. Only FeO 4 shows some deviation in the region of the last two minima.

Figure 11a-d shows the 3D models of all four samples, created using ATSAS and displayed in Paraview. Every model is the average of 15 individual models. Two different illustrations are chosen to discuss the models in more detail. Firstly, the model is shown with all DAs on display (averaged model) **Figure 11 (left)** and secondly only DAs with a normalised occupancy greater than 0.5 are displayed (*centre*), allowing a look at a statistically more valid model. The second illustration is referred to as occupancy map. The colour scheme of the DAs represents the occupancy, red is the highest normalised occupancy (1) and blue is the lowest occupancy (0). Additionally, the fit of the computed scattering curve of the model is shown in comparison to the experimental data in **Figure 11 (right)**.

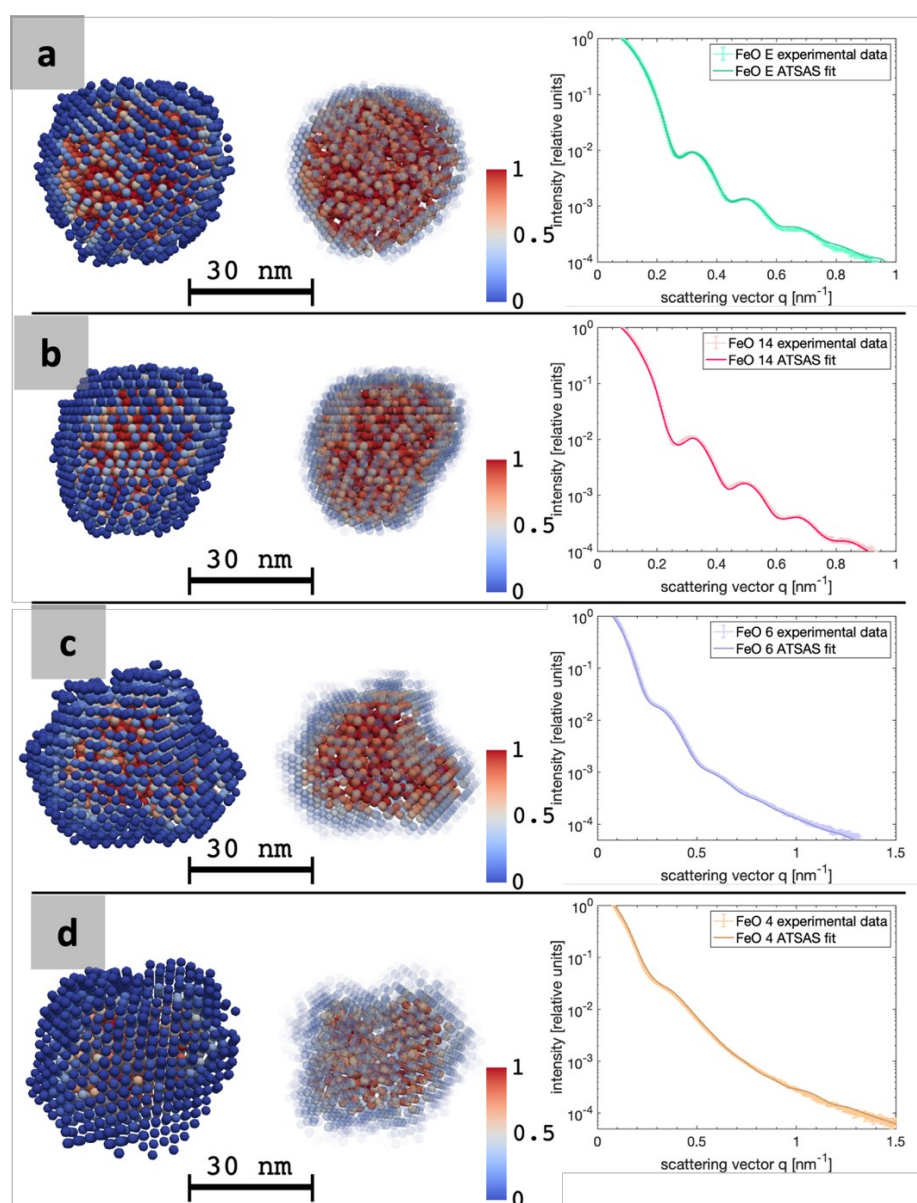


Figure 11: 3D models, created using ATSAS and no predefined symmetry, of the four samples FeO E (a), FeO 14 (b), FeO 6 (c) and FeO 4 (d) shown with all DAs on display (left), with DAs with an occupancy lower than 0.5 partly transparent (occupancy map) and a scale bar for the occupancy (centre). Furthermore, the corresponding fits are shown (right).

Generally speaking, the deviation from a cubic shape follows the trend $\text{FeO E} < \text{FeO 14} < \text{FeO 6} < \text{FeO 4}$. This trend is even more distinct considering the occupancy maps. Another general trend is that in every case the averaged model looks more cubic than the occupancy map. This effect is connected to the averaging process. As described in chapter 4.2.2, the final model is the average of 15 individual models. This is done by aligning them and remapping all of them onto an underlying grid. Because of the varying shapes of the individual models the outer perimeter tends towards a cube like shape. **Figure 12** shows all 15 individual models of sample FeO 4 (individually coloured) before the averaging process. The individual models all have many arms vectoring out in all directions, this leads to the impression of a more cube like structure, as they fill the entire space. However, the occupancy of all those DAs will only be $1/15$ once the averaging process is completed and is therefore not visible in the occupancy map. Thinking about this and looking at **Figure 12** really demonstrates the power of ATSAS. The fact that first models representing the most distinct features are created and are then, in a second step, averaged in a way that those features are emphasised is astonishing.

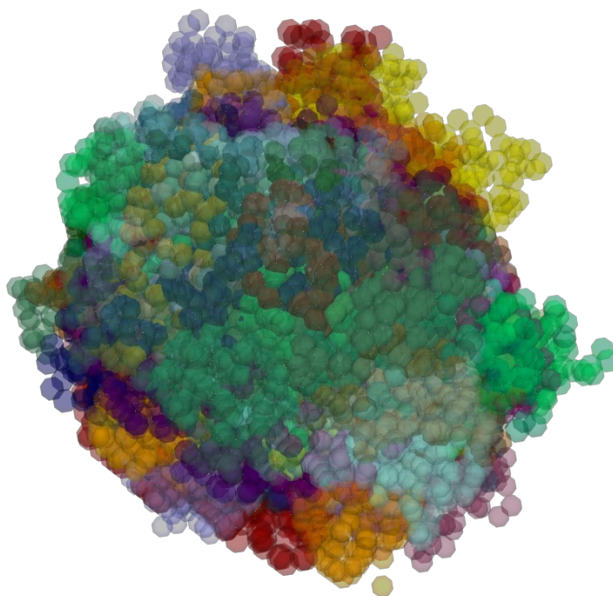


Figure 12: All 15 3D models (individually coloured) of FeO 4 before the averaging process. The little arms are the reason for the cube like overall shape of the averaged model.

Another general trend that can be spotted concerning the number of DAs with an occupancy smaller than 0.5. The number of DAs with an occupancy lower than 0.5 is smallest for FeO E and largest for FeO 4, therefore following the same trend as before $\text{FeO E} < \text{FeO 14} < \text{FeO 6} < \text{FeO 4}$. This trend can again be explained when looking at **Figure 12**. Because of the individual arms all vectoring out in different directions the individual models of FeO 4 start to overlap further inside. Looking at e.g. FeO E all individual models are of cubic shape, so the overlap is bigger if randomly oriented. Only considering the overlapped parts, however, leads to more rounded edges and vertices when comparing the occupancy map and the averaged model. This is also true for the model of FeO 14. Whilst the model's reliability and validity can be improved

by averaging the samples, a blurring effect of the details has to be taken into account. This must always be kept in mind when discussing and studying the models in the following.

Figure 13 and **Figure 14** show a three-plane projection (where **(a)** is the front view, **(b)** the side view and **(c)** the top view) and a cross section **(d)** of both, the averaged model and the occupancy map of FeO E respectively.

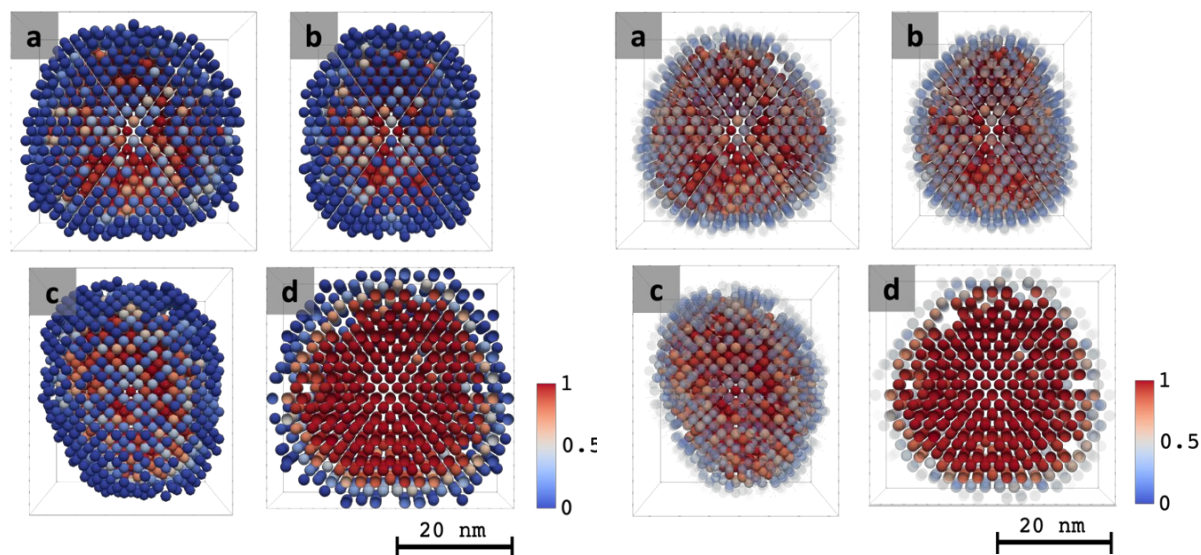


Figure 13: Averaged model of the FeO E ATSAS model in the three-plane projection, where **(a)** is the front, **(b)** the side and **(c)** the top view. Additionally, a cross section through the centre of the model is displayed **(d)**.

Figure 14: Occupancy map of the FeO E ATSAS model in the three-plane projection, where **(a)** is the front, **(b)** the side and **(c)** the top view. Additionally, a cross section through the centre of the model is displayed **(d)**.

The trend of the features of the occupancy map being blurred is continuing to show. The front view **(a)** has the squarest base area, but it turns into the least rectangular base area in the occupancy map. The side **(b)** and top view **(c)** are best described as rectangular, but not as square. Their shape, however, is better preserved when moving from the averaged model to the occupancy map. The edges and vertices are less rounded off than the front view's ones. Looking at the cross section **(d)**, one can see that there are only about one to two layers of DAs with an occupancy of less than 0.5 in the perimeter of the model. Especially the averaged model's cross section exhibits a square base with four well defined, straight sides and edges. Those four straight edges are also visible in the occupancy map, albeit not all equally long and definitely less rectangular. The fit (**Figure 11a right**) of the computed scattering curve of the model is in good agreement with the experimental data, even though the fit marginally deviates from the experimental curve starting from 0.6 nm^{-1} .

Figure 15 and **Figure 16** show the averaged model and occupancy map of FeO 14 respectively. Looking at the three projections it is again the front view (**a**), that is closest to the square base area of a cube. However, in contrast to the FeO E model, both the side (**b**) and top (**c**) view are considerably squarer than before. Yet, the cross section (**d**) is less square than before, still showing four almost equally long sides and a more or less rectangular shape though. Looking at the occupancy map, this trend no longer holds true, but rather the opposite is true. As always, the vertices and edges of the occupancy map are more rounded than those of the averaged model. Comparing the models of FeO E and FeO 14 there is a tendency towards more rounded edges and vertices in the model of FeO 14. The number of DAs with an occupancy lower 0.5 is similar in both models, accounted for by the rather cube like shape. The fit in **Figure 11b right** shows only very little deviation from the experimental data (some in the range of the first maximum), yet never exceeding the error bars.

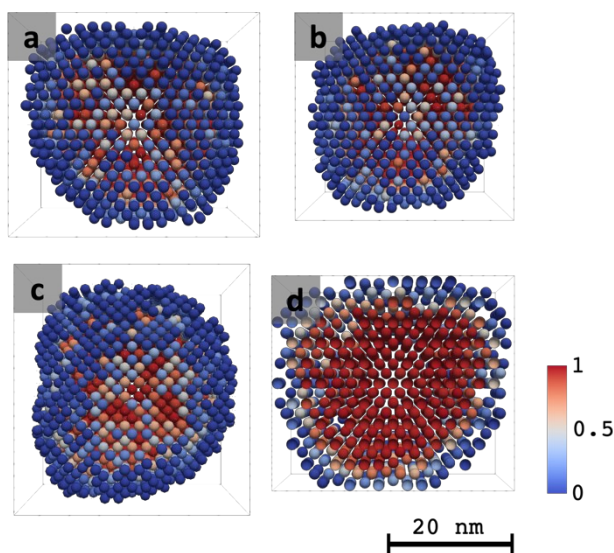


Figure 15: Averaged model of the FeO 14 ATAS model in the three-plane projection, where (**a**) is the front, (**b**) the side and (**c**) the top view. Additionally, a cross section through the centre of the model is displayed (**d**).

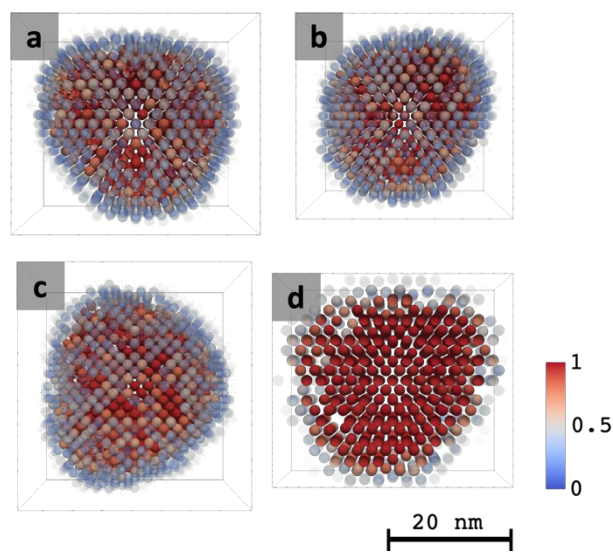


Figure 16: Occupancy map of the FeO 14 ATAS model in the three-plane projection, where (**a**) is the front, (**b**) the side and (**c**) the top view. Additionally, a cross section through the centre of the model is displayed (**d**).

Figure 17 and **Figure 18** display the averaged model and occupancy map of the model for FeO 6. Compared to the models of FeO E and FeO 14 there is a stronger divergence from the rectangular base area in all three projections (**a**, **b**, **c**) and the cross section (**d**). Whilst the front view (**a**) still shows a slightly rectangular base area, in the side (**b**) and top view (**c**) the rectangular base area gives way to a more oval shape displaying concave edges and faces. This also holds true for the cross section, where the concave faces are even more pronounced. In contrast to the models before, these distinctive details are better defined in the occupancy map than in the averaged model. The number of (layers of) DAs with an occupancy lower than 0.5 has risen to between four and five, so the overlapping core is reduced by the more arm like shape, similar to what can be seen in **Figure 12**. The fit (**Figure 11c right**) of the computed scattering curve of the model shows no deviation from the experimental data.

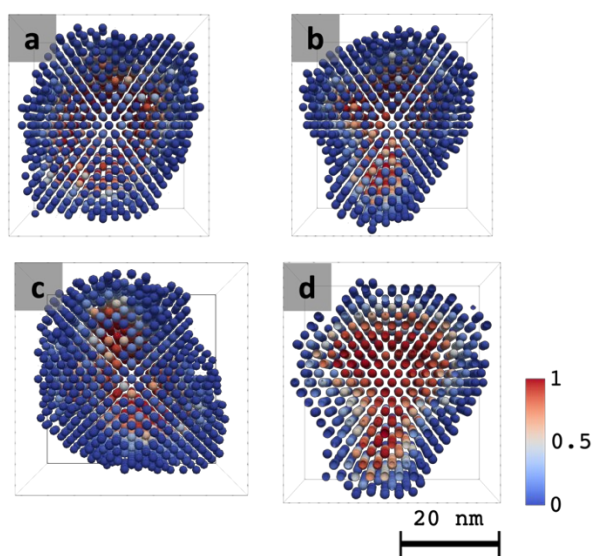


Figure 17: Averaged model of the FeO 6 ATSAS model in the three-plane projection, where (*a*) is the front, (*b*) the side and (*c*) the top view. Additionally, a cross section through the centre of the model is displayed (*d*).

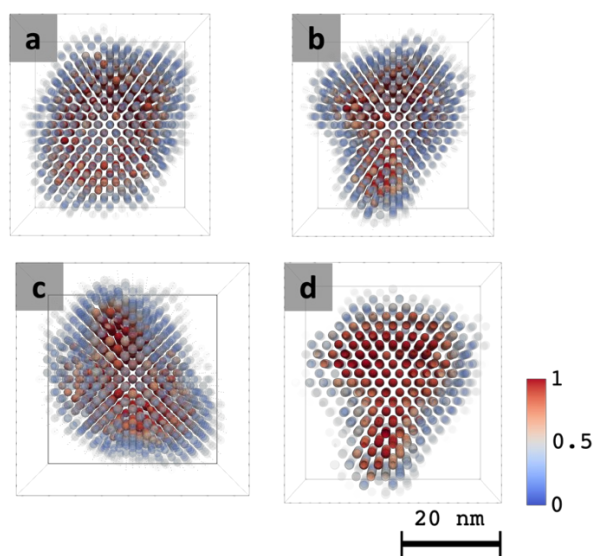


Figure 18: Occupancy map of the FeO 6 ATSAS model in the three-plane projection, where (*a*) is the front, (*b*) the side and (*c*) the top view. Additionally, a cross section through the centre of the model is displayed (*d*).

Shown in **Figure 19** and **Figure 20** are the averaged model and occupancy map for FeO 4 respectively. The divergence from a rectangular shape of the base area in all projections (**a**, **b**, **c**) and the cross section (**d**) is strongest here, compared to the other three models. Despite a star-like structure already being clearly visible in the averaged model, there still is a slightly cubic shape, caused by the DAs with an occupancy lower than 0.5. This has already been explained earlier (**Figure 12**). Comparing the averaged model of FeO 4 with those of FeO E and FeO 14 the difference regarding the rectangular base area is most notable. The number of DA layers removed because their occupancy is lower than 0.5 is between four and five. When comparing FeO 4 and FeO 6 the overall divergence from said base area is similar, however FeO 4 shows more small arms vectoring out in the averaged model. This difference is best seen when consulting the occupancy map, where the arms are clearly evident, whilst boasting an occupancy of 0.8 to 1. To quickly remind the reader, this means if ten individual models were averaged, in at least eight of the models, DAs were found in those positions. This fact gives the results of all the occupancy maps a lot of credibility and statistical validity. This is additionally emphasised by the good fit of the scattering curve of FeO 4 (**Figure 11d right**), only showing a slight trend towards the upper limit of the error bars in the range above 1 nm^{-1} .

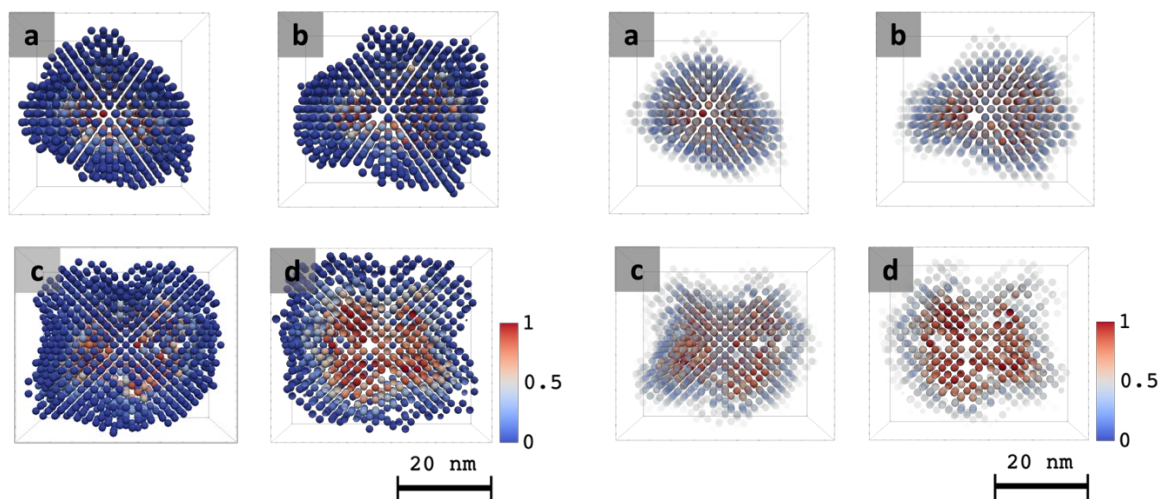


Figure 19: Averaged model of the FeO 4 ATSAS model in the three-plane projection, where (**a**) is the front, (**b**) the side and (**c**) the top view. Additionally, a cross section through the centre of the model is displayed (**d**).

Figure 20: Occupancy map of the FeO 4 ATSAS model in the three-plane projection, where (**a**) is the front, (**b**) the side and (**c**) the top view. Additionally, a cross section through the centre of the model is displayed (**d**).

5.1.2. ATSAS models with predefined symmetry

As mentioned before ATSAS supports the preselection of symmetries that will then be applied to the model. For one, this dramatically reduces the simulation time and it might improve the results as well. However, the prerequisite for this process is *a priori* information about the NCs' shape. This *a priori* information can stem from either TEM images, or in the present case the symmetry was derived from the models created without a predefined symmetry, described in

the preceding chapter. A clear tendency towards a cubic form factor can be seen in the models presented in **Figure 13** to **Figure 20**. The space group symmetry (used by ATSAS) for a cubic shape is $p432$ and is therefore used for the simulation. All the fits of the models created using the $p4$ and $p8$ symmetry bared only little resemblance to the experimental data and are therefore not included in this work.

Figure 21 shows the fits of the four models created in ATSAS using the $p432$ symmetry. For FeO E (**a**) and FeO 14 (**b**) it can be seen that the positions of the minima and maxima of the fit deviate from the experimental data. The fit of FeO 6 (**c**) tends towards the lower end of the error bars in the q range larger than 1 nm^{-1} . In the same range the fit of FeO 4 (**d**) tends towards the top end of the error bars, which is in good accordance with the fit of the model created without a predefined symmetry.

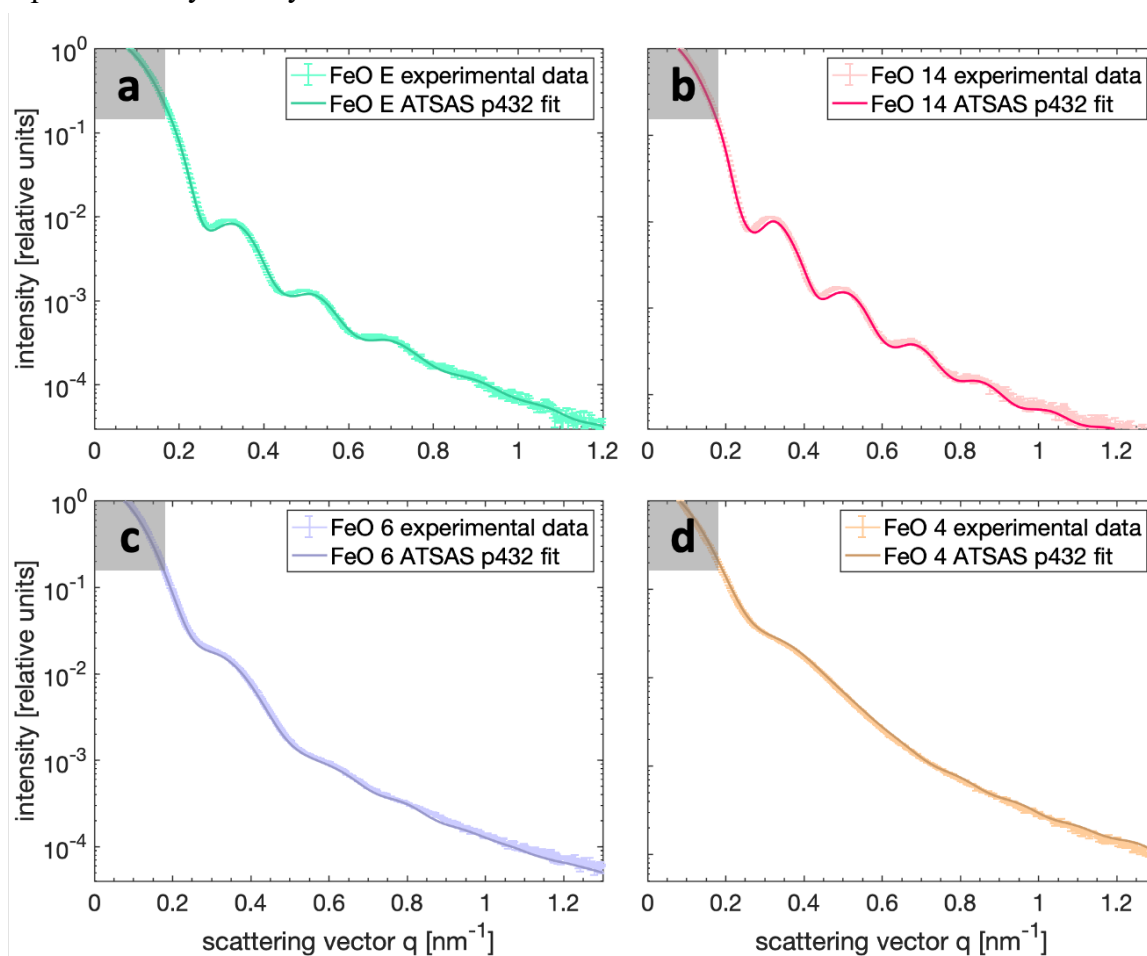


Figure 21: Fits of the models of the four samples FeO E (**a**), FeO 14 (**b**), FeO 6 (**c**) and FeO 4 (**d**) created in ATSAS with the $p432$ symmetry. For FeO E and FeO 14 there is a deviation in the position of the minima and maxima, FeO 6 and FeO 4 both tend towards the boundaries of the error bars at q values above 1 nm^{-1} .

Figure 22 shows the 3D view of the averaged model (*left*) and occupancy map (*centre*) for all four NC samples created with a predefined symmetry FeO E (**a**), FeO 14 (**b**), FeO 6 (**c**) and FeO 4 (**d**), with the corresponding fits (*right*).

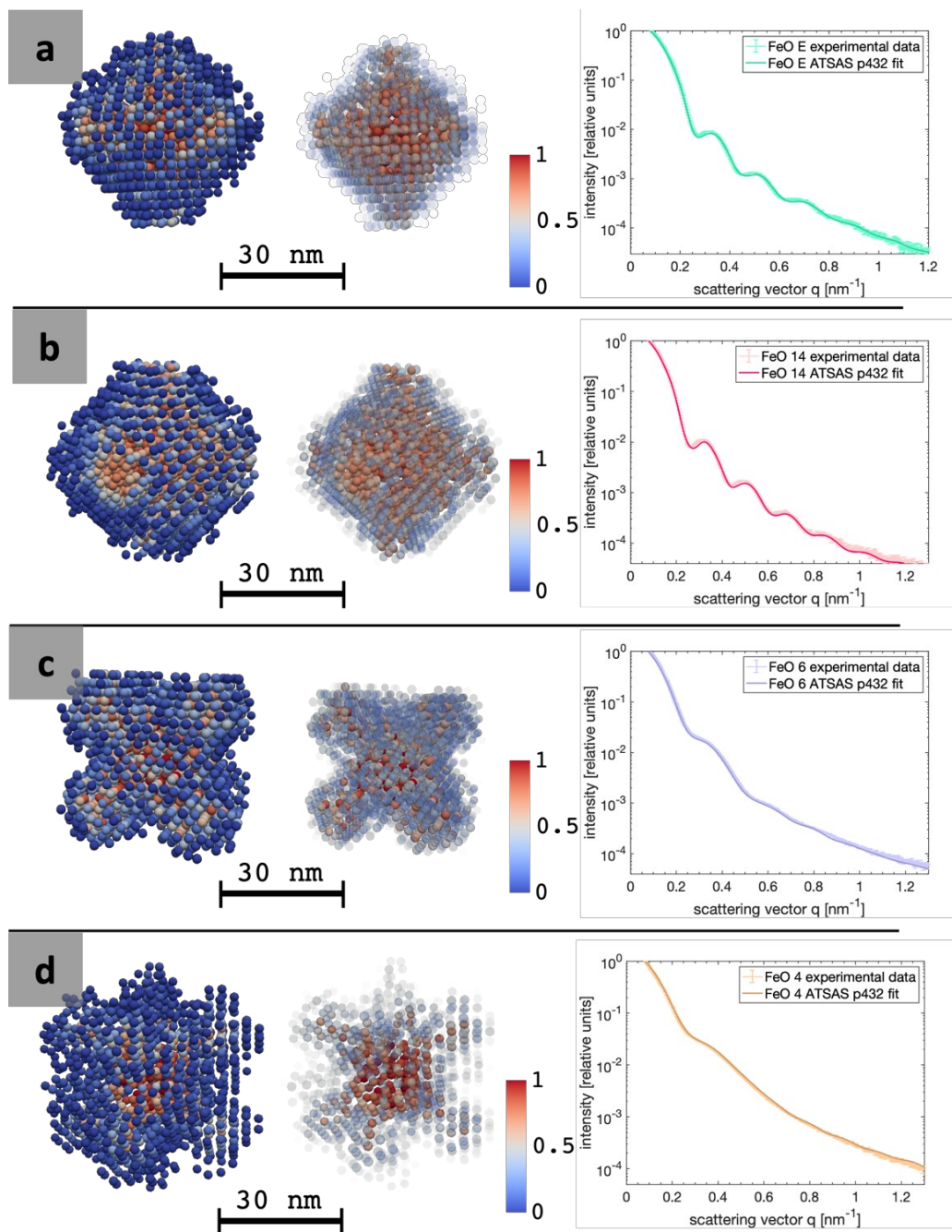


Figure 22: 3D models created using the $p432$ space group symmetry in ATSAS for FeO E (a), FeO 14 (b), FeO 6 (c) and FeO 4 (d) shown with all DAs on display (*left*), with only the DAs with an occupancy larger than 0.5 (occupancy map) on display (*centre*) and the fit of the scattering curve of the model in comparison to the experimental data (*right*).

The occupancy map of FeO E (**Figure 22a** *centre*) has a cubic shape, with a light hint of the first rudiments of very little arms growing out of the vertices of the model. The fit (*right*) shows a slight deviation from the experimental data, as it cannot fully reproduce the minima and maxima in the correct positions.

The occupancy map of FeO 14 (**Figure 22b** *centre*) looks very similar to the occupancy map of FeO E in that it also exhibits the rudiments of little arms growing out of the vertices. Apart

from the arms, the model has an almost perfectly cubic shape. However, the model of FeO 14 exhibits slightly concave faces. In analogy to the fit of FeO E, the fit of the FeO 14 model (*right*) again is slightly shifted in the region of the minima and maxima. This might be caused by the fact that the symmetry forces the edges of the model to be equally long. Because in the real system this is not the case for the majority of NCs, this leads to a difference between fit and experimental data.

Figure 22c shows the occupancy map (*centre*) for FeO 6, where a cubic shape with concave faces can clearly be seen. In contrast to the two foregoing fits, the fit for the FeO 6 model (*right*) is in extremely good accordance with the experimental data, with only a slight trend towards the lower end of the error bars in the q region above 0.9 nm^{-1} .

The FeO 4 occupancy map in **Figure 22d** (*centre*) has eight equally long arms, vectoring in all spatial directions. In the averaged model these arms are not yet visible, indicating that at least one of the individual models had the arms arranged differently. When studying the eight individual models, one can find exactly one model that has only six arms. The eight arms of the occupancy map are equally long, due to the symmetry constraints applied to the model. One can see that depending on the position a considerable amount of the DAs is lost due to the low occupancy, but this is not the case for the area surrounding the arms, where the arms exhibit an occupancy ranging from approx. 0.7 to 1, underlining the statistical significance of the model. The fit of the scattering curve of the model (*right*) is in excellent accordance with the experimental data. In analogy to the fit of the model created without symmetry (**Figure 11d** *right*) the fit tends towards the top end of the error bars in the q range larger than 1 nm^{-1} , always remaining within the error bars though.

Generally speaking, the number of DAs with an occupancy lower than 0.5 is higher than was the case for the model created without any predefined symmetry. This is clearly related to the arms present in all four models create with the $p432$ symmetry, be it with strongly differing lengths. The reasons for this effect were explained and visualised (**Figure 12**) in great detail in the preceding chapter.

5.1.3. SasHel models

As mentioned before, the SasHel models are used for comparison between a grid and a no-grid based *ab initio* shape retrieval process. As further analysis is hindered by the missing ability to calculate an occupancy, only the 3D models will be discussed.

Figure 23 shows the averaged models (*left*) of the four samples FeO E (**a**), FeO 14 (**b**), FeO 6 (**c**) and FeO 4 (**d**) and the corresponding fits of the calculated scattering curve of the model to the experimental data (*right*). This time the shapes were retrieved using the SasHel software [6]. All models presented are the average of seven individual models. The averaging was again performed using DAMAVER. The first big difference to notice, is the absence of an occupancy scale bar and the occupancy map. This is because, as mentioned before, for the SasHel models no occupancy can be calculated, due to the random nature of the DA placement.

This main difference between SasHel and ATSAS can immediately be spotted comparing, for example, two front views (for ATSAS see e.g. **Figure 13** and for SasHel e.g. **Figure 24**). Whilst in the ATSAS model a clear grid can be spotted, no such grid is visible in the SasHel model. Rather the opposite holds true and the random placement of DAs is noticeable. There are also more so called “satellite” DAs present in the SasHel model, that are not connected to the main body of the model.

Generally speaking, a clear trend towards a cube like shape can be noticed for all four samples. However, there is a deviation from this cubic shape, which is biggest for FeO 4 (**d**) and smallest for FeO E (**a**). This trend is in good agreement with the results from the ATSAS models. Roughly estimating the size, similarly sized models are retrieved by SasHel and ATSAS.

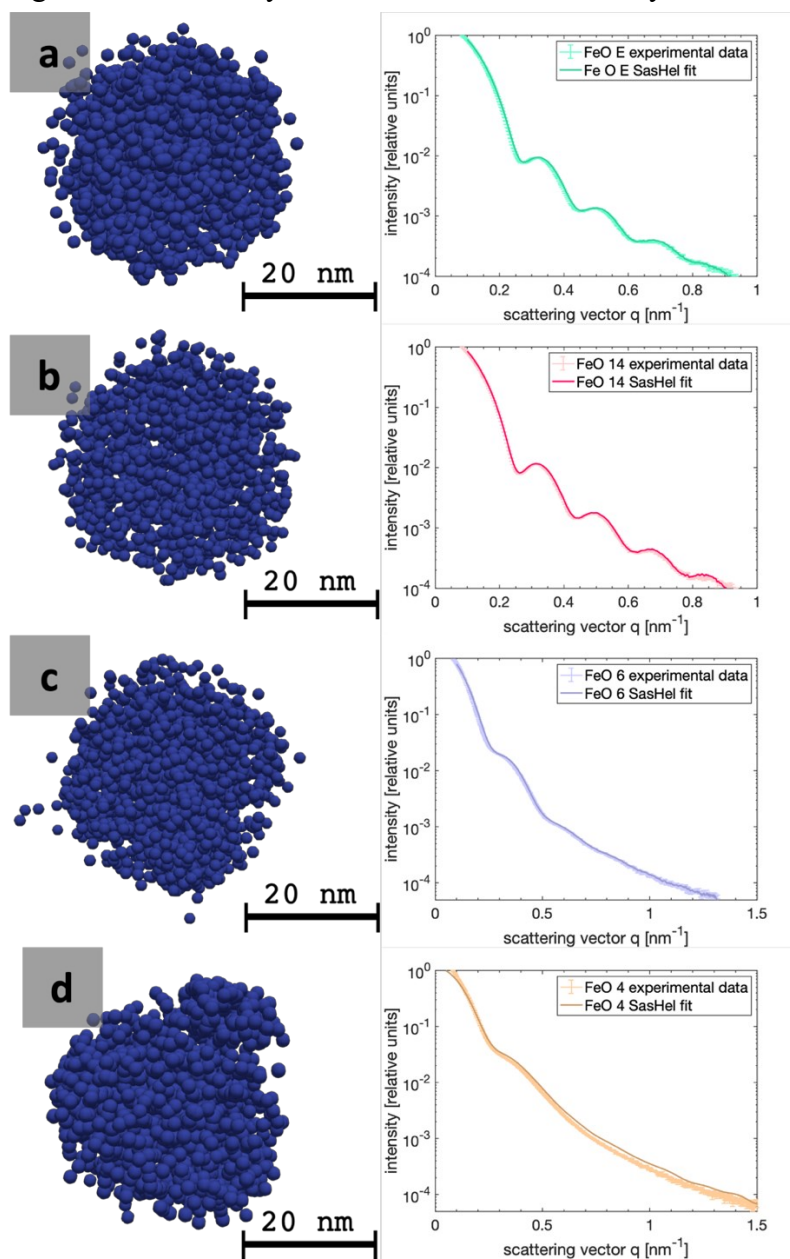


Figure 23: 3D models, created using SasHel, of the four samples FeO E (**a**), FeO 14 (**b**), FeO 6 (**c**) and FeO 4 (**d**). The averaged model (*left*) has the same occupancy all over, so no scale bar for the occupancy is needed. Additionally, the corresponding fits are shown (*right*).

Figure 24, Figure 25, Figure 26 and Figure 27 show the three-plane projection (**a, b, and c**) and a cross section (**d**) of samples FeO E, FeO 14, FeO 6 and FeO 4 respectively. This projection further supports the beforementioned trend, that the cubic shape is most pronounced for the FeO E model (**Figure 24a**) and least pronounced for the FeO 4 model (**Figure 27a**). The satellite DAs are again clearly visible in all four models. In the cross section, holes can be seen, where there basically should be a DA (fully dense cores are assumed), probably missing due to the grid free approach of the SasHel software.

The front (**a**), side (**b**) and top view (**c**) of the FeO E averaged model in **Figure 24** show a distinctly square base area, with almost perfectly equal side lengths. The edges and vertices are reproduced are extremely straight, rectangular and detailed. The same is true in the cross section (**d**). This is supported by the cube like 3D view of the model and the highly accurate fit (**Figure 23a left and right**).

Figure 25 shows the front (**a**), side (**b**) and top view (**c**) of the averaged FeO 14 model. The base area is again best described as a square, this time however, the edges are more rounded than before, this effect is most clearly visible in the cross section (**d**) of the model. The edges are straight again, and the edges are almost perfectly perpendicular to one another. The fit of the computed scattering curve is in good agreement with the experimental data (**Figure 23b right**).

The front (**a**), side (**b**) and top view (**c**) of the averaged model of FeO 6 are shown in **Figure 26** and a square base is still perceived. The edges are still very straight and perpendicular, the cross section (**d**) hints a lower density of DAs on the sides, which might be indicative of a concave face. The fit (**Figure 23c right**) is in good agreement with the experimental data.

Figure 27 shows the front (**a**), side (**b**) and top view (**c**) of the averaged FeO 4 model. There are still four sides visible in the three projections, they are, however, not equally long, nor perpendicular anymore in the front (**a**) and side view (**b**). They taper towards one end creating almost the impression of a triangular base area. In the top view (**c**) the base area is still more or less square. In the cross section (**d**) a little arm-like detail can be recognised, creating a shape that is reminiscent of a jellyfish. This jellyfish-like shape can also be seen in the 3D model in **Figure 23**. The fit shows a strong deviation from the experimental data, the slope in the q range below 0.3 nm^{-1} is off and from 0.6 nm^{-1} the fit is too high and not inside the error bars anymore. This was however the best averaged model that could be created for sample FeO 4 using SasHel. Generally speaking, the details of FeO E and FeO 14 are well defined and the difference between the two models is more distinct than it is the case for the two ATSAS models of the same samples. Regarding FeO 6 and FeO 4 this high quality of the model is not kept upright. The model of FeO 6 looks very similar to that of FeO 14 and the fit of the FeO 4 model is not acceptable anymore, rendering the result less valid.

The cube-like shape of the models retrieved using the grid free approach of SasHel additionally supports the claim made in the preceding chapter, that the $p432$ symmetry is appropriate for this system.

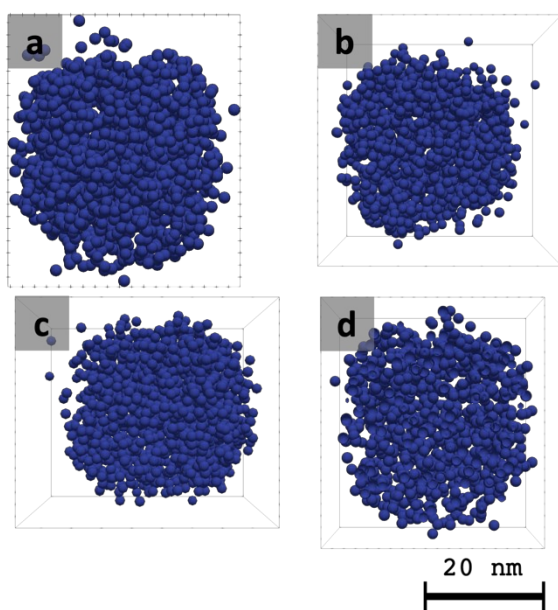


Figure 24: Averaged SasHel model of the FeO E in the three-plane projection, where (a) is the front, (b) the side and (c) the top view. Additionally, a cross section through the centre of the model is displayed (d).

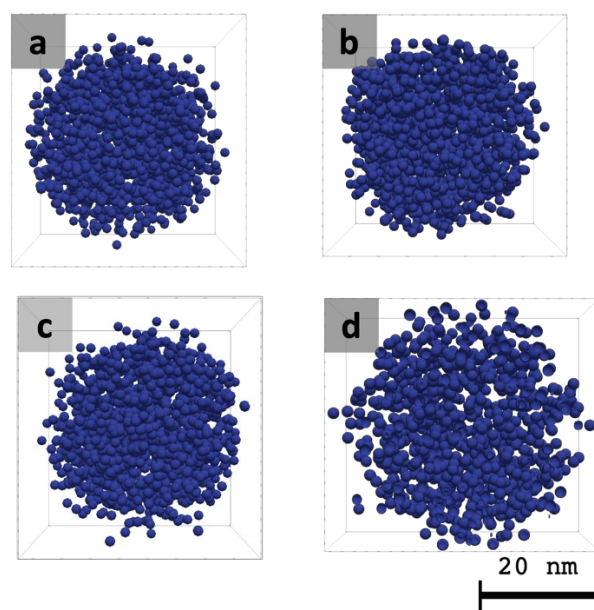


Figure 25: Averaged SasHel model of the FeO 14 in the three-plane projection, where (a) is the front, (b) the side and (c) the top view. Additionally, a cross section through the centre of the model is displayed (d).

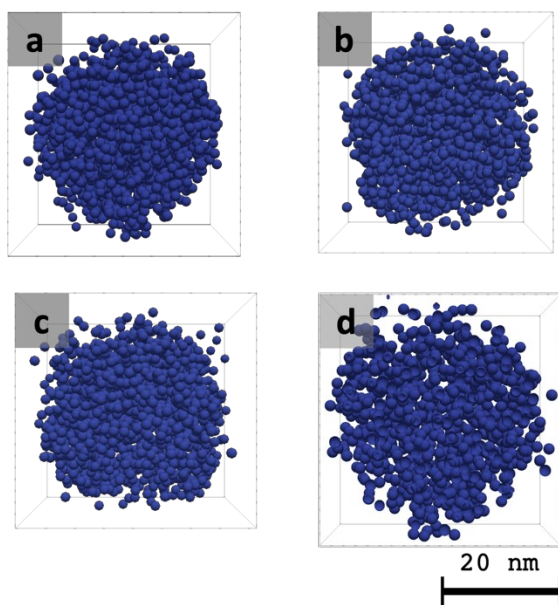


Figure 26: Averaged SasHel model of the FeO 6 in the three-plane projection, where (a) is the front, (b) the side and (c) the top view. Additionally, a cross section through the centre of the model is displayed (d).

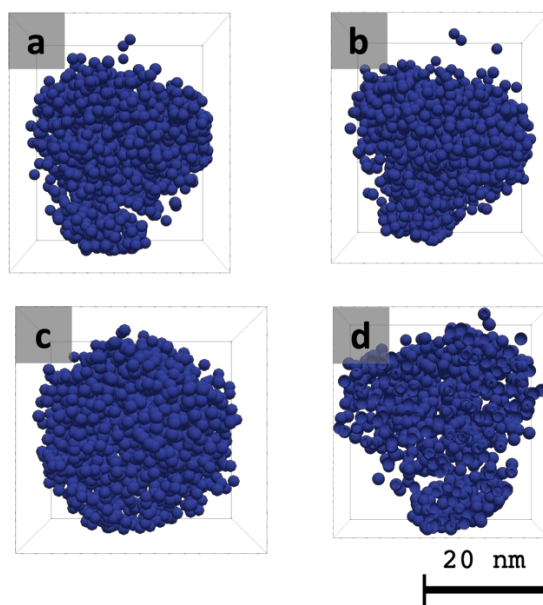


Figure 27: Averaged SasHel model of the FeO 4 in the three-plane projection, where (a) is the front, (b) the side and (c) the top view. Additionally, a cross section through the centre of the model is displayed (d).

5.2. Diameter Distribution

The diameter distribution analysed here must not be confused with the particle size distribution used to describe the range of diameters of individual particles in a powder, which is more common for classical powders and described by Jilavenkastesha *et al.* [45]. In this chapter a diameter distribution will be discussed, that focuses on the analysis of all possible dimensions of one particle, measured through the centre of gravity of the particle. This distance is denoted as diameter in the following. The mean particle shape used are the ATSAS models (with and without symmetry) of all four NC ensembles, discussed in the preceding chapter.

5.2.1. Diameter Distribution for the Models Without a Predefined Symmetry

Figure 28 shows the diameter distribution for all four samples FeO E (**a**), FeO 14 (**b**), FeO 6 (**c**) and FeO 4 (**d**), computed using a measuring cylinder with a 4 nm diameter. The diameter distribution has been normalised to the maximum frequency value of every individual distribution. The analysis was performed using one million (10^6) randomised directions.

There are two general trends observed when studying the diameter distributions. First, a broadening of the distribution is noticed. The width of the diameter distribution is defined as the FWHM and not as the difference between the minimum and maximum dimension. The width of the distribution follows the trend FeO E < FeO 14 < FeO 6 < FeO 4. Secondly, the maximum frequency value shifts towards a lower distance through the centre of gravity in the same manner. So basically, FeO E has the narrowest distribution with the peak at the highest distance through centre of gravity, and FeO 4 has the widest distribution and the peak at the lowest distance through centre of gravity.

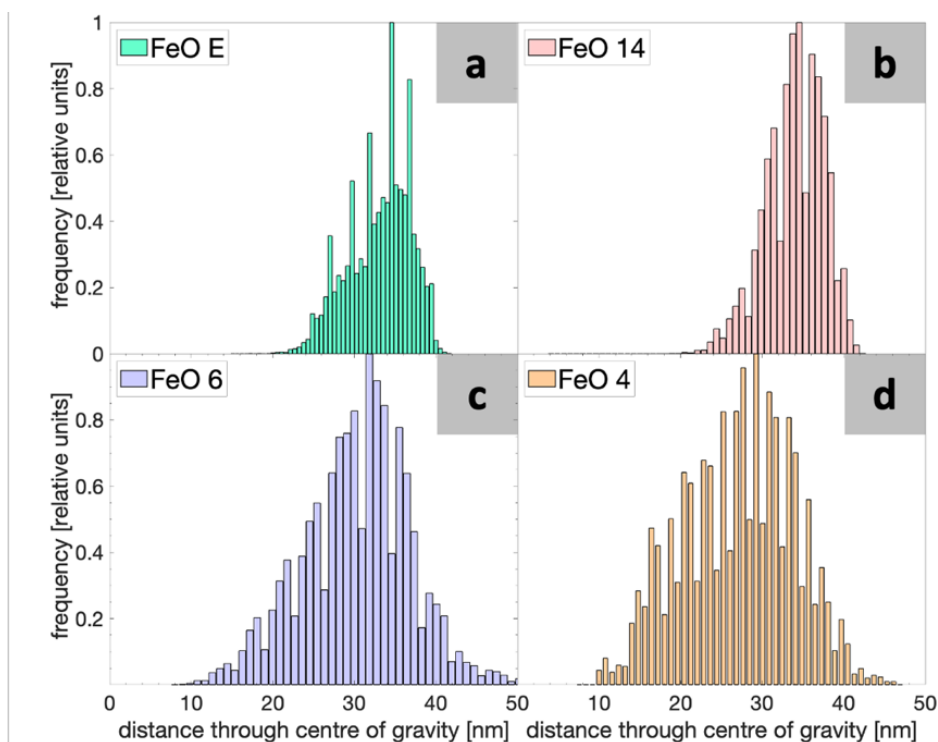


Figure 28: Diameter distribution showing all distances through the centre of gravity of one model. The diameter distribution is shown for all four samples created in ATSAS without a predefined symmetry FeO E (a), FeO 14 (b), FeO 6 (c) and FeO 4 (d). The distance through the centre of gravity was analysed with a measuring cylinder diameter of 4 nm in one million randomised directions and normalised to the maximum frequency.

The minimum, maximum dimension and the dimension with the highest frequency are listed in **Table 2**, again demonstrating that the dimension with the highest frequency is decreasing from FeO E to FeO 4. The minimum dimensions of all models must be treated with caution. Looking at the 3D models of all samples in **Figure 11** and the projections in **Figure 13** to **Figure 20** is quickly becomes obvious that not many dimension measured through the centre of gravity will be as low as 20 nm, let alone 10 nm. The explanation is not as simple as measuring, e.g. the arms of the width of the arms of the star-like FeO 4 model and holding them accountable for small minimum dimensions. This is because in the diameter distribution only the distance through the centre of gravity is considered, and the width of an arm is not measured through the centre of gravity. There are two factors contributing to the extremely low minimum dimension, a purely physical one and one that is related to the analysis method. First, the simple physical explanation is that, there are dimensions through the centre of gravity down to 15 nm in FeO 4. Secondly, there are some vacant lattice places in the model, as can be seen e.g. in **Figure 20d**. If the measuring cylinder is oriented in a way that the missing DA is within, this will lead to a reduced diameter. Paying close attention to **Figure 28a** and **b**, the frequency down to very low diameters is nonzero, due to a small number of beforementioned missing DAs inside the model.

Table 2: Comparison of the maximum, minimum and diameter with the highest frequency (equal to 1) given in nanometres. The trends derived from the diameter distribution hold true. The error is ± 0.75 nm.

Dimension	FeO E	FeO 14	FeO 6	FeO 4
Minimum Diameter [nm]	22	22	10	10
Maximum Diameter [nm]	41	42	50	47
Diameter with Highest Frequency [nm]	35	35	32	29

For a more reliable interpretation a different approach at defining the minimum and maximum dimension can be taken by defining an edge where an abrupt decrease of the frequency can be detected and neglecting the values with a low frequency that follow. Doing so will of course lead to a bigger minimum and a smaller maximum dimension, at the same time limiting the possibilities of mistakes due to the evaluation method. The diameter distribution is thereby trimmed of unreliable and unphysical values, that are the result of inevitable mistakes in the analysis. To give an example based on FeO E (**Figure 28a**) the edge for the maximum dimension is located at approx. 35 nm and for the minimum dimension at approx. 25 nm. Similar values can be defined for the model of FeO 14. For the minimum and maximum dimension of FeO 6 this means a reduction to 17 nm and 41 nm respectively. The minimum and maximum dimension of FeO 4 change to 14 nm and 40 nm respectively. Whilst this does not make a big difference for the dimensions regarding FeO E and FeO 14, it definitely changes the dimensions of FeO 6 and FeO 4 to more realistic values. **Table 3** outlines the results, together with the ratio of the maximum to minimum diameter. The ratio of maximum and minimum diameter can be used to compare the results to a perfect cube, for which it is known to be $\sqrt{3}$. The dimension with the highest frequency remains unchanged of course. To support the claim that those values can simply be neglected, and that they really stem from a mistake in the evaluation method, the diameter distribution was recalculated, this time using a measuring cylinder with a bigger radius of 6 nm. Whilst this might lead to a loss of resolution, it can help identify errors caused by the method itself. This diameter distribution is shown in **Figure 29** and the values are in almost perfect agreement with those in **Table 3**. Only the maximum value of FeO 6 deviates, the maximum value in the distribution is 45 nm and not 41 nm, as estimated before.

Table 3: Minimum and maximum diameter using the edges to trim the diameter distribution of unreliable and unphysical values. Additionally, the ratio between the maximum and minimum dimension is given. The results are in good comparison to the diameter distribution calculated using the larger measuring cylinder. The error is ± 0.75 nm.

Dimension	FeO E	FeO 14	FeO 6	FeO 4
Minimum Diameter [nm]	25	25	17	16
Maximum Diameter [nm]	39	39	41	40
Ratio of Maximum to Minimum Diameter	1.6	1.6	2.4	2.5

Increasing the diameter of the measuring cylinder not only trims the distribution of any unphysical values, but also considerably smoothens the distribution. The spikes present in **Figure 28** are almost completely eliminated, making the distribution easier to interpret.

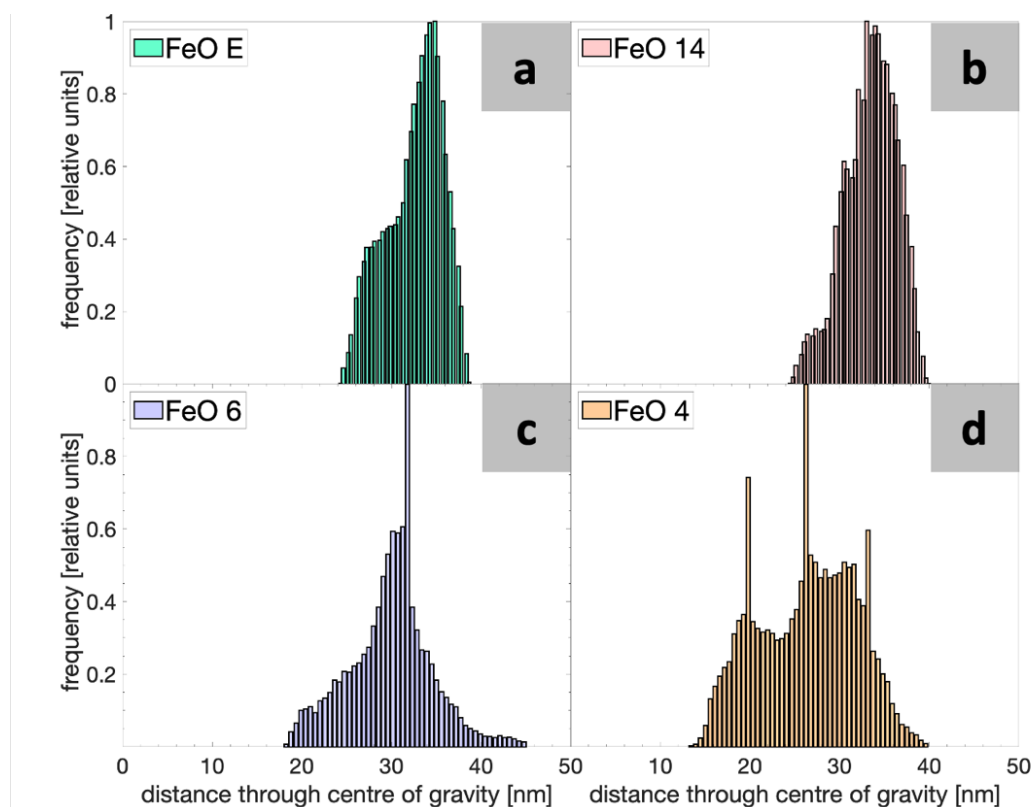


Figure 29: Diameter distribution showing all distances through the centre of gravity of one model. The diameter distribution is shown for all four samples created in ATSAS without a predefined symmetry FeO E (a), FeO 14 (b), FeO 6 (c) and FeO 4 (d). The distance trough the centre of gravity was analysed with a measuring cylinder radius of 6 nm in one hundred thousand randomised directions and the maximum frequency is normalised to 1 in the depiction.

5.2.2. Diameter Distribution for the Models With a Predefined Symmetry

The diameter distribution was also calculated for the models created using the predefined *p432* symmetry. **Figure 30** shows the diameter distribution for the models of FeO E (a), FeO 14 (b),

FeO 6 (**c**) and FeO 4 (**d**). It was created using a measuring cylinder with a radius of 4nm and measured at one hundred thousand randomised directions.

The diameter distributions of all four samples look very similar, but the diameter with the highest frequency is shifted towards lower dimensions when going from FeO E to FeO 4 and at the same time dimensions surrounding the diameter with the highest frequency become more frequent (this is most pronounced in the distribution for FeO 6).

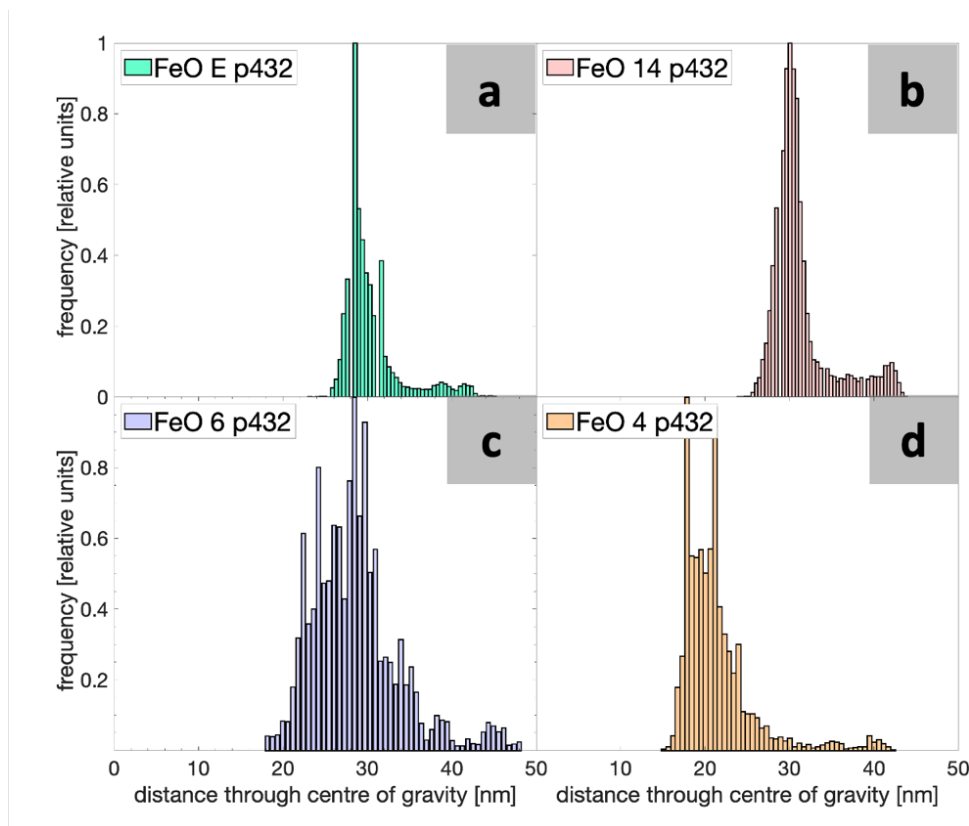


Figure 30: Diameter distribution showing all distances through the centre of gravity of one model. The diameter distribution is shown for all four samples created in ATSAS with a predefined $p432$ symmetry FeO E (**a**), FeO 14 (**b**), FeO 6 (**c**) and FeO 4 (**d**). The distance trough the centre of gravity was analysed with a measuring cylinder radius of 4 nm in one hundred thousand randomised directions and the maximum frequency is normalised to 1 in the depiction.

The maximum and minimum diameter, the diameter with the highest frequency and the ratio of maximum and minimum diameter are listed in **Table 4**. As was done for the results in **Table 3** the diameter distribution was trimmed at abrupt edges at the beginning and end of the distribution. The values are very similar to those obtained from the diameter distribution of the models created without a predefined symmetry, however the distribution itself looks substantially different. As before the largest diameters can be found in the model of FeO 6. The value for the diameter with the highest frequency of the FeO 6 model has to be treated with caution though, as there is larger range where there are numerous, almost equally frequent maxima at lower values. All four distributions in **Figure 30** show another increase in frequency towards the end of the distribution, something that was not observed before.

Table 4: Comparison of the maximum, minimum and diameter with the highest frequency for all four NCs, given in nanometres. As before, the diameter distribution is trimmed at the sharp edges. Additionally, the ratio between the maximum and minimum dimension is given. The error is ± 0.75 nm.

Dimension	FeO E	FeO 14	FeO 6	FeO 4
Minimum Diameter [nm]	26	26	18	16
Maximum Diameter [nm]	42	43	46	42
Diameter with Highest Frequency [nm]	29	30	28	18
Ratio of Maximum to Minimum Diameter	1.6	1.7	2.6	2.6

5.3. X-Ray Diffraction

XRD measurements were performed to support the findings from SAXS measurements and the subsequent shape retrieval. As this work's main focus is dedicated on the shape retrieval from SAXS data, only the two "extreme" cases FeO E and FeO 4 were investigated using XRD. The idea being, that because of the big difference between the cube- and star-like shape it is most likely to see a difference here. At least more so than if the much more similar FeO E and FeO 14 NCs were compared. Furthermore, they represent the beginning and end of the synthesis. The XRD pattern can deliver information on the chemical composition, crystallite size and possible preferential directions. If analysed carefully, this information could potentially help support the findings from SAXS.

Figure 31 shows the recorded XRD patterns for both FeO E (full green line) and FeO 4 (full orange line). The first distinction that must be mentioned, is the difference in the drying of the two NCs. Despite the approach being the same for both samples, there is an obvious difference in the way this worked out. For the FeO 4 sample, a dominant solvent peak is seen from approx. 6 nm^{-1} to 18 nm^{-1} , indicating that despite heating and a considerable amount of time exposed to air, the solvent didn't fully evaporate. The XRD pattern of the FeO E NCs paints a different picture, in the q range from 6 nm^{-1} to 18 nm^{-1} there are three extremely sharp peaks located at 7.3 , 14.1 and 20.8 nm^{-1} respectively. Because of their sharpness, a connection to the NCs can be ruled out and the peaks can rather be ascribed to toluene and oleic acid (OA) forming a crystallite structure.

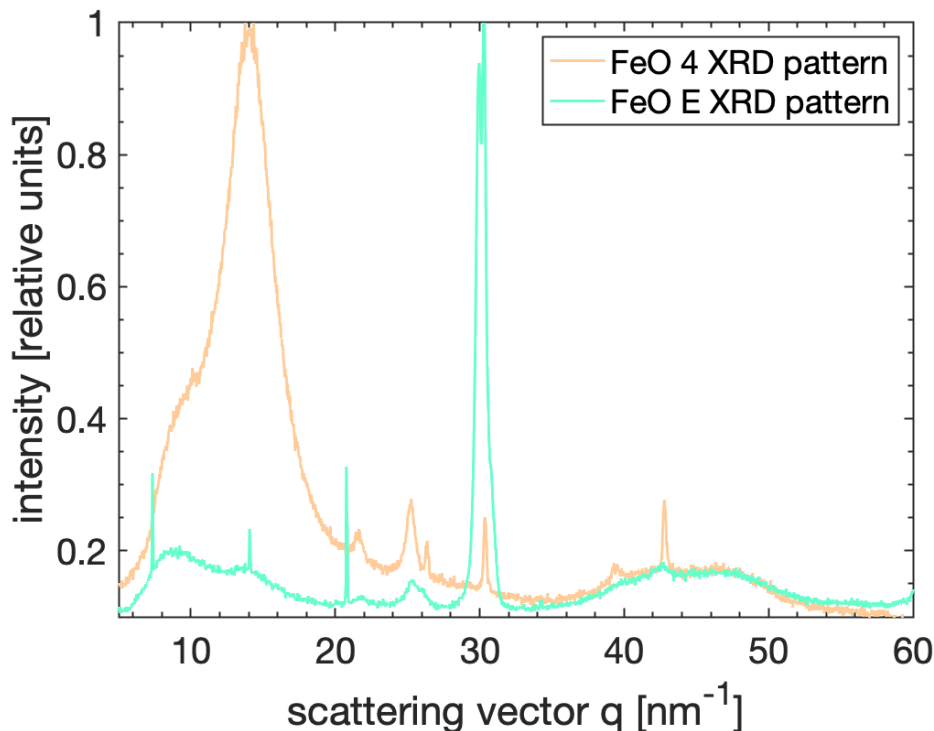


Figure 31: X-ray diffraction pattern of the samples FeO E (full green line) and FeO 4 (full orange line). Normalised intensity plotted over the scattering vector q . In the q range from 6 to 18 nm^{-1} the solvent peak of toluene in the FeO 4 XRD pattern and the crystallised solvent for the FeO E XRD pattern can be seen.

Generally speaking, both XRD patterns exhibit the same peaks, albeit with very different intensities and FWHMs, indicating that both NCs have the same chemical composition and only differ in crystallite size and preferential orientation. To obtain more information on the exact chemical composition the experimental peak position is compared to that of different standards. This process can be sped up considerably if *a priori* knowledge of the chemical composition of the sample is available. As mentioned before the NCs are synthesised from iron(II)oleate and iron(III)oleate and the finished NCs consist of FeO. It is therefore perfectly obvious to start the chemical analysis by comparing the experimental peak positions to those of standards for different oxidation states of iron. More precisely, wustite (FeO), maghemite (Fe_2O_3) and magnetite (Fe_3O_4). The result of this comparison is shown in **Figure 32**. It can be seen that because the NCs were exposed to air, the FeO is gone and the iron has further oxidised increasing the oxidation state of iron. After their exposure to air the NCs have therefore turned mainly into Fe_3O_4 and some Fe_2O_3 , as can be seen by the good agreement of standards and experimental data shown in **Figure 32**. It was shown before, that there is no difference regarding size and shape between the different oxidation states of the NCs [8].

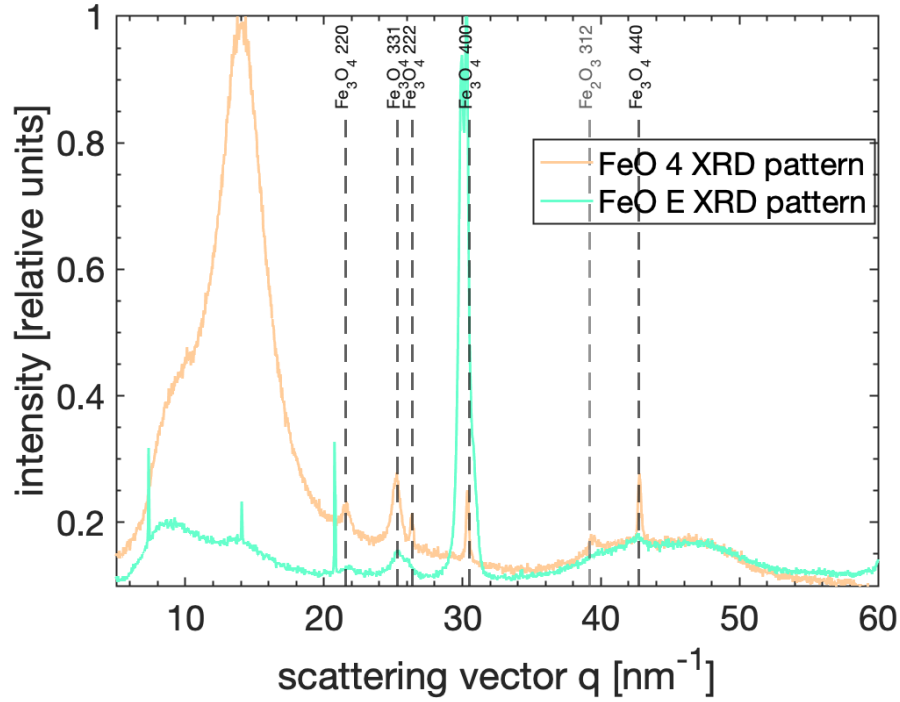


Figure 32: X-ray diffraction pattern of the samples FeO E (full green line) and FeO 4 (full orange line). Additionally, the peak positions of Fe_2O_3 (dashed light grey line) and Fe_3O_4 (dashed dark grey line) are represented with the corresponding crystallographic direction (labelled at the top of the inherent peak position). Normalised intensity plotted over the scattering vector q .

Using *Scherrer's Equation* (Equation 29) the crystallite size was analysed for all peaks of FeO E and FeO 4. The crystallite sizes with corresponding crystallographic directions are listed in **Table 5**. All peaks can be ascribed to either Fe_3O_4 or Fe_2O_3 and the crystallite size is somewhere between 6 nm and 25 nm and therefore smaller than the NCs overall size, demonstrating the feasibility of the 3D models' sizes. Furthermore, this reveals that the NCs are apparently not single crystalline. The crystallite's size span is considerably smaller for the FeO E NCs (approx. 6 to 13 nm) than it is for the FeO 4 NCs (approx. 8 to 26 nm). Furthermore, FeO 4 shows the larger crystallites with up to approx. 26 nm. Interestingly there are only three peaks ((222), (400) and (440)) that show this increase in crystallite size. This could indicate a connection between the crystallographic direction and the increase in crystallite size.

Table 5: Outline of the different peaks in the XRD patterns of FeO E and FeO 4 with their corresponding crystallographic direction, oxidation state of the iron and size of the crystallite.

Peak Position [nm^{-1}]	21.7	25.2	26.4	30.3	39.3	42.8
Crystallographic plane	(220)	(331)	(222)	(400)	(312)	(440)
Oxidation state	Fe_3O_4	Fe_3O_4	Fe_3O_4	Fe_3O_4	Fe_2O_3	Fe_3O_4
Size FeO E [nm]	9.0	6.5	12.6	7.3	-	9.2
Size FeO 4 [nm]	15.3	8.0	25.6	23.6	10.0	21.4

The peak intensities of FeO E and FeO 4 in **Figure 32** are varying strongly. Whilst there is a noticeable difference in the intensities of the FeO 4 peaks, it is nowhere near as pronounced as in the FeO E XRD pattern. For FeO E the intensity of the (400) peak, located at $\sim 30 \text{ nm}^{-1}$, is approx. 25 times higher than for the next peak ((331) located at $\sim 25 \text{ nm}^{-1}$). This big difference in the intensity of the peak clearly indicates a preferential direction in the $\langle 100 \rangle$ direction, as the normalised standard intensity for the (400) peak is only 0.2. This is no surprise, as it can be assumed that a majority of the cube like NCs is oriented on their faces.

6. Discussion

The aim of this chapter is combining all the results to a greater picture. As TEM images of the FeO E, FeO 14, FeO 6 and FeO 4 NCs exist (**Figure 6**), this real space information will be used as a comparison. As the main objective of this work is reconstructing the shape of the four NCs from the SAXS data, the main focus will be on the evaluation of the success of this undertaking. Furthermore, the shape retrieval capability of SAXS regarding differently complex shapes is assessed for both the ATSAS and SasHel results. The diameter distribution is interpreted and the characteristic dimensions are compared to the 3D model. Finally, the XRD data is incorporated in order to (a) deepen the understanding of the NC shape and (b) complement and reinforce the SAXS results.

6.1. Evaluation of the SAXS models

Evaluating the feasibility of the results of the SAXS shape retrieval is done by comparing the resulting models to TEM images (all taken from [8]), always keeping the big differences in the analysis method in mind. As understanding this difference is vital for the subsequent chapter, a quick reminder of those differences follows, despite having been discussed in great detail before:

- (a) Using TEM a maximum of approx. 100 – 500 NCs can be analysed. Using SAXS this number is considerably higher, in the present case between 10^{10} and 10^{11} . Therefore, the results from SAXS shape retrieval have a higher statistical validity.
- (b) Due to the random orientation of the NCs in the sample and the large amount of NCs contributing to the result, the shape extracted from SAXS measurements is a 3D representation of the averaged mean shape of the NCs.
- (c) TEM images are a representation of the focus plane only and contain no information on the shape perpendicular to the focus plane. Unless an electron tomography is performed, as was done by Feld *et al.* [8], it's a 2D representation of a 3D shape.

6.1.1. SAXS models without a predefined symmetry

Figure 33 shows the TEM image (*centre*), ATSAS occupancy map (*left*) and SasHel model (*right*) (both in front view) of FeO E. The size conformity of the three models is good, although the NC appear slightly larger in the TEM image than in the SAXS models. The base area of the TEM image is almost perfectly square, with slightly rounded vertices. The base area of the SasHel model is almost perfectly square too, again with similarly rounded edges, but there are some DAs not connected to the main body. Those satellite DAs are most probably the result of the grid free approach of SasHel and could indicate that the averaging process using DAMAVER is not working properly either, as loose, disconnected DAs should be removed in the averaging process. Nevertheless, the retrieved shape is in exceptionally good agreement with the TEM shape, if the disconnected DAs are neglected. Taking a closer look at the ATSAS

model, again a square-like base area can be established, this time however the divergence from a perfect square is apparent. The edges are not really rounded but rather truncated by factettes, leading to the impression of more than four edges. In the 3D model, a tapering of the cube towards one end can be observed. This could be a way of the model coping with the slight polydispersity of the ensemble, that can be seen from the TEM images in **Figure 37**.

Keeping the three differences between SAXS and TEM in mind, the result is still impressive in the way it represents the averaged shape of at least 10^{10} NCs.

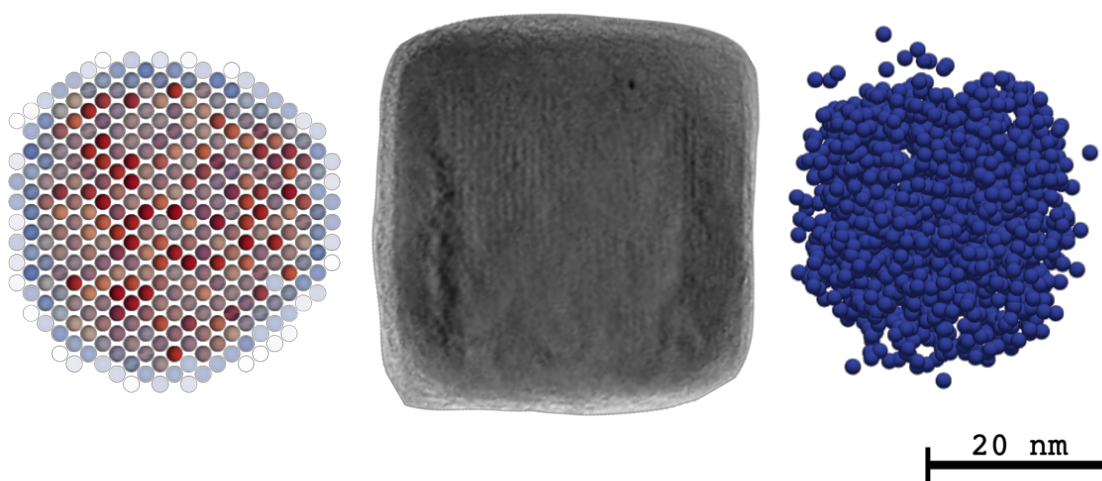


Figure 33: Comparison of the TEM image (*centre*), the ATSAS occupancy map (*left*) and SasHel model (*right*) of FeO E. Whilst the NCs appear larger in the TEM, the shape is astonishingly well reproduced by both models.

The TEM image (*centre*), ATSAS occupancy map (*left*) and SasHel model (*right*) for FeO 14 are shown in **Figure 34**. Again, a difference between the size in the TEM image and the model size is observed, where the NCs appear larger in TEM. Regarding the shape, both models have a square-like base area. Looking at the SasHel model, one can see that apart from the size the model and TEM image are almost congruent, even the increased roundness of the vertices is almost identical. In the FeO 14 SasHel model satellite DAs are present, but there are only few and close to the main body. In the ATSAS model the vertices are again truncated and not rounded, but this time the truncation is stronger than it was before, coinciding with the TEM image.

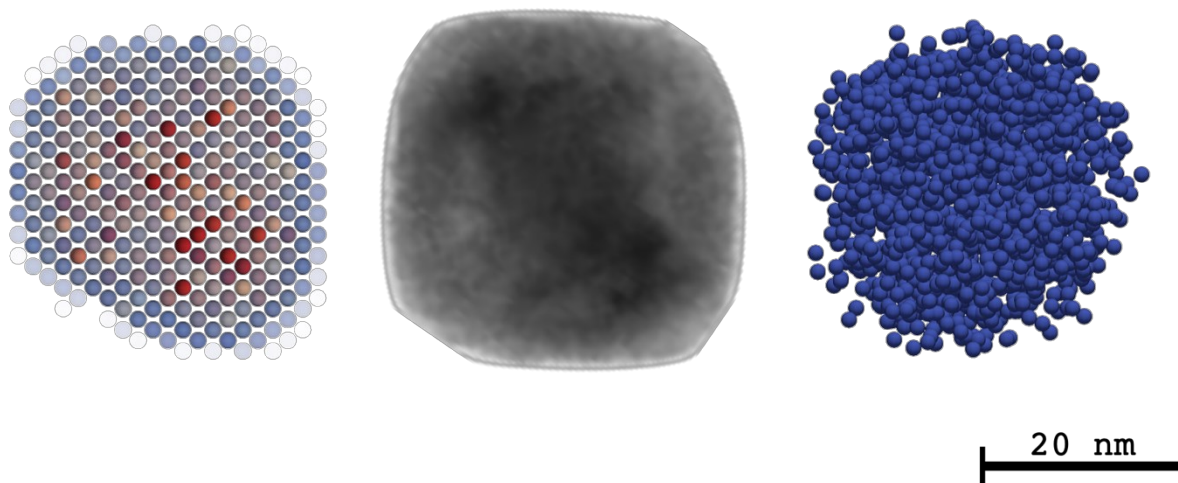


Figure 34: Comparison of the TEM image (*centre*), the ATSAS (*left*) occupancy map and SasHel (*right*) model of FeO 14. Whilst the NCs appear larger in the TEM, the shape is astonishingly well reproduced by both models.

The results of the ATSAS (*left*) and SasHel (*right*) shape retrieval for FeO 6 are shown in comparison to the corresponding TEM image (*centre*) in **Figure 35**. The trend of the NCs in the models being smaller than in the TEM image continues. Furthermore, there are two phenomena to be observed, (1) the SasHel model still has more or less the same square base area as before, albeit with a hint of a concave face on the lower right hand side and (2) the ATSAS occupancy map now has a non-rectangular base area with clear concave faces. The conformity of either model and the TEM image is considerably worse than for FeO E and FeO 14.

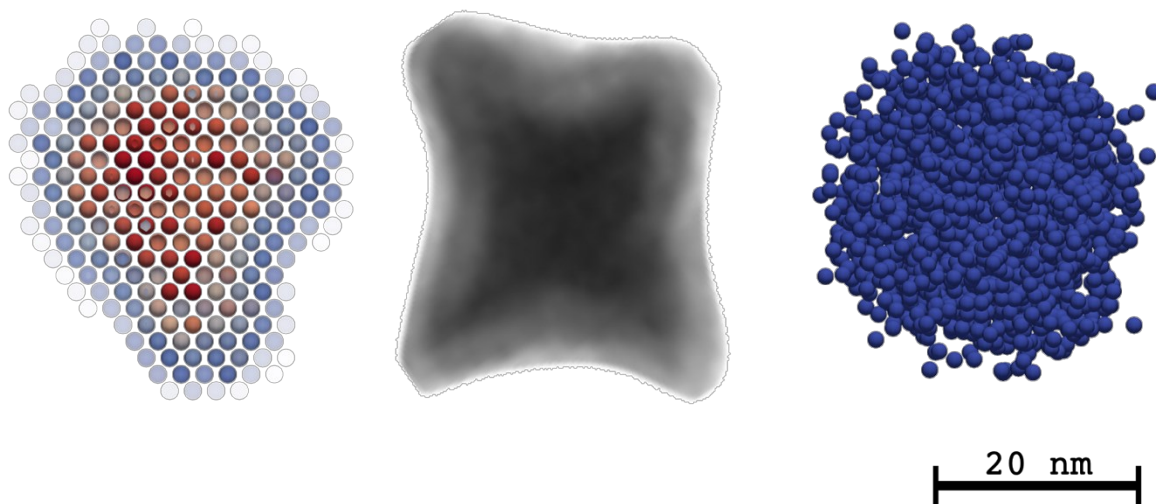


Figure 35: Comparison of the TEM image (*centre*), the ATSAS (*left*) occupancy map and SasHel (*right*) model of FeO 6. The NCs appear larger in TEM and the models only represent the characteristic feature, as the exact shape cannot be resolved for this more complex shape.

Figure 36 displays the FeO 4 ATSAS occupancy map (*left*) and SasHel model (*right*) and compares both of them to the TEM image (*centre*). As before, the NCs in the two retrieved

shapes appear smaller than in the TEM image. The ATSAS occupancy map features four more or less well-defined arms, in good accordance to the TEM image. Due to the averaging process the occupancy in large parts of these arms is rather low, but given a good understanding of the averaging process is present, this lower occupancy can be accepted. The shape resembles the TEM image reasonably well, but given the fact that this is the average of 15 individual models, each created as the mean average shape of up to 10^{11} NCs, this result is still rather impressive. The SasHel model has a triangular base area, hardly reminiscent of the star-like shape of the TEM image.

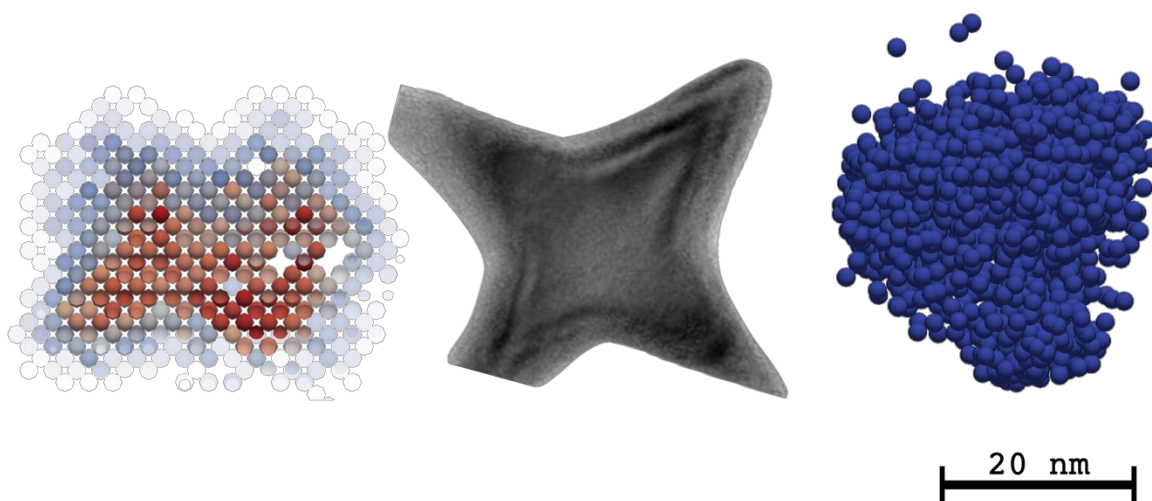


Figure 36: Comparison of the TEM image (*centre*), the ATSAS (*left*) occupancy map and SasHel (*right*) model of FeO 4. Whilst the ATSAS occupancy map is a reasonable representation of the TEM image, the SasHel model bears only little resemblance with the TEM image.

Generally speaking, there are three lessons to be learned from these results, regarding (a) the models' size, (b) general quality of shape retrieval and (c) comparison of ATSAS and SasHel.

- (a) Looking at **Figure 33** to **Figure 36** the models from either ATSAS or SasHel are always smaller than the NCs in the TEM image. This is most probably a result of the averaging process, as it removes DAs that are not in line with the most likely model. Furthermore, for the ATSAS the occupancy map is shown, where already all DAs with an occupancy lower than 0.5 have been removed. This of course leads to an additional decrease in model size. This effect is largest for FeO 6 and FeO 4, as here there are four to five DA layers lost on the outside of the model, this adds up to about 4 to 5 nm that the occupancy map loses in size. Additionally, if we consult a TEM image showing more NCs (e.g. of FeO E as shown in **Figure 37**), the polydispersity of the ensemble is observed. So maybe, the TEM images in the comparative Figures above, coincidentally were all on the larger spectrum of this distribution. This is one of the main advantages of the shape retrieval from SAXS data, a definite result that represents a statistically significant number of NCs is retrieved.

- (b) Here one should start by differentiating between the two noncomplex shapes of FeO E and FeO 14 and the two (highly) complex shapes of FeO 6 and especially FeO 4, as the results of the two groups strongly differ. The shape retrieval process for the two former NCs produced models that are in very good accordance with the TEM data. Of course, there is some deviation as the 3D model is less cubic than suggested by the TEM images, as the ATSAS model tapers towards one end. The roundness of the vertices is not reproduced perfectly, especially ATSAS truncated the vertices rather than rounding them. All things considered, there is still a clear indication that the two models stem from different NCs and that the main difference is the shape of the vertices. The latter two models paint a slightly different picture, which will be discussed based on the ATSAS models. The shape retrieval process is not capable of reconstructing a model with a fair congruence as for the simpler shapes, but rather one that contains the most characteristic features of the shape. For FeO 6 these are the concave faces, represented to a sufficient extent by the model. The characteristic features of FeO 4 are the arms, adequately represented by the model.

One must not forget that neither the FeO E, nor the FeO 4 NCs are *perfectly monodisperse* or congruent in the TEM images, as seen in **Figure 37a** and **b**. Because SAXS extracts the mean shape of more than 10^{10} NCs, it becomes obvious that this lack of congruence is the main reason for the fact that the shape is not retrieved in perfect accordance to the TEM images. The size distribution leads to a smearing of the SAXS scattering curve, which is not considered as a size distribution by the software, as they are designed for strictly monodisperse systems [5]. Given these obstacles, the results are most impressive. So far, the models have only been compared to the TEM images. However, Feld *et al.* also performed an electron tomography on a FeO 4 NC, revealing the 3D shape the NC seen in **Figure 37c**. The result is an octopod, a star with eight arms. The ATSAS model only has four arms, and they are more or less located in one plane and not vectored in all spatial directions. This can be ascribed to the fact that the NCs are completely randomly oriented in the sample, and a mean shape of this is extracted, resulting in four and not eight arms. The electron tomography results have only little statistical validity, as only one tomography is presented and the TEM image only shows four arms for every NC. Summarising, for simple shapes the models present a congruent solution to the TEM images, for more complex shapes only the characteristic features are reproduced by the shape retrieval process.

- (c) Comparing the results from ATSAS and SasHel one should look at two aspects, the resemblance of the model and the NC shape from the TEM image and the occupancy for further analysis. Starting with the latter, due to the fact that no occupancy can be calculated, further analysis of the SasHel models is hampered as no information on the statistical validity of the individual DAs is given. It is therefore imperative, that a method for averaging the SasHel models to yield the occupancy is developed. Regarding

the shape one again has to differentiate between the complex (FeO 6 and FeO 4) and non-complex (FeO E and FeO 14) structures. The SasHel models have better congruence to the simple NCs than the ATSAS models, as the ATSAS cubes slightly tapers towards one side. For the complex structures of FeO 6 and FeO 4, SasHel cannot reproduce the characteristic features to the same degree that ATSAS is able to. Summarizing, due to its capability of reproducing the characteristic features of the complex shapes even and the presence of an occupancy after averaging ATSAS is still the tool of choice when looking at retrieving the shape from SAXS data.

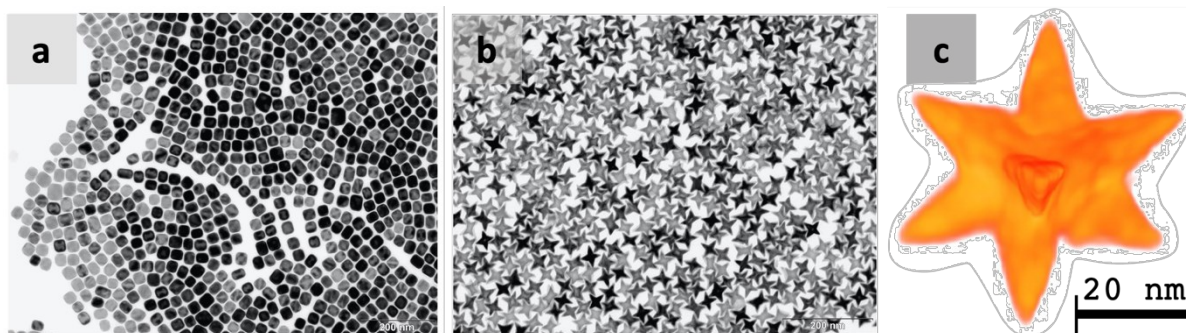


Figure 37: TEM images showing an ensemble of NCs of FeO E (*a*) and FeO 4 (*b*), revealing that the NCs exhibit a polydispersity and are not perfectly congruent. An electron tomography of a FeO 4 NC (*c*), showing the octopod-like shape with eight arms. TEM images and electron tomography taken from [8]

6.1.2. SAXS models with a predefined symmetry

It was stated before, that predefining the symmetry could lead to better results in the simulation of the NCs. In the following this statement will be proven to be true, but restrictions apply. **Figure 38** compares the cross section of the model in a 2D projection (displayed as the occupancy map) (*left*) and TEM image (*right*) of FeO E. In accordance to the model created not using a predefined symmetry the model is again smaller than the NC in the TEM image. Possible reasons for this have been discussed before. Furthermore, the model exhibits the first rudiments of small arms growing out of the vertices. It has to be pointed out that the angle between the four faces of the cube is not perfectly orthogonal and therefore the base area is nor perfectly cubic, but rather rhombohedral. Nevertheless, the model is extremely congruent with the TEM image, definitely more so than the model created without a predefined symmetry.

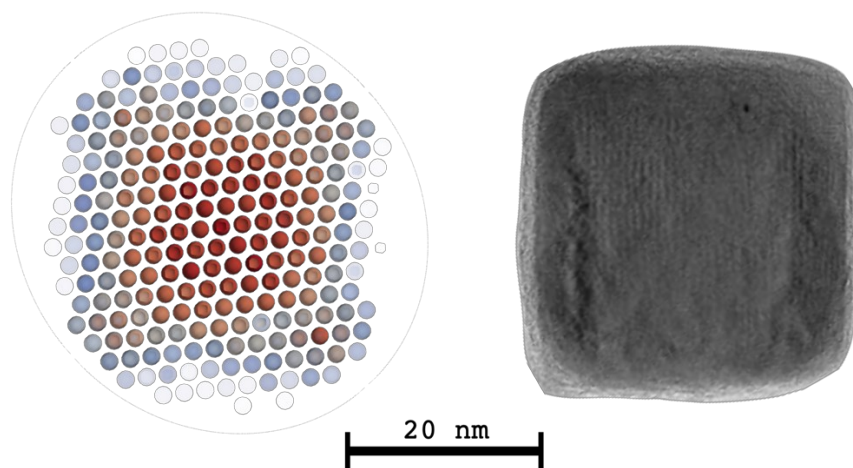


Figure 38: Comparison of a cross section of the FeO E model created using the $p432$ symmetry (*left*) and the TEM image of a FeO E NC (*right*). The occupancy map again is smaller than the NC in the TEM image and exhibits the hint of small arms in the vertices, nevertheless, it is extremely congruent with the TEM image.

Figure 39 shows the 2D occupancy map of the FeO 14 cross section (*left*) in comparison to the TEM image (*right*). The overall shape again appears rhombohedral, the vertices appear more strongly truncated than is the case for the FeO E model. This is the representation of the more rounded vertices in the TEM image. Again, rudiments of little arms growing out of the vertices can be spotted and again the model is smaller than the NC in the TEM image. Additionally, the model exhibits the first indication of concave vertices. This is not visible in the TEM image. Just as was the case before, once more the model created with the $p432$ symmetry is more congruent with the TEM image than the model created without any predefined symmetry.

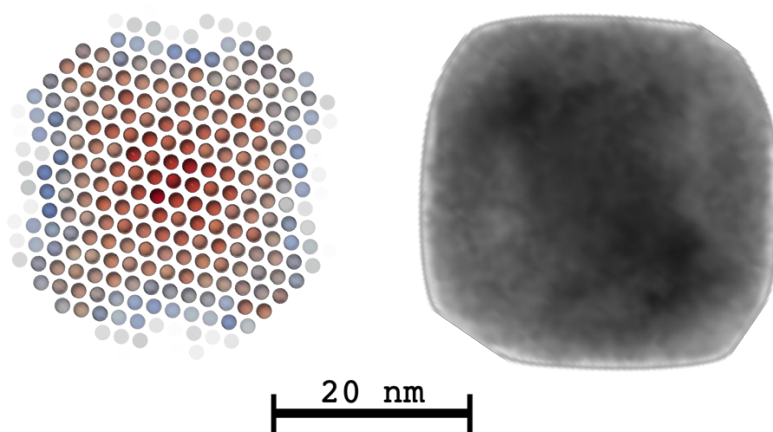


Figure 39: Comparison of a cross section of the FeO 14 model created using the $p432$ symmetry (*left*) and the TEM image of a FeO 14 NC (*right*). The occupancy map again is smaller than the NC in the TEM image and exhibits the hint of small arms in the vertices, nevertheless, it is very congruent with the TEM image.

Figure 40 shows the occupancy map of a cross section of FeO 6 (*left*) in a 2D view compared to the TEM image (*right*). The most characteristic feature of the FeO 6 NCs are the concave

faces and are congruently reproduced by the model. The model again is slightly smaller than the NC in the TEM image.

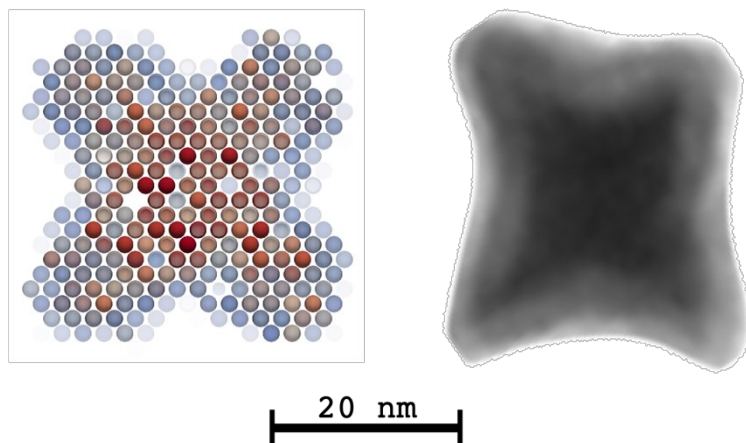


Figure 40: Comparison of a cross section of the FeO 6 model created using the $p432$ symmetry (*left*) and the TEM image of a FeO 6 NC (*right*). The occupancy map again is smaller than the NC in the TEM image. The characteristic concave faces of the NC in the TEM image are perfectly represented in the model.

Figure 41 displays the 3D occupancy map and the electron tomography image of FeO 4 side by side. The eight arms of the NCs are clearly visible in both of them and they are even almost equally long, as is the case for the body of the octopod. The entire 3D occupancy map again is a bit smaller than the real space image, this can again be ascribed to the loss of DAs due to the averaging process.

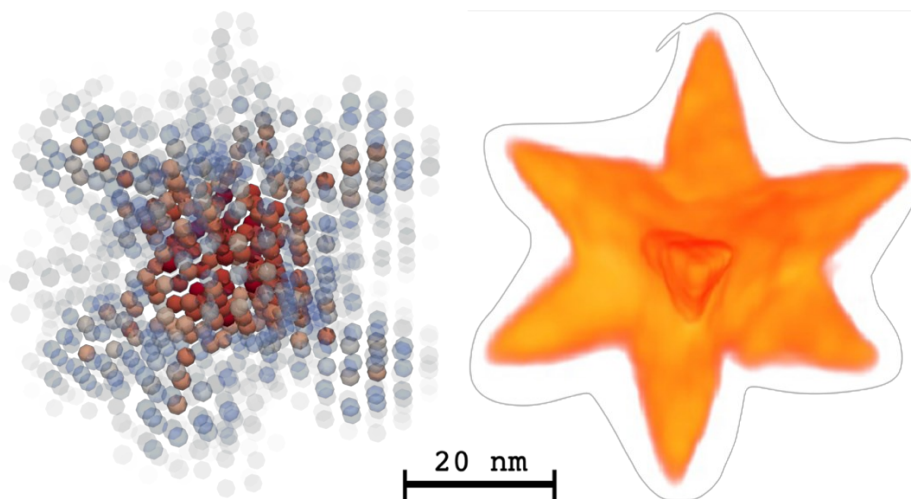


Figure 41: Comparison of the FeO 4 occupancy map created using the $p432$ symmetry (*left*) and the electron tomography image (*right*). The eight arms of the octopod seen in the tomography are also well represented by the model, additionally even displaying a similar arm length. Electron tomography taken from [8]

The results from this chapter impressively indicate that without a symmetry the shape retrieval from SAXS data is already capable of representing the characteristic features of complex NCs, but if the symmetry can be acquired either from TEM images or, as in this case, from the information of said models without any symmetry constraints, it is possible to retrieve a model that is in striking congruence to the electron tomography. Furthermore, additional information

can be extracted from the models, that is not present in the TEM images, like the first rudiments of little arms growing out of the vertices or the fact that already the FeO 14 NCs show slightly concave faces. However, extreme caution must be exercised as the predefined symmetry forces its attributes on all models and leads to a worsening of the fits of the two models of FeO E and FeO 14, as it forces all edges of the model to be equally long. This leads to corruption of the final results, as indicated by the deviation of fit and experimental data.

Table 6 conclusively summarises and compares the characteristic dimensions of the four NC samples taken from the 3D model and the TEM images. The dimension of the model was evaluated on two different ways, for one the single line diameter evaluation explained in chapter 4.3 was used and additionally Paraview’s measuring tool was used. The two are labelled as “Model” in the table. The results from the two different evaluation methods were within 1 nm. The error can be approximated with the DA radius, in this case is ± 0.75 nm. The results show an exceptional congruence for the minimum dimension, where the results from TEM are always slightly larger. This is in perfect accordance to the more qualitative size comparison above. In the case of the cube like NCs FeO E and FeO 14 the minimum dimension corresponds to the side length of the cube, for the NCs with arms FeO 6 and FeO 4 this corresponds to the central body. When looking at the results for the maximum dimension, it can be seen that the results are in good accordance for FeO 6 and FeO 4, but this is not the case for FeO E and FeO 14. The maximum dimension correlates to the arm span for FeO 6 and FeO 4 and to the body diagonal for FeO E and FeO. In the TEM images the cubes are all shown in a top view, where only the shorter face diagonal can be measured. This theory is supported by the fact that the ratio between the minimum and maximum diameter is approx. $\sqrt{2}$. When multiplying the smallest dimension with $\sqrt{3}$ the resulting dimension is again slightly larger than the largest dimension taken from the 3D model in Paraview, indicating the feasibility of the results. For FeO 6 and FeO 4 the results are considerably more congruent, as maybe sometimes the NCs are oriented in a way that the entire arm span is visible. Generally speaking, due to the polydispersity of the NCs, measuring their size from TEM images is not trivial. Nevertheless, the results again clearly demonstrate the congruence of TEM images and models, this time in a qualitative manner.

Table 6: Comparison of the characteristic dimensions of all four NCs taken from the model and the TEM images. All values given in nanometres. The error for the model is ± 0.75 nm and for the TEM results the error is ± 0.63 .

Dimension	FeO E		FeO 14		FeO 6		FeO 4	
	Model	TEM	Model	TEM	Model	TEM	Model	TEM
Dimension taken from	Model	TEM	Model	TEM	Model	TEM	Model	TEM
Maximum Diameter [nm]	42	38	42	36	43	42	40	42
Minimum Diameter [nm]	28	30	28	29	20	21	19	20

6.2. Interpreting the diameter distribution

This interpretation is best started by sorting out two potential misconceptions regarding the diameter distribution. For one, this is not the particle diameter distribution of a single NC, but rather it is representative of the entire NC ensemble. Secondly, it is not the diameter distribution of the NCs seen in the TEM images, but one of the 3D ATSAS models.

6.2.1. Interpreting the Diameter Distribution of the Models Without a Predefined Symmetry

Two trends were mentioned, for one the distribution gets wider when going from FeO E to FeO 4, whilst at the same time the most frequent dimension is decreasing in size. To fully understand this trend, one must first understand what the dimension with the highest frequency is. This diameter essentially corresponds to an inscribed sphere in the centre of the model. Looking at the TEM images in the preceding chapter, one could say that FeO E is a cube, as is FeO 14 and then gradually matter is removed to yield the cube with concave faces for FeO 6 and the star for FeO 4. The same can be applied to the ATSAS occupancy map, with the difference that the shapes are less well pronounced. Coming back to the inscribed sphere, it should be smaller for the NC where the faces are concave or the star-like shape. The inspheres are illustrated in **Figure 42**. The insphere gets smaller when going from FeO E (**a**) (insphere diameter of 35 nm) to FeO 4 (**d**) (insphere diameter of 26 nm). The insphere of FeO 14 has the same diameter as FeO E and the insphere of FeO 6 is somewhere in between with 32 nm. These values correspond perfectly to the diameters with the highest frequency from the diameter distribution in **Figure 29**.

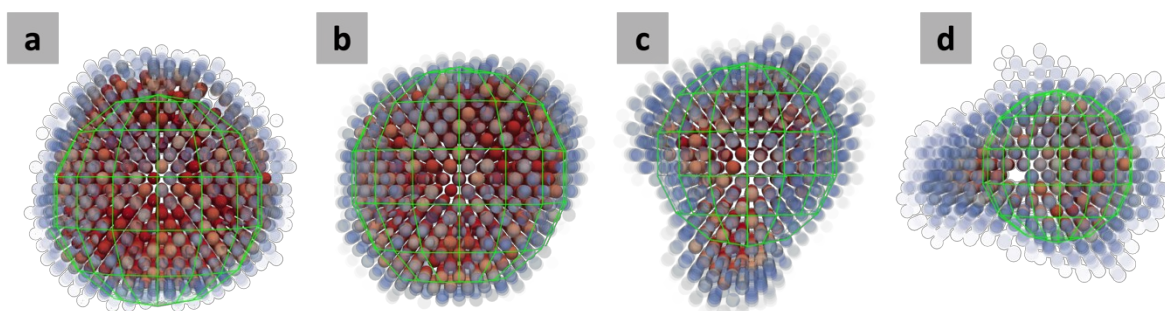


Figure 42: ATSAS occupancy maps with an inscribed sphere (green) representing the diameter with the highest frequency from the diameter distribution. These diameters are 35 nm, 35 nm, 32 nm and 26 nm for FeO E (**a**), FeO 14 (**b**), FeO 6 (**c**) and FeO 4 (**d**) respectively.

The entire diameter distributing will be explained by representatively analysing the diameter distribution of FeO 4 in more detail. **Figure 43** again shows the diameter distribution of FeO 4, but this time additionally the model is shown with cylinders (**a**, **b**, **d**, **e**) and a sphere (**c**) representing the corresponding diameter size. In case of FeO 4 the smallest diameter can be related to the smallest dimension in the core of the model (**a**). If the measuring cylinder slowly rotates by about 90°, longer distances (indicated by the longer cylinder) that at the same time are more frequent (indicated by the wider diameter of the cylinder) can be measured (**b**). As

mentioned before the diameter with the highest frequency can be ascribed to an insphere with said diameter (**c**). If the insphere is transformed back to a cylinder and located to reach the arm on the left side of the model (**d**), differently long, but equally frequent diameters are measured, explaining the plateau in the diameter distribution. The steep decline of the frequency can be explained by the fact that diameters with corresponding sizes are only possible by measuring from arm to arm. As the arms are rather thin and get even thinner towards the outermost points, the frequency drops drastically. The longest diameter is the maximum arm span of the NC (**e**).

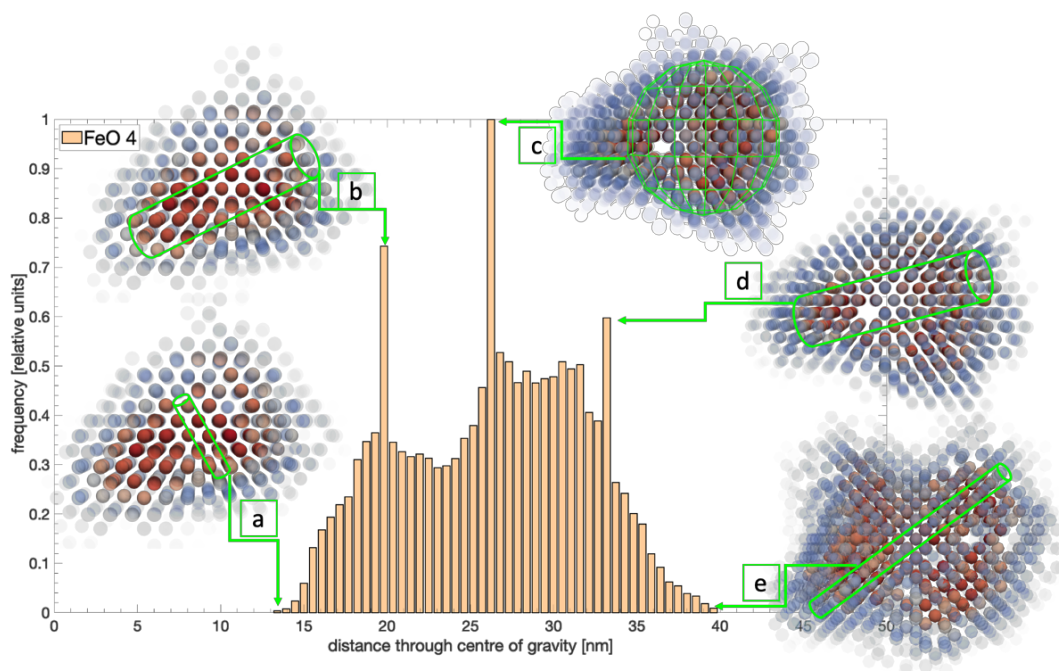


Figure 43: Diameter Distribution of FeO 4 with added models (seen from different perspectives) of FeO 4 indicating the corresponding diameter with a green cylinder or sphere. The cylinders' length and the spheres' diameter correlates to the size indicated on the distribution, *from left to right* the diameters are approx. (**a**) 15 nm, (**b**) 20 nm, (**c**) 26 nm, (**d**) 33 nm and (**e**) 40 nm. The width correlates to the frequency (not to scale).

The diameters in a cube can go from the edge length (minimum dimension) to the body diagonal (maximum dimension) and in a perfect cube the ratio would be $\sqrt{3}$. This holds true for the cube like models of FeO E and FeO 14 (as denoted in **Table 3**), where the minimum dimensions are $25 \text{ nm} \pm 0.75 \text{ nm}$ and the maximum dimension are $40 \text{ nm} \pm 0.75 \text{ nm}$ and therefore the ratio in both cases is approx. $\sqrt{3}$. This is further evidence for the cube-like shape of the two models. In the case of the star like FeO 4 NCs the difference between the maximum arm span (**Figure 43e**) and the core of the star (**Figure 43a**) is objectively larger, as represented by the diameter distribution and therefore the ratio increases to approx. 2.5. Furthermore, the difference between the most frequent diameter and the biggest diameter increases when going from the cube like FeO E NCs to the star like FeO 4 NCs, which is in line with this comment. This explains the trend of the broadening diameter distribution.

6.2.2. Interpreting the Diameter Distribution of the Models With a Predefined Symmetry

The diameter distributions of the models with a predefined symmetry (shown in **Figure 44**) follow the same trends as the distributions obtained for the models created without a symmetry and can be ascribed to the same effects. This is because the models created without a symmetry show the same characteristic features that are responsible for the characteristics of the diameter distribution. However, there are some differences that will be discussed in the following.

First, the four distributions of the four different samples look very much alike, something that cannot be said for the distributions of the models without symmetry. All distributions have a more or less congruent form, with a main peak at lower diameters and then another peak right at the end of the distribution at larger diameters. This can be explained by the fact that all four models exhibit arms, be in in very different lengths. Due to the presence of the larger dimensions in the model, that clearly correlate with those arms, the frequency increases again. It is important to note that this second peak is located at more or less the same diameter for all four samples, somewhere between 40 nm and 45 nm, indicating that the overall size of all samples remains unchanged during the synthesis. The fact that the diameter with the highest frequency decreases when going from FeO E to FeO 4, can again be explained when looking at the insphere. For the more cube like samples FeO E and FeO 14 this insphere is considerably larger than for FeO 6 and FeO 4 with their arm like shape, where the insphere can only be inscribed into the main body of the model. The dimension with the highest frequency is larger for FeO 6 than for FeO 4 because the model of FeO 6 only features concave faces and therefore the body of the model is larger than for the model of FeO 4, that has strongly pronounced arms.

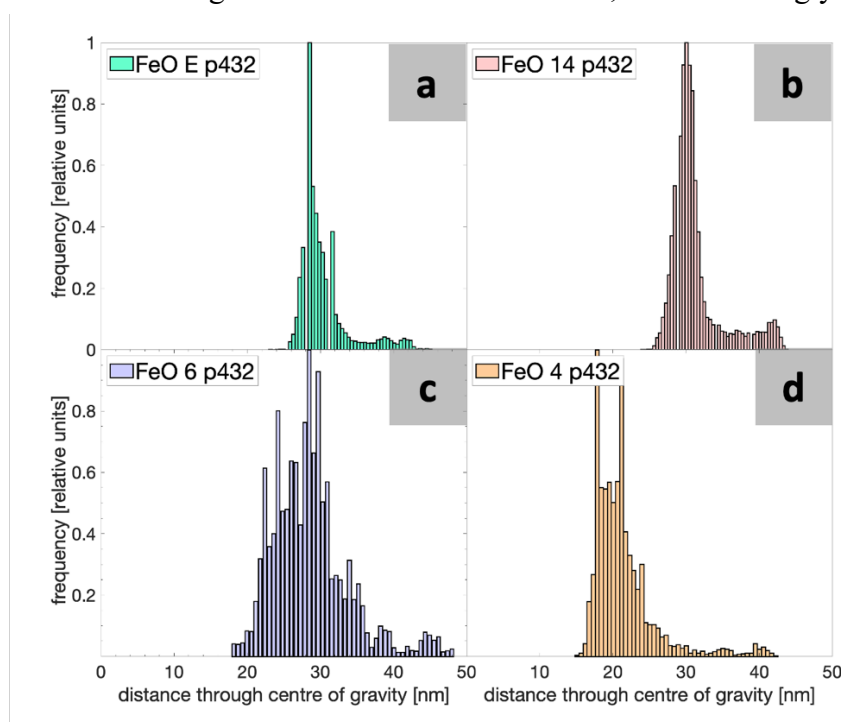


Figure 44: Diameter distribution showing all distances through the centre of gravity of one model. The diameter distribution is shown for all four samples created in ATSAS with a predefined *p432* symmetry FeO E (a), FeO 14 (b), FeO 6 (c) and FeO 4 (d).

The FWHM of the main peak of FeO E is considerably narrower than the FWHM of the main peak in the distribution of FeO 14. A schematic explanation for this is depicted in **Figure 45**. The idealised shapes of the two NCs are represented by the grey area (FeO E) and the yellow area (FeO 14). In reality the corners of the two areas would overlap, as the diameters of the two NCs are almost equal according to the diameter distribution and can also be seen by plotting the 3D models around the same centre of gravity, but in **Figure 45** they are depicted in a way that the two inspheres would be equally large to aid the explanation. The insphere in both cases has a diameter equal to the dimension indicated by the violet section of measurement (**a**) and correlates to the diameter with the highest frequency in the diameter distribution. If the section of measurement is tilted by a degree φ , then there is a considerable difference Δ in the distances measured for FeO 14 (**b**) and FeO E (**c**). Whilst for FeO E the distance measured increases only by one over the cosine of the angle φ , for FeO 14 there is an additional distance that is caused by the curvature of the face. Therefore, a little deviation from the diameter of the insphere causes a bigger difference in the diameter and with that a broader distribution. As the distribution is plotted as a histogram, a certain range of diameters is represented by one bar and because a slight deviation from the insphere causes only a small deviation a considerably larger number of diameters is represented by the most frequent bar in the distribution of FeO E leading to a very sharp and narrow peak.

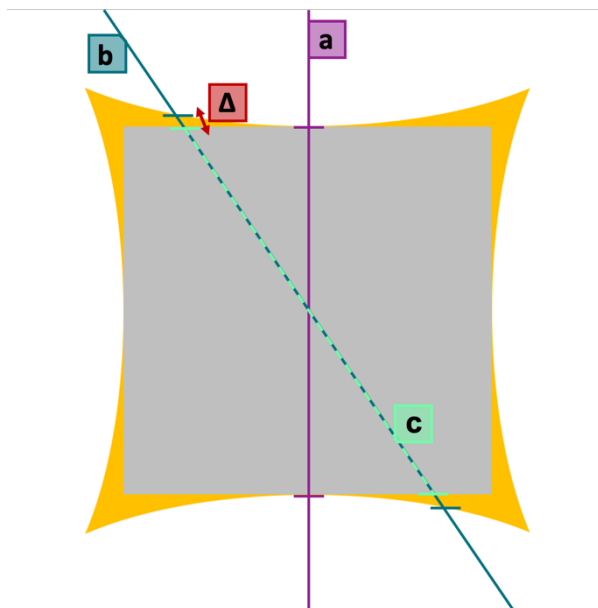


Figure 45: Schematic explanation for the narrower FWHM of the main peak in the diameter distribution of FeO 14 compared with the main peak in the distribution of FeO E (both for the models created using the $p432$ symmetry). The shape of FeO E is represented by the grey area and the shape of FeO 14 by the yellow area behind it.

6.3. XRD Data and crystal growth during synthesis

To quickly recap, the chemical composition, preferential orientation and crystallite size with corresponding crystallographic directions can be extracted from the XRD data of FeO 4 and FeO E.

The NCs' oxidation state clearly changes when exposed to air. When in solution the NCs composition is mainly wustite (FeO). The XRD data clearly indicates that after their exposure to air during the drying process and the measurement, the oxidation state of the iron changes to mostly magnetite (Fe₃O₄). It was shown before that this has no effect on the size or shape of the NCs [8].

The preferential orientation, mainly observed in the XRD data of FeO E, indicates that the dried NCs are no longer oriented randomly, but rather rearrange. From **Table 5** one can see that this preferential orientation is (400) or more generally speaking $\langle 100 \rangle$. If we consider a cubic crystal structure, this corresponds to the top plane of the cube, indicating that the cube like FeO E NCs reorient to come to rest on the cubes' base area when dried. This makes perfect sense, as it is extremely unlikely that a dried cube comes to lie on one of its edges or vertices. The crystallites in FeO 4 are almost equally long in the crystallographic directions of $\langle 100 \rangle$, $\langle 110 \rangle$ and $\langle 111 \rangle$, albeit the crystallites are slightly larger in $\langle 111 \rangle$, indicating that in the beginning stages of the synthesis the crystals grow at almost the same growth rate in all main crystallographic directions. But in the later stages of the synthesis, the growth of the NCs is mainly in $\langle 111 \rangle$ to fill the space between the arms and form the cubic shape. From the results of the diameter distribution and the models it is clear to see that the maximum dimension remains unchanged during the synthesis when going from FeO 4 to FeO E. This is further proof for the theory that once the arms of FeO 4 are formed, the only change regards the faces where slowly the empty space is filled until a cube is formed. In contrast to the TEM images, the results from the shape retrieval indicate that also the FeO E NCs exhibit little arms and that the concave faces are still visible in the NCs of FeO 14. Generally speaking, the crystallite sizes of FeO E are smaller than those of FeO 4, despite having the longer reaction time. This could indicate, that the reformation from the star like shape of FeO 4 to the cubic shape of FeO E leads to the integration of stacking faults into the system. However, this difference in crystallite size could also be caused by the oxidation process and only by performing the XRD measurement to the exclusion of oxygen could this theory be reinforced further.

7. Conclusion

In this work the shapes of four different superparamagnetic iron oxide nanocrystals were retrieved from SAXS scattering curves using the *ab initio* bead modelling software DAMMIN, DAMMIF (both referred to as ATSAS) and SasHel. The shapes of the four NCs differ strongly and exhibit details of utmost varying complexity. The shapes of the NCs range from a simple cubic to a complex star like shape with eight arms vectoring in all spatial directions. Due to its *ab initio* approach no *a priori* knowledge of the shape is needed for the shape retrieval process, as any shape can be reconstructed from an assembly of beads.

The main objective of this work is the reconstruction of the NCs' shape whilst at the same time highlighting the limits of this analysis method. Furthermore, two different approaches of bead modelling were compared, the grid free approach of SasHel and the approach of ATSAS, with an underlying FCC grid.

It was shown that without any *a priori* information on the shape, it is possible to reconstruct the simple shapes of FeO E and FeO 14 in good congruence with real space information on the shape (from TEM images), while for the complex shapes (FeO 6 and FeO 4) it is only possible to reconstruct models exhibiting the NCs' characteristic features. By calculating and interpreting the distribution of all distances through the centre of gravity of the model (denoted as diameter distribution in this work) further information on the NCs shape can be extracted.

In a next step one can either use *a priori* information from TEM images to find the symmetry of the system or take this information for the models created without a predefined symmetry. Due to the cubic shape of the models and the NCs in the TEM images, the cubic $p432$ symmetry was chosen and predefined for the next simulation of the models (only possible in ATSAS). Using a predefined symmetry improved the results of the cubic FeO E and FeO 14 models, as now they were even more congruent with the TEM images. The more remarkable difference concerns the two complex shapes of FeO 6 and FeO 4. By predefining the symmetry, it was possible to not only produce models exhibiting the characteristic features, but rather it was possible to create models with astonishing congruence to the TEM images. However, using a predefined gives rise to risks, as it forces the symmetry on the system and extreme caution must be exercised.

Regarding the comparison of SasHel and ATSAS it was found that despite the very good results retrieved from SasHel for the more cubic shapes of FeO E and FeO 14, the characteristic features of FeO 6 were only poorly reproduced and for FeO 4 it was not possible to extract information on the shape as no solution with a good fit could be found. Furthermore, the grid free approach of SasHel prevents the calculation of an occupancy. The occupancy is an important information on the statistical validity of a model and without it no further analysis was possible. To improve the usability of SasHel it is imperative that a way is found to average the models to yield the occupancy of the averaged model.

Figure 46 gives a conclusive summary of all the models created for the four NCs FeO E (**a**), FeO 14 (**b**), FeO 6 (**c**) and FeO 4 (**d**), where *from left to right* the SasHel model, ATSAS model with no predefined symmetry, ATSAS model with predefined $p432$ symmetry and TEM image are depicted. The excellent congruence of the model created using the $p432$ symmetry with the TEM image can be seen and generally speaking, the congruence improves when going from left to right.

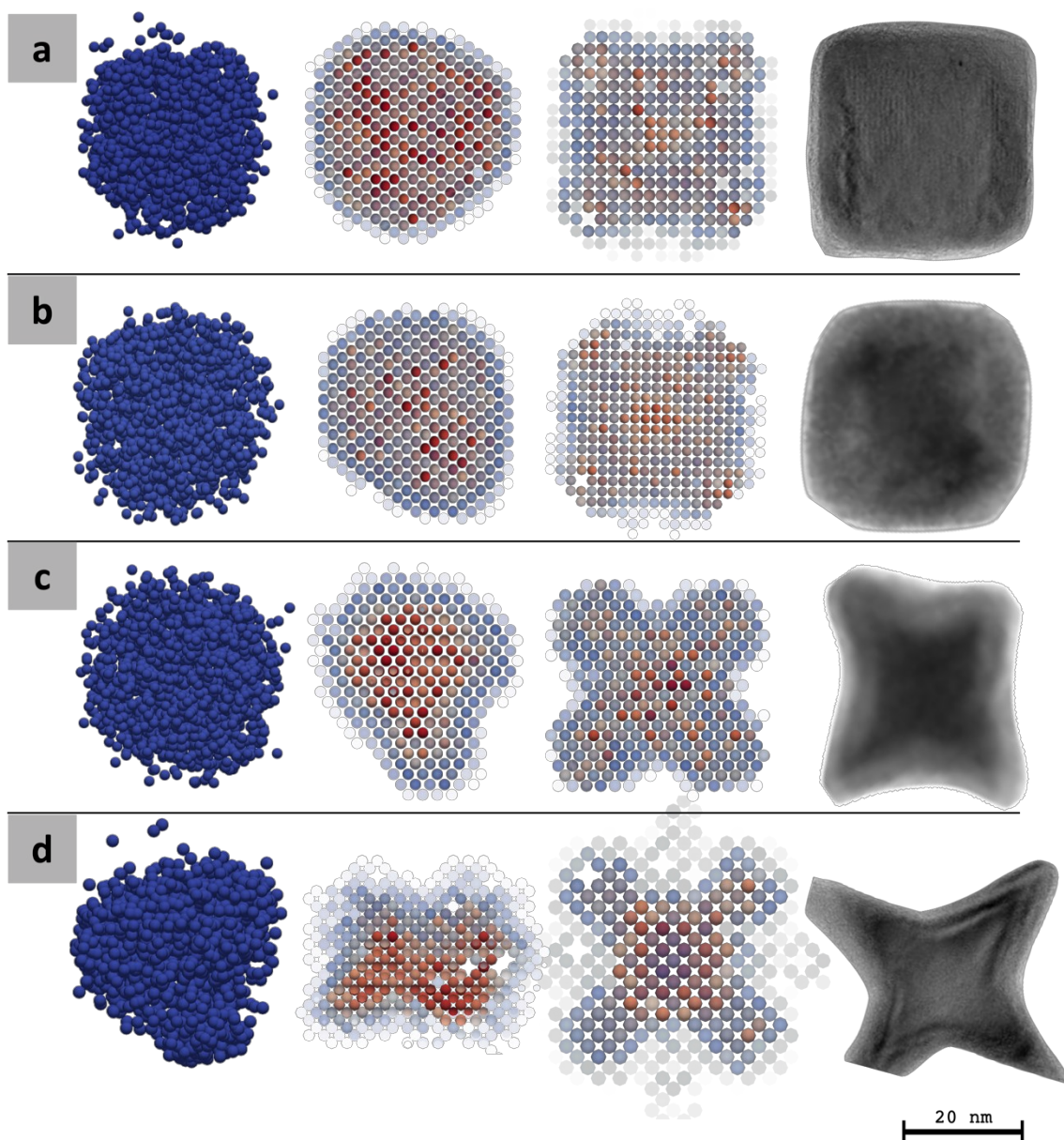


Figure 46: Summary of the different models (shown in a 2D projection) created for all four NCs FeO E (**a**), FeO 14 (**b**), FeO 6 (**c**) and FeO 4 (**d**) in comparison to the corresponding TEM image. From *left to right* there is the SasHel mode, ATSAS model without symmetry, ATSAS model with $p432$ symmetry and the TEM image. Generally speaking, the congruence of the models improves when going from left to right. This conclusive summary shows that shape retrieval from SAXS data is a powerful tool, not only for monodisperse molecular systems, but also for inorganic NCs exhibiting a limited polydispersity.

The results are even more astonishing when considering that the mean 3D shape of at least 10^{10} not perfectly monodisperse and congruent NCs was reproduced. Comparing the results of the SAXS shape retrieval with the results of a TEM analysis, especially the added statistical validity of the data has to be stressed.

Additionally, it was shown using XRD, that in the beginning of the synthesis the crystallite growth is similar in the three main crystallographic directions $\langle 100 \rangle$, $\langle 110 \rangle$ and $\langle 111 \rangle$. In later stages of the synthesis the main growth direction is $\langle 111 \rangle$ to fill space and subsequently yield the cubic NCs, whilst incorporating a considerable amount of stacking faults. These findings are further supported by the diameter distribution.

To summarise, the applicability of shape retrieval from SAXS data for inorganic NCs systems has been proven formidably. Despite the fact that the software used is not designed for systems of polydisperse, slightly incongruent NCs the shape retrieval has been demonstrated to be a powerful tool and a definite alternative to TEM when studying the morphology of colloidal nanocrystals.

References

- [1] M. Faraday, “X. The Bakerian Lecture. —Experimental relations of gold (and other metals) to light,” *Philos. Trans. R. Soc. London*, vol. 147, pp. 145–181, 1857, doi: 10.1098/rstl.1857.0011.
- [2] M. V. Kovalenko *et al.*, “Prospects of nanoscience with nanocrystals,” *ACS Nano*, vol. 9, no. 2, pp. 1012–1057, 2015, doi: 10.1021/nn506223h.
- [3] Y. Sun and Y. Xia, “Shape-controlled synthesis of gold and silver nanoparticles,” *Science (80-.)*, vol. 298, no. 5601, pp. 2176–2179, 2002, doi: 10.1126/science.1077229.
- [4] Z. Hens, D. Vanmaekelbergh, E. J. Stoffels, and H. van Kempen, “Effects of crystal shape on the energy levels of zero-dimensional PbS quantum dots,” *Phys. Rev. Lett.*, vol. 88, no. 23, pp. 2368031–2368034, 2002, doi: 10.1103/PhysRevLett.88.236803.
- [5] M. Burian, G. Fritz-Popovski, M. He, M. V. Kovalenko, O. Paris, and R. T. Lechner, “Considerations on the model-free shape retrieval of inorganic nanocrystals from small-angle scattering data,” *J. Appl. Crystallogr.*, vol. 48, pp. 857–868, 2015, doi: 10.1107/S1600576715006846.
- [6] M. Burian and H. Amenitsch, “Dummy-atom modelling of stacked and helical nanostructures from solution scattering data,” *IUCrJ*, vol. 5, pp. 390–401, 2018, doi: 10.1107/S2052252518005493.
- [7] P. Viswanathan, Y. Muralidaran, and G. Ragavan, *Challenges in oral drug delivery: A nano-based strategy to overcome*. Elsevier Inc., 2017.
- [8] A. Feld *et al.*, “Chemistry of Shape-Controlled Iron Oxide Nanocrystal Formation,” *ACS Nano*, vol. 13, no. 1, pp. 152–162, 2019, doi: 10.1021/acsnano.8b05032.
- [9] W. Wu, Z. Wu, T. Yu, C. Jiang, and W. S. Kim, “Recent progress on magnetic iron oxide nanoparticles: Synthesis, surface functional strategies and biomedical applications,” *Sci. Technol. Adv. Mater.*, vol. 16, no. 2, 2015, doi: 10.1088/1468-6996/16/2/023501.
- [10] J. L. Burt, J. L. Elechiguerra, J. Reyes-gasga, J. M. Montejano-carrizales, and M. Joseyacamán, “Beyond Archimedean solids : Star polyhedral gold nanocrystals,” vol. 285, pp. 681–691, 2005, doi: 10.1016/j.jcrysgro.2005.09.060.
- [11] L. Kopanja, S. Kralj, D. Zunic, B. Loncar, and M. Tadic, “Core-shell superparamagnetic iron oxide nanoparticle (SPION) clusters: TEM micrograph analysis, particle design and shape analysis,” *Ceram. Int.*, vol. 42, no. 9, pp. 10976–10984, 2016, doi: 10.1016/j.ceramint.2016.03.235.
- [12] C. E. Blanchet and D. I. Svergun, “Small-Angle X-Ray Scattering on Biological Macromolecules and Nanocomposites in Solution,” *Annu. Rev. Phys. Chem.*, vol. 64, no. 1, pp. 37–54, 2013, doi: 10.1146/annurev-physchem-040412-110132.
- [13] J. D. Watson and F. H. C. Crick, “Molecular Structure of Nucleic Acids: A Structure for Deoxyribose Nucleic Acid,” *Nature*, vol. 171, no. 4356, pp. 737–738, Apr. 1953, doi: 10.1038/171737a0.
- [14] R. P. Rambo and J. A. Tainer, “Super-Resolution in Solution X-Ray Scattering and Its Applications to Structural Systems Biology,” *Annu. Rev. Biophys.*, vol. 42, no. 1, pp. 415–441, 2013, doi: 10.1146/annurev-biophys-083012-130301.
- [15] D. Franke *et al.*, “ATSAS 2.8: A comprehensive data analysis suite for small-angle scattering from macromolecular solutions,” *J. Appl. Crystallogr.*, vol. 50, pp. 1212–1225, 2017, doi: 10.1107/S1600576717007786.
- [16] O. M. Londoño, P. Tancredi, P. Rivas, D. Muraca, L. M. Socolovsky, and M. Knobel, “Small-Angle X-Ray Scattering to Analyze the Morphological Properties of Nanoparticulated Systems,” in *Handbook of Materials Characterization*, Cham: Springer International Publishing, 2018, pp. 37–75.
- [17] O. Glatter and O. Kratky, *SMALL ANGLE X-RAY SCATTERING*. London: Wiley, 1982.

- [18] L. A. Feigin and D. I. Svergun, *Structure Analysis by Small-Angle X-Ray and Neutron Scattering*. New York: Plenum Press, 1987.
- [19] M. Burian, “Shape Retrieval of Inorganic Nanocrystals from SAXS-Data, Master Thesis,” Montanuniversität Leoben, 2014.
- [20] M. Erko, “Water properties in confined geometry, PhD Thesis,” Montanuniversität Leoben, 2012.
- [21] J. Als-Nielsen and M. Des, *Elements of Modern X-Ray Physics*, vol. 252, no. 1. 1951.
- [22] M. Planck, “Ueber das Gesetz der Energieverteilung im Normalspectrum,” *Ann. Phys.*, vol. 4, no. 4, pp. 1–11, 1900, doi: 10.1002/andp.19013090310.
- [23] M. Born, “Quantenmechanik der Stossvorgaenge,” *Zeitschrift fuer Phys.*, vol. 38, no. 11–12, pp. 803–827, Nov. 1926, doi: 10.1007/BF01397184.
- [24] P. Debye, “Zerstreuung von Röntgenstrahlen,” *Ann. Phys.*, vol. 351, no. 6, pp. 809–823, 1915, doi: 10.1002/andp.19153510606.
- [25] P. W. H. Bragg and W. L. Bragg, “The reflection of X-rays by crystals,” *Proc. R. Soc. London. Ser. A, Contain. Pap. a Math. Phys. Character*, vol. 88, no. 605, pp. 428–438, Jul. 1913, doi: 10.1098/rspa.1913.0040.
- [26] H. Schnablegger and Y. Singh, “The SAXS Guide,” *Ant. Paar GmbH*, pp. 1–99, 2013, doi: 10.1006/aphy.1994.1055.
- [27] I. Grillo, “Scattering and Condensed Matter,” *Soft-Matter Charact.*, 2008, doi: 10.1115/ICES2006-1436.
- [28] R. Stepto *et al.*, “Definitions of terms relating to individual macromolecules, macromolecular assemblies, polymer solutions, and amorphous bulk polymers (IUPAC recommendations 2014),” *Pure Appl. Chem.*, vol. 87, no. 1, pp. 71–120, 2015, doi: 10.1515/pac-2013-0201.
- [29] C. D. Putnam, “Guinier peak analysis for visual and automated inspection of small-Angle X-ray scattering data,” *J. Appl. Crystallogr.*, vol. 49, no. 5, pp. 1412–1419, 2016, doi: 10.1107/S1600576716010906.
- [30] O. Glatter, “A new method for the evaluation of small-angle scattering data,” *J. Appl. Crystallogr.*, vol. 10, no. 5, pp. 415–421, 1977, doi: 10.1107/s0021889877013879.
- [31] B. Weyerich, J. Brunner-Popela, and O. Glatter, “Small-angle scattering of interacting particles. II.† Generalized indirect Fourier transformation under consideration of the effective structure factor for polydisperse systems,” *J. Appl. Crystallogr.*, vol. 32, no. 2, pp. 197–209, 1999, doi: 10.1107/S0021889898011790.
- [32] S. Kirkpatrick, C. D. Gelatt, and M. P. Vecchi, “Optimization by Simulated Annealing,” *Science (80-.)*, vol. 220, no. 4598, pp. 671–680, 1983, doi: 10.1126/science.220.4598.671.
- [33] M. Mitchell, “Genetic algorithms: An overview,” *Complexity*, vol. 1, no. 1, pp. 31–39, 1995, doi: 10.1002/cplx.6130010108.
- [34] M. Mitchell, *An Introduction to genetic algorithms*, 5th ed. Cambridge, MA: The MIT Press, 1999.
- [35] N. Metropolis, A. W. Rosenbluth, M. N. Rosenbluth, A. H. Teller, and E. Teller, “Equation of state calculations by fast computing machines,” *J. Chem. Phys.*, vol. 21, no. 6, pp. 1087–1092, 1953, doi: 10.1063/1.1699114.
- [36] H. B. Stuhrmann, “Interpretation of small-angle scattering functions of dilute solutions and gases. A representation of the structures related to a one-particle scattering function,” *Acta Crystallogr. Sect. A*, vol. 26, no. 3, pp. 297–306, 1970, doi: 10.1107/S0567739470000748.
- [37] D. I. Svergun, “Solution scattering from biopolymers: advanced contrast-variation data analysis,” *Acta Crystallogr. Sect. A*, vol. 50, no. 3, pp. 391–402, 1994, doi: 10.1107/S0108767393013492.

- [38] G. Fritz, A. Bergmann, and O. Glatter, "Evaluation of small-angle scattering data of charged particles using the generalized indirect Fourier transformation technique," *J. Chem. Phys.*, vol. 113, no. 21, pp. 9733–9740, 2000, doi: 10.1063/1.1321770.
- [39] T. Raftery and R. Gilles, "JCPDS-International Centre for Diffraction Data Round Robin Study of Silver Behenate. A Possible Low-Angle X-Ray Diffraction Calibration Standard," *Powder Diffr.*, vol. 10, no. 2, pp. 91–95, 1995, doi: 10.1017/S0885715600014421.
- [40] B. Ingham and M. F. Toney, "X-ray diffraction for characterizing metallic films," in *Metallic Films for Electronic, Optical and Magnetic Applications: Structure, Processing and Properties*, 2013, pp. 3–38.
- [41] P. Scherrer, "Bestimmung der Grosse und der inneren Struktur von Kolloidteilchen mittels Röntgenstrahlen," *Nachrichten von der Gesellschaft der Wissenschaften zu Göttingen, Math. Klasse*, no. 26, pp. 98–100, 1918.
- [42] D. Franke, "DAMMIF manual," 2013. [Online]. Available: <https://www.embl-hamburg.de/biosaxs/manuals/dammif.html>. [Accessed: 23-Apr-2020].
- [43] M. B. Kozin and D. I. Svergun, "Automated matching of high- and low-resolution structural models," *J. Appl. Crystallogr.*, vol. 34, no. 1, pp. 33–41, 2001, doi: 10.1107/S0021889800014126.
- [44] M. Burian, G. Fritz-popovski, and M. He, "Considerations on the model free shape retrieval of inorganic nanocrystals from SAXS data," pp. 1–6.
- [45] L. L.-S. H. Jilavenkatesa Ajit, Dapkunas Stanley J., *NIST recommended practice guide : Particle Size Characterization. Special Publication*. 2001.